University of Alberta

Characterizing Charged Muonium in GaAs and Si

by

Bradley Edmund Schultz ©

A thesis submitted to the Faculty of Graduate Studies and Research in partial fulfillment of the requirements for the degree of Master of Science

Department of Physics

Edmonton, Alberta
Fall 2005

Library and
Archives Canada

Published Heritage
Branch

395 Wellington Street
Ottawa ON K1A 0N4
Canada

Bibliothèque et
Archives Canada

Direction du
Patrimoine de l'édition

395, rue Wellington
Ottawa ON K1A 0N4
Canada

Your file Votre référence
ISBN: 0-494-09281-5
Our file Notre référence
ISBN: 0-494-09281-5

NOTICE:
The author has granted a non-exclusive license allowing Library and Archives Canada to reproduce, publish, archive, preserve, conserve, communicate to the public by telecommunication or on the Internet, loan, distribute and sell theses worldwide, for commercial or non-commercial purposes, in microform, paper, electronic and/or any other formats.

The author retains copyright ownership and moral rights in this thesis. Neither the thesis nor substantial extracts from it may be printed or otherwise reproduced without the author's permission.

AVIS:
L'auteur a accordé une licence non exclusive permettant à la Bibliothèque et Archives Canada de reproduire, publier, archiver, sauvegarder, conserver, transmettre au public par télécommunication ou par l'Internet, prêter, distribuer et vendre des thèses partout dans le monde, à des fins commerciales ou autres, sur support microforme, papier, électronique et/ou autres formats.

L'auteur conserve la propriété du droit d'auteur et des droits moraux qui protège cette thèse. Ni la thèse ni des extraits substantiels de celle-ci ne doivent être imprimés ou autrement reproduits sans son autorisation.

In compliance with the Canadian Privacy Act some supporting forms may have been removed from this thesis.

While these forms may be included in the document page count, their removal does not represent any loss of content from the thesis.

Conformément à la loi canadienne sur la protection de la vie privée, quelques formulaires secondaires ont été enlevés de cette thèse.

Bien que ces formulaires aient inclus dans la pagination, il n'y aura aucun contenu manquant.

Canada

Reproduced with permission of the copyright owner. Further reproduction prohibited without permission.

Abstract

This thesis describes μSR measurements aimed at characterizing diamagnetic (i.e. charged) muonium (Mu $= \mu^+e^-$) centers in GaAs and Si. Using muon level crossing resonance (μLCR), the structure of the positively charged center (i.e. Mu$^+$) in p-type GaAs at 50 K is determined. Mu$^+$ is found to sit near the center of a stretched Ga–As bond, with nearest neighbor separations of $r_{Ga} = 1.83 \pm 0.10$ Å and $r_{As} = 1.76 \pm 0.10$ Å. In addition, transverse field (TF) and μLCR measurements are performed in semi-insulating GaAs at 10 K in the presence of an electric field that is used to enhance the diamagnetic signal. The TF relaxation is found to be consistent with that of Mu$^+$ for electric fields between $\approx 1 - 15$ kV/cm. Level crossing data at 20 kV/cm show a resonance signature identical to that of Mu$^+$ in p-type GaAs. As well, a new technique (dubbed ZeroX) is presented to study low-spin semiconductor systems. Measurements in p-type GaAs are conducted as proof-of-principle, and new data from p-type Si are presented.

Acknowledgements

First, I would like to thank my supervisor Kim Chow. His knowledge, enthusiasm, and unrelenting willingness to answer questions was invaluable to my growth as a graduate student. Without his help, much of this thesis would not have been possible.

In addition, I must extend thanks to all of our collaborators, who provided guidance and experimental assistance over the last two years. This includes Rob Kiefl, Bassam Hitti, Roger Lichti, Donald Arseneau, Zahier Salman, Andrew MacFarlane, and Syd Kreitzman. Their assistance made the long experiments at TRIUMF enjoyable, and far less stressful. As well, their experience and patience were essential in guiding me through the (often confusing) world of μSR.

I would also like to thank Don Mullin, Greg Popowich, and Tony Walford for their assistance in the machine shop and in the deposition lab. As well, thanks go out to my examining committee for their careful input and suggestions for my thesis.

Finally, I would like to extend deepest thanks to my family. In particular, my mother Linda's constant support (both emotional and financial) has made the last several years possible.

Table of Contents

List of Tables

List of Figures

Chapter 1

Introduction and Motivation

Semiconductors are an important group of materials which are widely used for both scientific and technological purposes. Ultimately, the usefulness of these materials for any application depends on their electronic and/or optical properties. The atomic impurities inside the semiconductor often play a very important role in determining the properties of the bulk material. One way that impurities can be introduced into the semiconductor is through an intentional process called doping. For example, consider the doping of silicon (Si) (14 electrons) with phosphorous (P) (15 electrons); the additional electron makes P a donor impurity. These extra electrons introduce an energy level into the Si bandgap close to the conduction band edge. As a result, electrons can be easily excited into the conduction band, changing the electronic properties of the material. This sort of change is generally beneficial and is, in fact, the basis of modern electronics. However, there are certain impurities which can enter the material in ways which are difficult to anticipate, such as during the crystal growth process.

One common example of such an impurity is hydrogen (H). Hydrogen is the most abundant element on earth, and easily enters many elemental and compound semiconductors. Inside these materials, H can form three different centers: H^+, H^0, and H^-. Hydrogen is very reactive, and can quickly modify the properties of the host material. It is known to activate neutral impurities, tie up dangling bonds, and form bound states with defects and other impurities (including intentional dopants) inside the lattice. In the process of forming such complexes, the H atom ties up the extra charge carrier associated with the dopant atom. In the above example, the hydrogen would bond to the phosphorous, becoming negatively charged and removing the levels in the bandgap due to the extra electron. The reduction of the electronic activity of a dopant in this fashion is called passivation. In GaAs, many donors (e.g. Si, Ge, Sn, S, Se, and Te), as well

Physical Property	μ^+	p^+
Mass (MeV)	105.66	938.28
Spin	1/2	1/2
Gyromagnetic Ratio $\tilde{\gamma}_\mu$ (μs^{-1}T^{-1})	135.54	42.58
Lifetime (μs)	2.197	stable
	Mu^0	H^0
Reduced mass (m_H)	0.9956	1
Ground state radius (a_0)	1.0044	1
Ground state energy (E_H)	0.9956	1

Table 1.1: Selected physical properties of the muon, proton, Mu, and H.

as acceptors (e.g. Be, Mg, Cd, Zn, and C) are all passivated by hydrogen. In addition, hydrogen itself can act as a donor or acceptor (for more information on hydrogen in semiconductors, see [1, 2, 3, 4]). The passivation of both types of impurities is possible because H is an amphoteric impurity; that is, it changes its charge state to act as a compensating defect in heavily-doped materials. The ionized dopants and H will be of opposite charge, resulting in a strong Coulomb attraction and the resultant passivation of the dopant atom. In principle, the behavior of hydrogen as an impurity in semiconductors can be either beneficial or unfavorable. Certain applications involve the use of hydrogen to improve material properties, such as the passivation of dislocations and other defects in silicon solar cells [5, 6]; the hydrogen ties up any free bonds, eliminating them as electron-hole recombination centers. However, the *unintentional* introduction of hydrogen into materials is almost always detrimental for the reasons mentioned above.

Modification of the host properties in this way has implications for technological applications, making the study of hydrogen in semiconductors very important. Although a great deal is known about the passivation complexes of hydrogen, its high mobility and reactivity present problems when trying to study *isolated* hydrogen centers (i.e. H that has not yet reacted with any lattice defects), as well as the formation and dissociation of hydrogen complexes as they happen.

Although it is difficult to gather *direct* information on isolated hydrogen in semiconductors, it is widely recognized that the *indirect* study of hydrogen can be done using muonium (Mu). The neutral muonium "atom" is an electron bonded to a positive muon (μ^+). Similar to hydrogen, muonium can form neutral (Mu^0) and charged (Mu$^+$, Mu$^-$) centers upon entering the host. Muonium can be treated as a light pseudoisotope of H, with a mass of approximately 1/9th that of atomic hydrogen (p^+e^-). Mu and H have almost identical electronic structures in vacuum, due not only to the identical spin and charge of the muon and proton, but also to the almost identical reduced masses of both atoms ($m_p > m_\mu >> m_e$). A comparison of muon, proton, Mu, and H properties are shown in Table 1.1.

Muonium in semiconductors is studied using a set of techniques known as muon spin rotation/resonance/relaxation (μSR), an overview of which can be found in [7, 8, 9]. μSR involves the implantation of spin-polarized muons into a sample. The muon acts as a sensitive magnetic probe; measurement of the time-evolution of the muon spin gives detailed information on interactions with the nuclei inside the material. In μSR, only a few muons (or sometimes only one) are implanted into the sample at any given time. As a result, muon-muon interactions inside the host will be negligible. Combined with the short lifetime of the muon ($\tau_\mu = 2.2\ \mu$s), this makes isolated muonium relatively straightforward to study. However, although muonium can be used as a hydrogen analogue, there are key differences which must be understood before making a direct comparison. First, the two impurities are introduced under very different circumstances. Hydrogen typically enters semiconductors during the growth of the crystal, and as a result is likely at equilibrium by the time the sample is studied. On the other hand, muons are implanted directly into the sample, and quite possibly do not reach equilibrium before they decay. The muon lifetime restricts the muonium centers that can be studied; only those that are formed within a few muon lifetimes ($\approx 10\ \mu$s) can be detected. Furthermore, these centers may not have time to reach thermal equilibrium, particularly at low temperatures. One consequence of this is the fact that multiple muonium states (for example Mu^0 and $\mathrm{Mu}^\pm$) can co-exist inside the host at the same time.

Second, the differing masses of the muon and proton can lead to different kinetic behavior. Ignoring zero point motion effects due to the lighter mass of the muonium compared to hydrogen, one expects the energy level positions of each to be almost identical within the band gap. However, the difference in zero point energies tends to place the energy level of muonium in a given potential well higher than that of hydrogen. This can result in a modification of the ionization energies. Furthermore, due to muonium's lighter mass, one would also expect a difference in diffusion related processes.

To date, there have been extensive studies of muonium centers (Mu^+, Mu^0, and Mu^-) in many semiconductors. Arguably, one of the best studied semiconductors is GaAs. This is due largely to the fact that all nuclei are spin 3/2 (^{71}Ga, 39.8% abundant; ^{69}Ga, 60.2% abundant; ^{75}As, 100% abundant), resulting in a variety of muon-nuclear interactions. In high-resistivity, semi-insulating (SI) GaAs at low temperature, two distinct neutral (i.e. paramagnetic) centers are formed: Mu^0_{BC} (historically known as Mu*, or anomalous muonium) and Mu^0_T (historically known as normal muonium). The subscript notation now widely used reflects the position of each of these centers within the lattice (see Figure 1.1). The Mu^0_{BC} center is immobile on the timescale of the muon lifetime, and is located in a (stretched) Ga–As bond; i.e. at the bond center (BC) site. This center is characterized by a small anisotropic hyperfine interaction which is axially symmetric about a $\langle 111 \rangle$ crystalline axis, with most of the electron spin density residing on the nearest neighbor nuclei [10]. On the other hand, Mu^0_T appears to be rapidly diffusing between interstitial tetrahedral (T) sites, and is characterized by a large isotropic hyperfine parameter [7, 11]. The ionization temperatures for Mu^0_{BC} and Mu^0_T are approximately 150 K and 450 K respectively [7]. This, in addition to the localized spin density of the electron, indicates that the energy levels for both centers lies deep within the gap, at least a few hundred meV below the conduction band.

Although the paramagnetic centers have been well characterized in GaAs, until recently considerably less information existed for the charged (i.e. diamagnetic) centers. The experimental existence of these states is clear (for example, by looking at the muon precession frequencies in a transverse magnetic field). However, there is much that is not known about the structure, and even the charge (i.e. positive or negative) of the center cannot be determined directly [12]. The primary difficulty is the lack of an unpaired electron spin, and the resulting lack of hyperfine and nuclear hyperfine interactions. Characterization of the diamagnetic centers (Mu^+ and Mu^-) must therefore be done by studying the muon-nuclear dipole interaction with neighboring nuclei, as well as the muon induced nuclear electric quadrupole (neq) interaction. Although these are weak compared to the hyperfine interactions, it is still possible to gather considerable information.

In SI-GaAs, only a very small diamagnetic signal is present at low temperature. In heavily-doped (either p- or n-type) GaAs, one would expect the situation to change due to the large number of excess holes or electrons in the sample. Theoretically, the most stable equilibrium charge state of isolated H or Mu should depend on the location of the Fermi level with respect to the muonium level [13]. For example, in heavily-doped n-type semiconductors where the Fermi level is close to the conduction band edge, the negative charge state (i.e. H^- or Mu^-) is favored, while the positive state (H^+ or Mu^+) is more stable in heavily doped p-type semiconductors where the Fermi level is close to the edge of the valence band. As a result, isolated H in GaAs is a so-called "negative-U" impurity; that is, H^+ or H^- are the energetically favorable states (depending on the Fermi level), but never H^0.

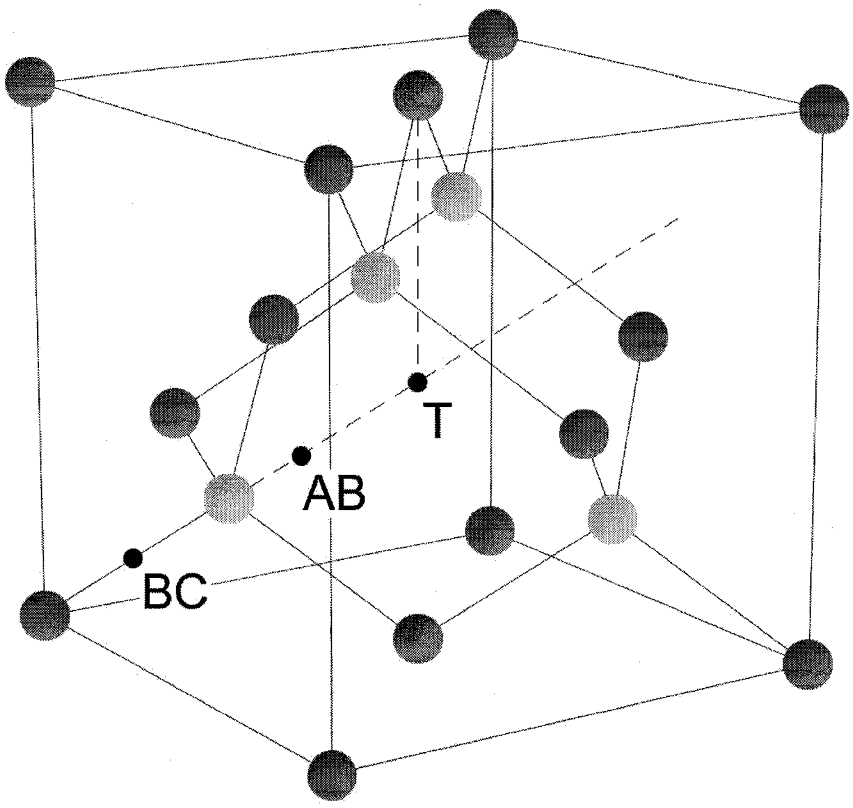

Figure 1.1: Zincblende structure of a Group III-V semiconductor such as GaAs. Black dots represent interstitial sites mentioned in the text: bond center (BC), tetrahedral (T), and anti bonding (AB). The darkly shaded circles represent one type of nuclei, while the lightly shaded circles represent the other. This structure is also valid for a Group IV semiconductor such as Si, except all atoms would be of the same type.

Experimentally, there has been considerable work done on understanding both diamagnetic centers. Although the charge of these states has yet to be directly measured, the dramatically different kinetics and stability of these centers in differently doped samples of GaAs confirms that Mu^+ and Mu^- are in fact distinct centers. In n-type GaAs, the diamagnetic center is static until approximately 500 K, where it begins to diffuse with an activation energy $E_a^- = 0.73 \pm 0.01$ eV [14]. In p-type GaAs, the situation is very different. The muon is found to be static until ≈ 180 K, where it begins to diffuse with $E_a^+ = 0.15 \pm 0.04$ eV [15]. At temperatures above 400 K, the muon appears to be undergoing trapping/detrapping with a Zn impurity. (To date, this is the only *direct* observation of the reaction between an isolated muonium (or hydrogen) center with an intentional impurity in a semiconductor). The differing behavior of the charged centers, combined with theoretical considerations, has led to the assignment of Mu^+ and Mu^- as the diamagnetic centers in p- and n-type GaAs respectively.

Prior to the work in this thesis, only Mu^- had been structurally characterized [16]. Theoretical calculations show that in n-type GaAs, Mu^- should be stable at the interstitial T site, surrounded by Ga nearest neighbors [1, 13, 17]. Using muon level crossing resonance (μLCR), a sensitive technique used to probe muon-nuclear dipole and quadrupole interactions, a distinct set of magnetic resonances are observed at magnetic fields less than ≈ 50 mT. A detailed analysis of these resonances (which appear due to resonant transfer of the muon's spin to the neighboring nuclei) indicates that Mu^- is located at or near the interstitial T_{Ga} site, as theory predicts. Theoretical studies conducted on p-type GaAs indicate that Mu^+ should be located at the BC site, between nearest neighbor Ga and As atoms. In this thesis, we perform experiments on p-type GaAs:Zn in an effort to ascertain the structure of Mu^+. Detailed numerical analysis of the corresponding μLCR spectra is used to determine the site and symmetry of the muon with respect to its nearest neighbors, and to estimate the muon-nuclear separation. This information should allow Mu^+ to be assigned definitively to a site in the GaAs lattice.

Although a great deal is known about the structure and kinetics of isolated muonium, little is known about the underlying formation of these states immediately after implantation of the energetic muon. This is primarily due to the short time scales over which the formation processes occur. In order to observe a coherent precession, Mu must be formed in a time period much less than the hyperfine period (several nanoseconds for Mu^0_{BC} and 0.5 ns for Mu^0_T), or significant dephasing of the signal would occur. In GaAs, it has been shown that the application of an electric field (EF) in the range 5–20 kV/cm can dramatically enhance the diamagnetic signal at the expense of Mu^0_{BC} [18, 19]. It is likely that epithermal (i.e. prompt) processes would be unaffected by such small electric fields; this is evidence that Mu^0_{BC} is formed after thermalization via capture of an electron from the radiation track left behind by the incoming muon. The strength of the field is insufficient to directly field ionize the ground state of Mu^0_{BC}. Instead, the magnitude is consistent with that required to field ionize a shallow center or an exciton. One possibility is that the formation of Mu^0_{BC} occurs through an intermediate excited shallow muonium center. If the electric field is sufficient to field ionize this center, then capture of an electron by the muon would be inhibited, leading to an enhanced signal corresponding to Mu^+. On such a short time scale, a third body would be required to carry away excess energy and momentum, such as a second electron or hole from the radiation track. It is also possible that the formation occurs via direct capture of an electron from an exciton, with the hole carrying away the excess energy and momentum. In this case, the role of the electric field would be to ionize the exciton, inhibiting electron capture by the muon since there is no third body to carry away energy and momentum. In either case, we see that the electric field acts to inhibit formation of the neutral center. On the other hand, if formation were occurring epithermally, it could be subsequently converted to Mu^+ or Mu^- via capture of a thermalized hole or second electron respectively. The electric field would thus act to ionize an exciton, providing the extra holes and electrons necessary for this to happen. In this thesis, we utilize an electric field to enhance the diamagnetic signal in SI-GaAs. Comparison of the data to existing signatures for Mu^+ and Mu^- will determine which charge state is forming as a function of electric field. In principle, this could lead to a better understanding of muonium formation between muon implantation and decay, and possibly a method to control the formation of the diamagnetic centers using an electric field.

In the context of μSR, GaAs is an excellent semiconductor to study using muons, since all nuclei have non-zero spin. However, many semiconductors possess a very low abundance of nuclear spins which are non-zero. A good example of this is Si. Si is composed of three isotopes: ^{28}Si, 92.23% abundant, spin 0; ^{29}Si, 4.68% abundant, spin 1/2; and ^{30}Si, 3.09% abundant, spin 0. Since the muon is a magnetic probe, it will only interact with nuclei which possess non-zero spin; i.e. ^{29}Si. The low abundance of this isotope, combined with the weak strength of the dipole interaction (the spin 1/2 Si nuclei do not possess a neq moment, so the quadrupole interaction is nonexistent) makes it difficult to extract a useful signal using current μSR techniques. A technique used to greatly enhance the sensitivity in low-spin materials ("ZeroX") is presented in this thesis, and preliminary results discussed.

The structure of this thesis is as follows. Chapter 2 describes the fundamentals of the μSR techniques. Chapter 3 will cover the theoretical background necessary to analyse and interpret the experimental data presented later. Details of the μLCR experiments in p-type GaAs and electric field experiments in SI-GaAs will be discussed in Chapters 4 and 5 respectively. Chapter 6 will give an introduction to the ZeroX technique, with a brief discussion of preliminary data taken in both GaAs and Si. Concluding remarks will be given in Chapter 7. Appendix A discusses the rotating reference frame transformation of transverse field μSR data, and Appendix B lists the Mathematica code used to simulate level crossing resonances.

Chapter 2

μSR Fundamentals

In this chapter, a general introduction to the fundamentals of the μSR techniques are given. Specific details of the so-called μLCR and EF-μSR methods actually used to gather the experimental data will be discussed in more detail in Chapters 4 and 5. μSR (which stands for muon spin rotation/resonance/relaxation) is the mnemonic for a set of complementary experimental techniques which use muons as a sensitive magnetic probe of matter. As we will see, the success of μSR depends on our ability to:

- Generate muons which are highly spin polarized (i.e. the muon spins all point in the same direction).
- Detect where this spin is pointing sometime after the muon has been implanted into the sample.

The purpose of this chapter is to discuss these points in more detail.

Section 2.1 gives an overview of muon production and decay. In Section 2.2, we discuss the classification of the different μSR techniques, according to the manner in which the experiment is set up and data recorded. This is followed in Section 2.3 by a discussion of the form and analysis of basic μSR data, including extraction of the all-important muon polarization. (More details on μSR can be found in [7, 8, 9]).

2.1 Muon Production and Decay

The creation of spin-polarized muons is a multi-step process, that varies from one facility to another. All experimental data collected in this thesis were gathered at the Tri-University Meson Facility (TRIUMF), in Vancouver, Canada. Hence, all details discussed below will therefore be limited to what is done at TRIUMF.

The process begins with the introduction of negatively charged hydrogen ions (H^-) into a large cyclotron. Powerful magnetic fields (≈ 0.6 T) are used to guide the ions in a widening spiral path, while electric fields "kick" the ions every half turn to accelerate them. The resulting beam has an energy of approximately 500 MeV. At some point, the ions are intercepted by a carbon foil which strips off the electrons, leaving behind a positively charged proton (p^+). Being of opposite charge to H^-, the protons are bent in the opposite direction in the magnetic field, leaving the cyclotron.

After exiting the cyclotron, the protons are guided down a beamline using dipole and quadrupole magnets to focus and steer the particles. The protons eventually collide with a production target made up of some light nuclear element, such as carbon (graphite) or beryllium. These high energy (≈ 500 MeV) protons strike neutrons and other protons inside the nuclei and generate a number of reactions, including:

$$\begin{aligned} p^+ + p^+ &\rightarrow \pi^+ + p^+ + n \\ p^+ + n &\rightarrow \pi^+ + n + n \end{aligned} \tag{2.1}$$

As (2.1) shows, one of the products of these reactions is the positively charged pion (π^+), an unstable spin zero particle with a lifetime of $\tau_\pi = 26$ ns. Pion decay leads to the production of a positively charged muon (μ^+) and muon neutrino:

$$\pi^+ \rightarrow \mu^+ + \nu_\mu \tag{2.2}$$

Some of the pions stop near the surface of the production target before decaying; muons generated in this fashion are called surface muons. The parity violating weak decay of the pion requires that both the muon and neutrino spins are polarized antiparallel to their momentum. In this way, a nearly 100% polarized beam of muons can be generated. This is the first essential requirement of μSR. At TRIUMF, surface muons created in this fashion have a kinetic energy of about 4 MeV and a nominal momentum of 30 MeV/c. In GaAs with a thickness of ≈ 0.35 cm (typical of our samples), this corresponds to a range of ≈ 100 mg/cm^2 and a muon stopping distance of a few hundred microns.

The polarized muons are guided further down the beamline, eventually entering the sample. Prior to this, they are passed through a set of crossed electric (E) and magnetic (B) fields (called a Wien filter), which serves two functions. First, the fields act as a velocity separator to eliminate unwanted particles (with the same momentum but different mass than the muons) which may contaminate the beam. Only particles with velocity v such that

$$v = \frac{E}{B} \tag{2.3}$$

will pass straight through the region containing the fields. Second, the Wien filter allows the muons to be spin rotated with respect to the applied magnetic field through the sample. For example, this is necessary for most transverse field experiments, where the spin is rotated by 90° with respect to the applied magnetic field.

Once inside the sample, the muon will decay ($\tau_\mu = 2.2\ \mu$s) into a positron, an electron neutrino, and a muon antineutrino:

$$\mu^+ \rightarrow e^+ + \nu_e + \bar{\nu}_\mu \tag{2.4}$$

The emitted positron energy varies continuously from zero (if both neutrinos are emitted in opposite directions, carrying away all the kinetic energy) to $E_{\text{max}} = 52.3$ MeV (if both neutrinos travel together, in opposite directions to the positron). The decay probability of the muon, i.e. the probability that a positron is emitted in a particular direction with respect to the muon spin, can be calculated from electroweak theory (see [8] and references therein). After integrating over the neutrino momenta, the probability per unit time for positron emission at an angle θ with respect to the muon spin is

$$dW(\epsilon, \theta) = \frac{1}{\tau_\mu}\left[1 + a(\epsilon)\cos\theta\right] n(\epsilon)\, d\epsilon\, d\cos\theta \tag{2.5}$$

where $\epsilon = E/E_{\text{max}}$ is the reduced positron energy, and

$$\begin{aligned} a(\epsilon) &= \frac{2\epsilon - 1}{3 - 2\epsilon} \\ n(\epsilon) &= \epsilon^2(3 - 2\epsilon) \end{aligned} \tag{2.6}$$

For large values of ϵ, the term '$1+a(\epsilon)\cos\theta$' in (2.5) leads to a large spatial asymmetry in the decay. Figure 2.1(a) shows a graph of this term for a variety of ϵ values. Integrating $dW(\epsilon, \theta)$ over the entire range of reduced positron energies ($\epsilon = 0$ to $\epsilon = 1$) yields

$$dW(\theta) = W(\theta)\, d\cos\theta \tag{2.7}$$

where

$$W(\theta) = \frac{1}{2\tau_\mu}\left(1 + \frac{\cos\theta}{3}\right) \tag{2.8}$$

This energy-averaged positron distribution is shown in Figure 2.1(b). This closely represents the distribution seen in an actual experiment, since positrons of many different

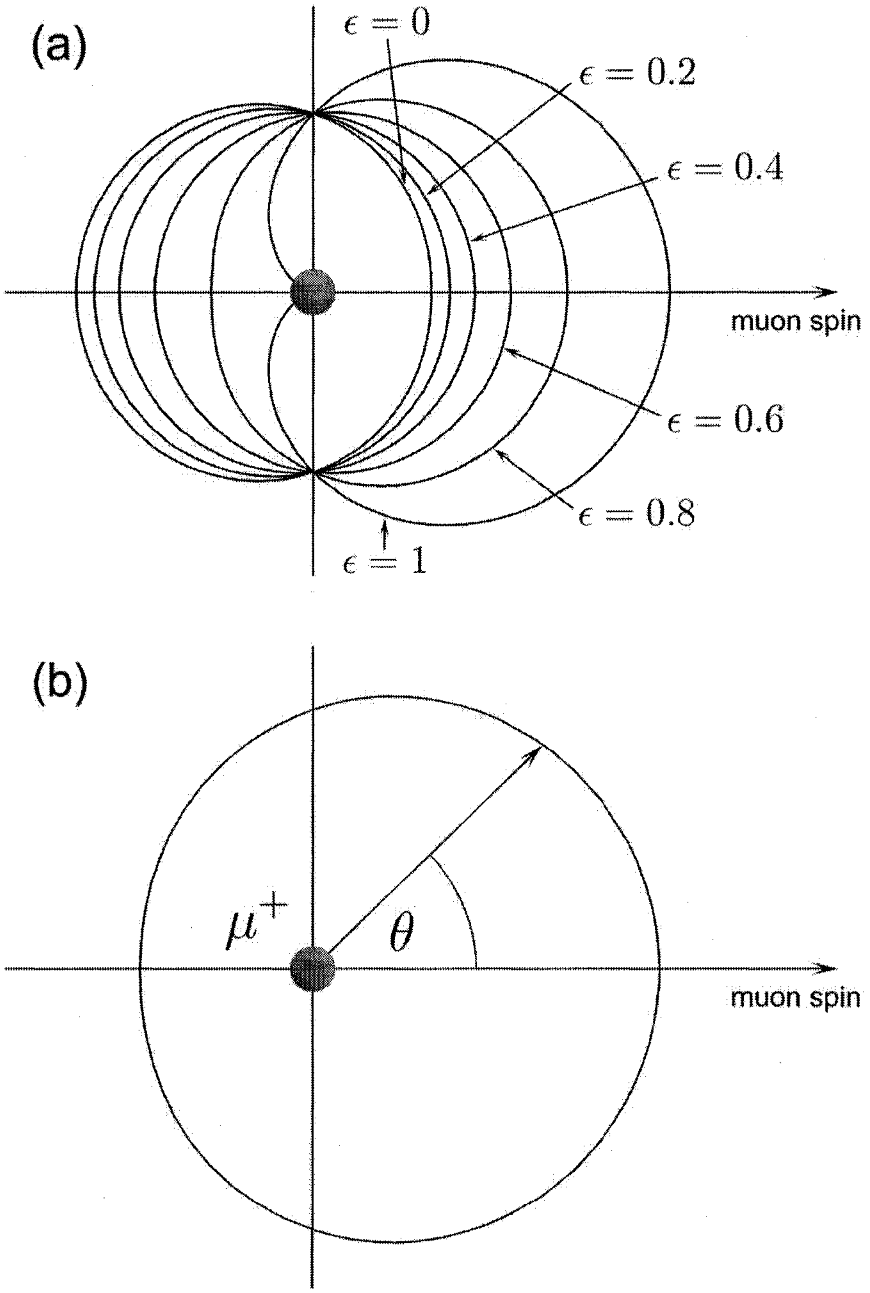

Figure 2.1: (a) Polar graph of the term $1 + a(\epsilon)\cos\theta$, for various reduced positron energies ϵ. (b) Energy averaged distribution $W(\theta)$. The shaded circle represents the muon.

energies are produced. Note that the decay is not spatially isotropic; rather, the positron is emitted preferentially along the direction of the muon spin. Therefore, by detecting the direction from which the decay positron came, we can determine the direction of the muon spin at the time of decay. (Of course, muon decay is a stochastic process, and as such a large number of decays must be observed to generate a reliable picture of the muon spin). The large spatial asymmetry of the positron emission is the second key feature of μSR; when combined with the high polarization of the incoming muon beam, it allows the time evolution of the muon spin in the sample to be experimentally measured. The muon polarization function, which is the expectation value of the muon spin (i.e. the direction the spin is pointing at any given time), is determined by the interactions between the muon and its local environment, and is the quantity of interest in any μSR experiment.

2.2 μSR Techniques

The μSR techniques are generally classified according to two criteria: (1) whether the data are time dependent or not, and (2) how the applied magnetic field is oriented with respect to the initial muon spin in the sample.

Experiments where the explicit time dependence of the polarization is recorded are known as time differential (TD). Figure 2.2 shows a schematic of a typical μSR setup. The incoming muon is detected using a muon counter (TM) which starts a clock. The time and direction of the decay positron is subsequently measured, stopping the clock and incrementing the appropriate time histogram. The positron is detected using a set of positron counters [labeled forward (F), backward (B), left (L), and right (R)] arranged around the sample. (The counter labels are defined with respect to the direction the muon is "looking" when it enters the sample). Recording the time dependence of the muon decay requires that each positron be unambiguously correlated to its parent muon; in other words, there must only be one muon in the sample at a time. Experimentally, this places a strict limit on the rate at which muons can be implanted into the sample. The time window in which decay positrons can be reliably measured is several muon lifetimes (≈ 10 μs), leading to a maximum theoretical rate on the order of 10^5 muons per second. (Practically, the muon rate for TD experiments must be lowered even further to become manageable). A system of electronics is then required to reject events involving multiple muons and/or multiple positrons (as well as record timing information); discarding these events further lowers the "good" muon rate. In certain experiments, the time dependence of the polarization is not required and can be discarded. Such experiments are classified

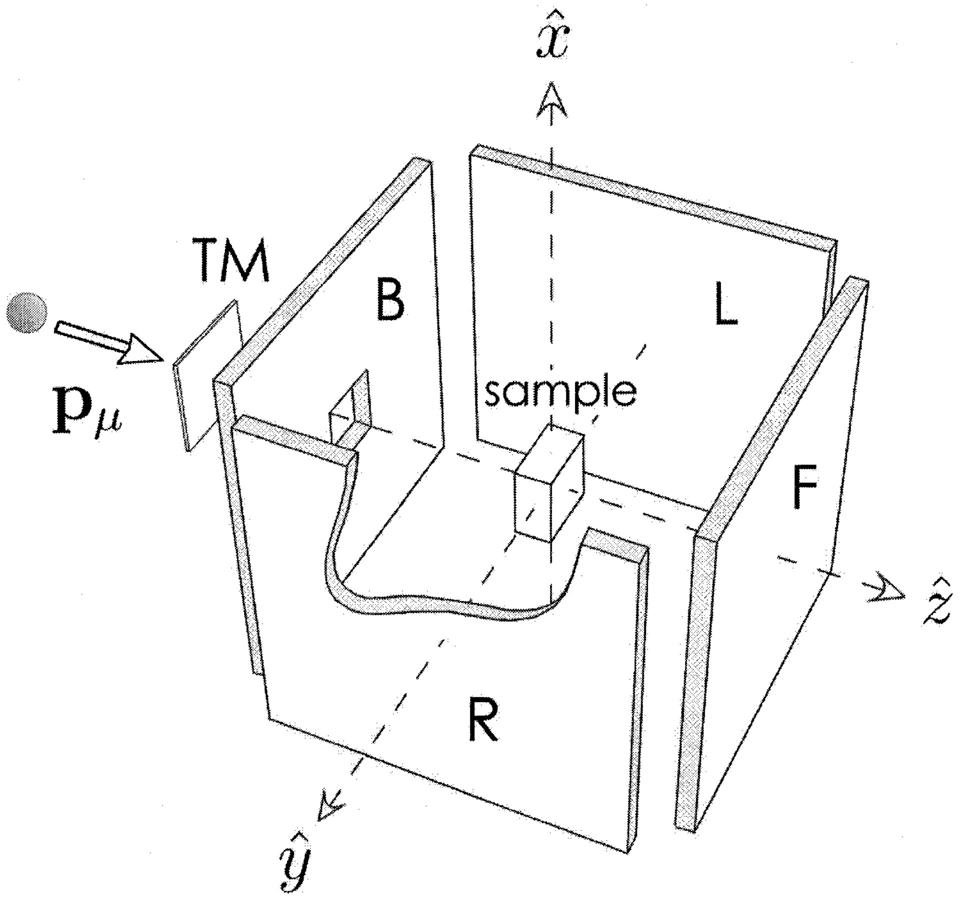

Figure 2.2: Schematic of typical counter arrangement for a μSR experiment. A muon with momentum $\mathbf{p}_\mu$ along $\hat{z}$ enters from the left. The muon counter is labeled by TM. F, B, L, and R label the forward, backward, left, and right counters respectively. Figure modified from one originally in [20].

as time-integral (TI). In this case, only the total number of counts is required, and is obtained by integrating the count rate over some time interval much larger than the muon lifetime. Doing this lifts the limit on the muon rate, allowing as many muons in the sample as can be delivered by the beam and processed by the electronics.

Further classification of μSR experiments depends on the magnetic field orientation. In transverse field (TF) experiments, the muon spin is initially perpendicular to the applied field $\mathbf{B}$ (this usually means the field is along $\hat{z}$ in Figure 2.2 and the muon spin will be rotated perpendicular to this axis). If the initial spin and field are parallel, the experiment is known as longitudinal field (LF). In a zero field (ZF) experiment, there is no applied magnetic field.

There are a number of μSR spectrometers available at TRIUMF, which can contain a variety of magnets and particle counters. Typically, the primary magnet is oriented such that the applied field is parallel (or antiparallel) to the momentum of the incoming muons (usually taken as the $\hat{z}$ direction). Often, there are additional auxiliary coils arranged around the primary magnet which can be used to zero the net field, or to apply a weak transverse field (wTF) through the sample. Equivalently, the muon can be spin rotated perpendicular to $\hat{z}$ before entering the sample. The three main spectrometers used to collect the data in this thesis are listed below:

1. HELIOS: HELIOS is a large superconducting solenoid with a bore diameter of 15.24 cm and a bore length of 60.96 cm. This magnet is capable of generating fields up to 7 Tesla along $\hat{z}$.

2. LAMPF: LAMPF provides a maximum field of ≈ 0.3 Tesla using a large set of Helmholtz coils. In addition, there are two smaller sets of coils arranged perpendicular to the primary set, capable of generating fields of up to 10 mT along the $\hat{x}$ and $\hat{y}$ directions.

3. SFUMU: The SFUMU spectrometer contains a set of Helmholtz coils capable of generating 0.45 T along either $\hat{y}$ or $\hat{z}$.

The particle counters arranged around the sample used to detect muons and positrons are plastic scintillators, which give off a flash of light when an energetic ionizing particle passes through them (the muon counter is thin enough that is does not adversely affect the energy of the muon). The photons are collected in a photomultiplier tube, and the amplified signal is then transmitted outside the experimental area to a monitoring room using coaxial cable. The signal is then processed using relevant electronics which assures that only good decay events are recorded.

2.3 μSR Data

Consider a histogram of the number of decay events $N_i(t)$ recorded by a particular positron counter i. It has the following form:

$$N_i(t) = N_i(0)e^{-t/\tau_\mu}\left[1 + A_i P_i(t)\right] + b_i \tag{2.9}$$

where A_i is a constant that depends on experimental factors such as the solid angle of the counter and the probability distribution of the emitted positron (A_i is typically on the order of ≈ 0.2), $P_i(t)$ is the projection of the muon polarization $\mathbf{P}(t)$ on the symmetry axis of the ith counter, and b_i is a random background which is generally assumed to be time-independent.

Figure 2.3(a) shows an example of $N_i(t)$ under transverse field conditions. (The sample is p-type GaAs:Zn at $T = 50$ K with $B_{TF} \approx 10$ mT). The oscillating component is due to precession of the muon spin in the magnetic field (i.e. Larmor precession). This is superimposed over the exponential decay of the muon. Typically, μSR data are displayed as a combination of histograms, rather than a single one. The primary reason for this is to isolate the signal of interest (i.e. the muon polarization). For example, in the data shown in Figure 2.3(a), this corresponds to the oscillating component. This is done by defining a quantity known as the asymmetry. For an opposing pair of counters labeled $+i$ and $-i$ [which are 180° out of phase, such that $P_{-i}(t) = -P_i(t)$], the asymmetry is

$$A(t) = \frac{[N_{+i}(t) - b_{+i}] - [N_{-i}(t) - b_{-i}]}{[N_{+i}(t) - b_{+i}] + [N_{-i}(t) - b_{-i}]} \tag{2.10}$$

This combination will eliminate the exponential factor, as well the background terms. By defining

$$\alpha = \frac{N_{-i}(0)}{N_i(0)}; \quad \beta = \frac{A_{-i}}{A_i} \approx 1 \tag{2.11}$$

we obtain

$$A(t) = \frac{(1-\alpha) + A_i P_i(t)(1+\alpha)}{(1+\alpha) + A_i P_i(t)(1-\alpha)} \tag{2.12}$$

which is known as the "raw asymmetry". Typically, α is fit from the raw data, and the "corrected asymmetry", $A_i P_i(t)$, is extracted. The corrected asymmetry is the most common form for displaying and analysing μSR data. An example of the corrected asymmetry for a TF field experiment is shown in Figure 2.3(b). The solid line is a best fit to the data, assuming a Gaussian damping of the oscillations. The large statistical error at longer times correspond to a decrease in counts at these times.

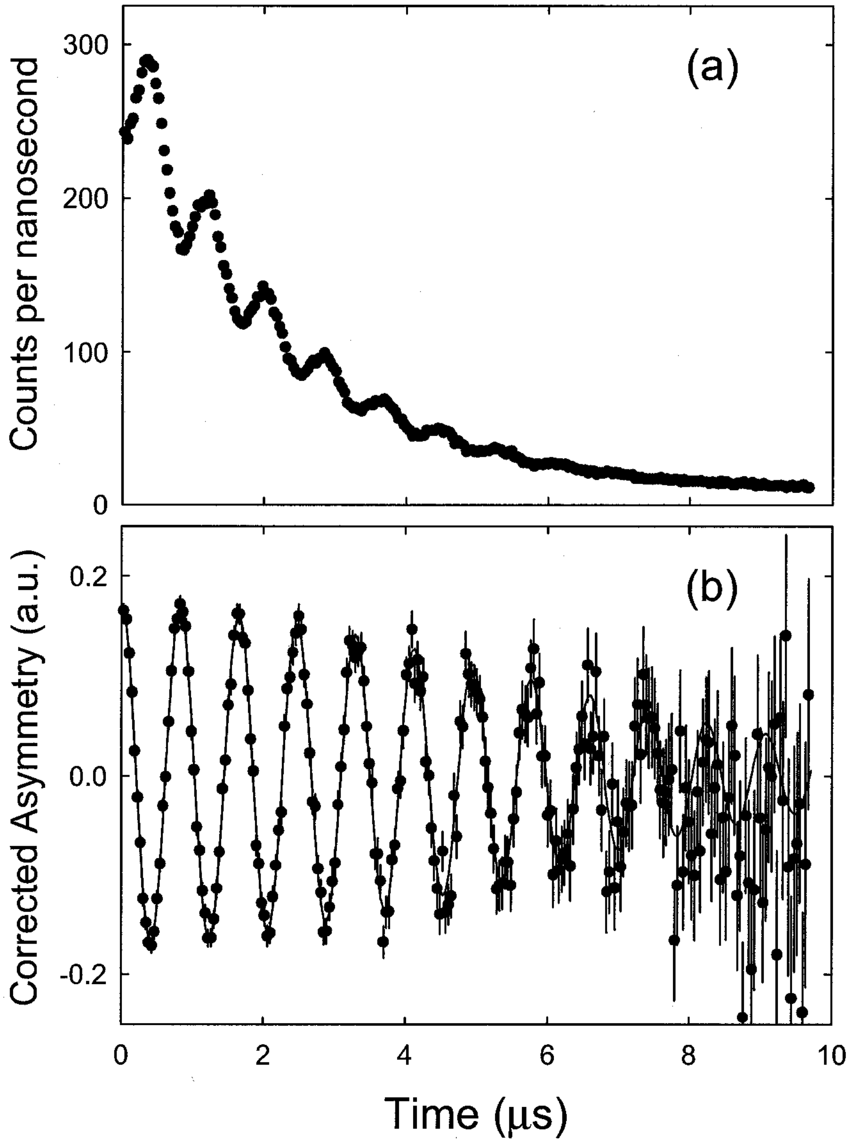

Figure 2.3: Time-dependant data for p-type GaAs:Zn at $T = 50$ K with $B_{TF} \approx 100$ G. (a) Raw data for a single histogram. (b) Corrected asymmetry for two histograms. Solid line is a best fit to the data assuming a Gaussian relaxation.

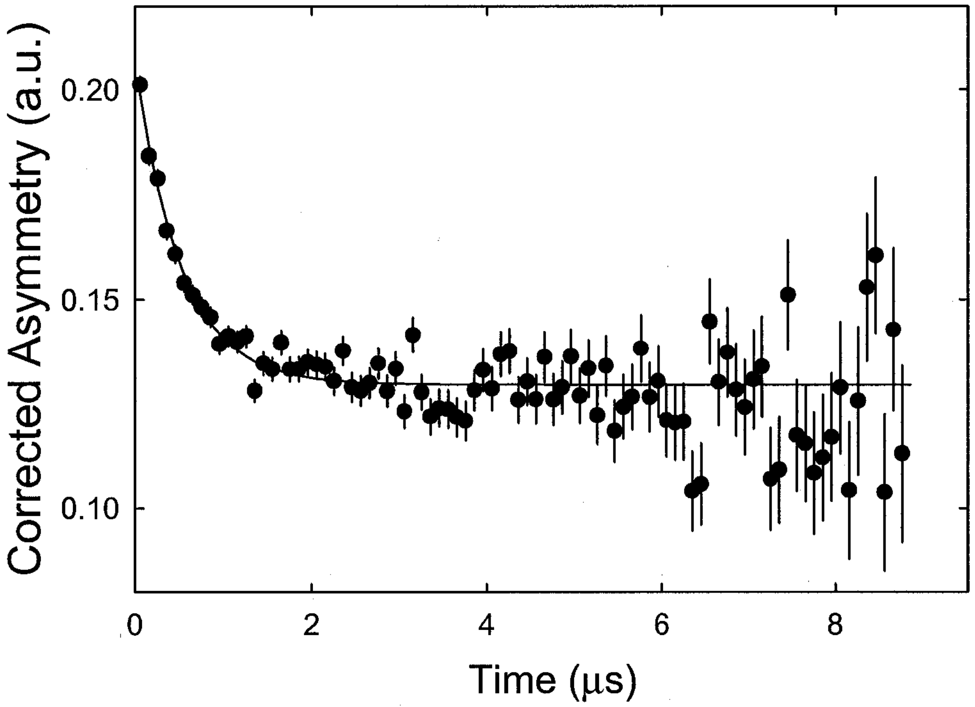

Figure 2.4: Time-dependant corrected asymmetry for a sample of GaN with $T = 2$ K and $B_{LF} \approx 15$ G. Solid line is a best fit to the data assuming an exponential relaxation.

Although there are no TD-LF experiments discussed in this thesis, an example of such a spectrum is shown in Figure 2.4 for completeness. (The sample is GaN at $T = 2$ K with $B_{LF} \approx 15$ G). The solid line is a best fit to the data assuming an exponential relaxation.

In TI experiments where the explicit time-dependence is not needed, we record the time-integrated counts for a histogram i, given by

$$\eta_i = \int_0^\infty \frac{1}{\tau_\mu} N_i(t) dt \tag{2.13}$$

and the normalized time-integrated polarization, given by

$$\bar{P}_i = \frac{\displaystyle\int_0^\infty e^{-t/\tau_\mu} P_i(t) dt}{\displaystyle\int_0^\infty e^{-t/\tau_\mu} dt} \tag{2.14}$$

Chapter 3

Theoretical and Numerical Considerations

This chapter discusses some of the theoretical and numerical aspects of the thesis. We begin by looking at the spin Hamiltonians used in the analysis, including an overview of the relevant muon-nuclear interactions, in Section 3.1. In Section 3.2, a quantum mechanical derivation of the time-dependant polarization is presented using density matrix theory. A discussion of the muon level crossing phenomenon is discussed in Section 3.3. Details of the numerical simulation of μLCR spectra are discussed in Section 3.4. Finally, Section 3.5 discusses the depolarization of the muon precession signal in a transverse magnetic field.

3.1 Hamiltonians

One of the main goals of this thesis is to study the interaction of muon spins with those of the surrounding nuclei. As a result, we are interested in the spin Hamiltonian describing these interactions, since this will allow us to calculate the evolution of the muon spin polarization. In this section, we will discuss the general form of this Hamiltonian, and look at specific examples that will become useful in future analysis.

Before going into detail on the Hamiltonians used to describe our muon-nuclear system, it is worthwhile to first discuss some of the important interactions. Typically, we will be considering a system consisting of a muon and some number of nuclei (with spins greater than 1/2) in an external magnetic field. In these cases, there are three interactions which will be of interest:

1. **Zeeman interaction**: The interaction between a magnetic dipole $\vec{\mu}$ and a mag-

netic field **B** is known as the Zeeman interaction. The coupling is described by the Hamiltonian

$$\mathcal{H} = -\vec{\mu} \cdot \mathbf{B} = -\tilde{\gamma}\hbar \mathbf{I} \cdot \mathbf{B} \tag{3.1}$$

where **I** is the spin of the particle, $\hbar$ is Planck's constant, and $\tilde{\gamma}$ is the gyromagnetic ratio of the particle. Consider the simple example of an isolated muon ($I = 1/2$) in a magnetic field, which we will assume is parallel to the z-axis. The Zeeman interaction will split the energy levels of the muon, and the corresponding eigenvalues will be $-\tilde{\gamma}_\mu \hbar B/2$ (corresponding to "spin up") and $\tilde{\gamma}_\mu \hbar B/2$ (corresponding to "spin down").

2. **Muon-nuclear dipole interaction**: The dipole interaction is a result of the magnetic coupling between two magnetic dipoles $\vec{\mu}_1$ and $\vec{\mu}_2$. Quantum mechanically, the Hamiltonian for this is given by

$$\mathcal{H} = \frac{\vec{\mu}_1 \cdot \vec{\mu}_2}{r^3} - 3\frac{(\vec{\mu}_1 \cdot \mathbf{r})(\vec{\mu}_2 \cdot \mathbf{r})}{r^5} \tag{3.2}$$

where $\mathbf{r}$ is the vector connecting the dipoles, and r is their separation. Since $\vec{\mu}_i = \tilde{\gamma}_i \hbar \mathbf{I}_i$, the Hamiltonian becomes

$$\mathcal{H} = \frac{\tilde{\gamma}_1 \tilde{\gamma}_2 \hbar^2}{r^3} \left[\mathbf{I}_1 \cdot \mathbf{I}_2 - 3(\mathbf{I}_1 \cdot \hat{r})(\mathbf{I}_2 \cdot \hat{r})\right] \tag{3.3}$$

where $\hat{r} = \frac{\mathbf{r}}{|\mathbf{r}|}$. The dipole interaction is typically very weak, creating an effective field of no more than a few mT.

3. **Muon-induced quadrupole interaction**: A charged particle near a nucleus will induce an electric field gradient at the nucleus. The interaction of the nuclear electric quadrupole moment with this field gives rise to the quadrupole interaction. Only nuclei with spin greater than 1/2 have a quadrupole moment [21, 22].

(Since this thesis deals exclusively with diamagnetic muonium we are not concerned with the interactions that would be present with the addition of an unpaired electron. These include the electron Zeeman interaction, the hyperfine interaction between the muon and the electron, and the nuclear hyperfine interaction between the electron and neighboring nuclei).

The general spin Hamiltonian is a sum of the above interactions, and has the form

$$\mathcal{H} = \mathcal{H}_Z + \mathcal{H}_D + \mathcal{H}_Q \tag{3.4}$$

where the Zeeman, dipolar, and quadrupole contributions are given by

$$\begin{aligned}\mathcal{H}_Z &= -h\tilde{\gamma}_\mu \mathbf{B}\cdot\mathbf{I} + \sum_i^N -h\tilde{\gamma}_N^i \mathbf{B}\cdot\mathbf{J}^i \\ \mathcal{H}_D &= \sum_i^N \mathbf{I}\cdot\tilde{\mathcal{D}}^i\cdot\mathbf{J}^i \\ \mathcal{H}_Q &= \sum_i^N \mathbf{J}^i\cdot\tilde{\mathcal{Q}}^i\cdot\mathbf{J}^i\end{aligned} \tag{3.5}$$

In the above equations, $\tilde{\gamma}_N^i$ are the nuclear gyromagnetic ratios, $\mathbf{I}$ and $\mathbf{J}^i$ are the spin operators for the muon and ith nucleus respectively, $\tilde{\mathcal{D}}^i$ is the dipole tensor between the muon and ith nucleus, and $\tilde{\mathcal{Q}}^i$ is the nuclear quadrupole tensor for nucleus i. Dipole interactions amongst the nuclear spins J^i are neglected. This Hamiltonian would be appropriate for any diamagnetic center, such as Mu^+ and Mu^- (where the net spin of the two electrons is zero).

We want to write (3.5) in a form that is more practical for analysis purposes. As a result, several assumptions are made to simplify the algebra substantially. First, we assume that the magnetic field $\mathbf{B}$ is oriented along the $\hat{z}$ direction, such that $\mathbf{B} = B\hat{z}$. In addition, we assume that the nuclear electric quadrupole and dipole tensors are axially symmetric about a symmetry axis $\hat{z}'$, which is along the muon-nucleus bond direction (in GaAs, this corresponds to the $\langle 111\rangle$ crystal direction). This axis is positioned at an angle φ from z (i.e. the magnetic field). With these assumptions, the Hamiltonian simplifies to[1]

$$\begin{aligned}\mathcal{H}/h = &-\tilde{\gamma}_\mu B I_z + \sum_i^N -\tilde{\gamma}_N^i B J_z^i \\ &+ \sum_i^N \mathcal{D}^i \left(I_{x'}J_{x'}^i + I_{y'}J_{y'}^i - 2I_{z'}J_{z'}^i\right) \\ &+ \sum_i^N \mathcal{Q}^i \left[J_{z'}^{i2} - \frac{J^i\left(J^i+1\right)}{3}\right]\end{aligned} \tag{3.6}$$

The spin operators along $\hat{z}'$ are related to those in the $\hat{z}$ direction by a rotation trans-

---

[1] Note that the Hamiltonian is divided by h, so that energy has units of frequency (usually expressed in MHz). This is standard practice in μSR, and is the convention used in rest of this thesis.

formation:

$$\begin{aligned} x' &= x\cos\varphi - z\sin\varphi \\ y' &= y \\ z' &= x\sin\varphi + z\cos\varphi \end{aligned} \tag{3.7}$$

The dipolar ($\mathcal{D}^i$) and quadrupole ($\mathcal{Q}^i$) parameters can be calculate from microscopic quantities:

$$\mathcal{D}^i = \frac{\mu_0 h \tilde{\gamma}_\mu \tilde{\gamma}_N^i}{4\pi r_i^3}; \qquad \mathcal{Q}^i = \frac{3V^i_{z'z'} e q^i}{4J^i\left(2J^i - 1\right)} \tag{3.8}$$

where μ_0 is the permeability of free space, r_i is the distance between the muon and the ith nucleus, $V^i_{z'z'}$ is the electric field gradient at the nucleus, and eq^i is the electric quadrupole moment of the nucleus (which is known for any particular nucleus i).

The above Hamiltonian can be used in numerical calculations of the polarization (see Section 3.2). However, the number of nuclei is usually limited to a small number, to avoid lengthy computation times (and because we will usually only need to consider a few nuclei). For example, in the specific case of the level crossing simulations used to fit the data in Chapter 4, we limit the system to a muon and two nuclei, a Ga and an As. The Hamiltonian used in the simulations is explicitly

$$\begin{aligned} \mathcal{H} = &- \tilde{\gamma}_\mu B I_z - \tilde{\gamma}_{Ga} B J_z - \tilde{\gamma}_{As} B K_z \\ &+ \mathcal{D}^{Ga}\left(I_{x'}J^i_{x'} + I_{y'}J^i_{y'} - 2I_{z'}J^i_{z'}\right) \\ &+ \mathcal{D}^{As}\left(I_{x'}K^i_{x'} + I_{y'}K^i_{y'} - 2I_{z'}K^i_{z'}\right) \\ &+ \mathcal{Q}^{Ga}\left(J^{i2}_{z'} - \frac{J^i\left(J^i+1\right)}{3}\right) \\ &+ \mathcal{Q}^{As}\left(K^{i2}_{z'} - \frac{K^i\left(K^i+1\right)}{3}\right) \end{aligned} \tag{3.9}$$

where $\mathbf{J}$ ($\mathbf{K}$), $\tilde{\gamma}_{Ga}$ ($\tilde{\gamma}_{As}$), $\mathcal{D}^{Ga}$ ($\mathcal{D}^{As}$), and $\mathcal{Q}^{Ga}$ ($\mathcal{Q}^{As}$) are the spin matrices, gyromagnetic ratios, dipole, and quadrupole parameters for the Ga (As) nuclei respectively.

3.2 Time-Dependent Muon Polarization

In this section, we derive a formula for calculating the time-dependant muon polarization $\mathbf{P}(t)$ given a spin Hamiltonian $\mathcal{H}$. The polarization is the experimental quantity of interest in any μSR experiment, and is calculated as the expectation value of the muon spin:

$$\mathbf{P}(t) = \langle 2\mathbf{S}_\mu \rangle = \langle \vec{\sigma}^\mu \rangle \tag{3.10}$$

One method to calculate $\mathbf{P}(t)$ explicitly is to use density matrix theory [21, 23]. In density matrix notation,

$$\mathbf{P}(t) = \mathrm{Tr}\left[\rho(t)\vec{\sigma}^\mu\right] \tag{3.11}$$

where $\rho(t)$ is the so-called density matrix, and $\vec{\sigma}^\mu$ are the Pauli matrices corresponding to the muon spin. With the magnetic field along the z-axis, the matrices for the rth component of the muon spin ($r = x,\ y,\ z$) are the usual Pauli matrices for a spin 1/2 particle,

$$\sigma_x^\mu = \begin{pmatrix} 0 & 1 \\ 1 & 0 \end{pmatrix}; \quad \sigma_y^\mu = \begin{pmatrix} 0 & -i \\ i & 0 \end{pmatrix}; \quad \sigma_z^\mu = \begin{pmatrix} 1 & 0 \\ 0 & -1 \end{pmatrix} \tag{3.12}$$

For a Hamiltonian $\mathcal{H}$ with eigenstates $|\,\epsilon_i\rangle$ and corresponding eigenvalues E_i,

$$\mathbf{P}(t) = \mathrm{Tr}\left[\rho(t)\vec{\sigma}^\mu\right] = \sum_i \langle \epsilon_i\,|\rho(t)\vec{\sigma}^\mu|\,\epsilon_i\rangle \tag{3.13}$$

In the Heisenberg representation (which carries the time dependence in the operators),

$$\rho(t) = e^{i\mathcal{H}t/\hbar}\rho(0)e^{-i\mathcal{H}t/\hbar} \tag{3.14}$$

If the initial muon spin is assumed to be 100% polarized in the rth direction and the nuclear spins are unpolarized, then

$$\rho(0) = \frac{1}{K}\left(\mathbf{1} + \sigma_r^\mu\right) \tag{3.15}$$

where $\mathbf{1}$ is the unity operator and K is the dimension of the system in the matrix representation of $\mathcal{H}$. For a system consisting of a muon (with two possible spin states) and N nuclei (each with $2J+1$ possible states), $K = 2(2J+1)^N$. Explicitly then,

$$\mathbf{P}(t) = \frac{1}{K}\sum_i \langle \epsilon_i \left| e^{i\mathcal{H}t/\hbar}\left(\mathbf{1} + \sigma_r^\mu\right) e^{-i\mathcal{H}t/\hbar} \right| \epsilon_i\rangle \tag{3.16}$$

Multiplying the right hand side by $\sum_j |\,\epsilon_j\rangle\langle\epsilon_j| = \mathbf{1}$ and acting with the exponential operators on the appropriate eigenstates, the polarization becomes

$$\begin{aligned}\mathbf{P}(t) &= \frac{1}{K}\sum_i\sum_j e^{-i\omega_{ij}t}\langle\epsilon_i\,|\mathbf{1}+\sigma_r^\mu|\,\epsilon_j\rangle\langle\epsilon_j\,|\vec{\sigma}^\mu|\,\epsilon_i\rangle \\ &= \frac{1}{K}\sum_i\sum_j e^{-i\omega_{ij}t}\left[\langle\epsilon_i\,|\mathbf{1}|\,\epsilon_j\rangle\langle\epsilon_j\,|\vec{\sigma}^\mu|\,\epsilon_i\rangle + \langle\epsilon_i\,|\sigma_r^\mu|\,\epsilon_j\rangle\langle\epsilon_j\,|\vec{\sigma}^\mu|\,\epsilon_i\rangle\right]\end{aligned} \tag{3.17}$$

where we have defined

$$\omega_{ij} = \frac{E_i - E_j}{\hbar} \tag{3.18}$$

The first term in the sum will cancel out to zero, since $\langle\epsilon_i\,|\mathbf{1}|\,\epsilon_j\rangle = \delta_{ij}$ and $\mathrm{Tr}[\vec{\sigma}^\mu] = 0$ for all $\vec{\sigma}^\mu$. Simplification of the second term is simpler with some assumptions. We are always interested in calculating a particular component $P_s(t)$ of the polarization along some axis $\hat{s}$. Although a general formula for $P_s(t)$ can be calculated from (3.17) with $s \neq r$, it is often the case that we wish to calculate the component of the polarization along the initial muon spin (i.e. parallel to $\hat{r}$). In time-integral experiments (such as μLCR) this is always the case; we will therefore assume that $s = r = z$. Thus,

$$\begin{aligned}\langle\epsilon_i\,|\sigma_r^\mu|\,\epsilon_j\rangle\langle\epsilon_j\,|\vec{\sigma}^\mu|\,\epsilon_i\rangle \rightarrow &\ \langle\epsilon_i\,|\sigma_z^\mu|\,\epsilon_j\rangle\langle\epsilon_j\,|\sigma_z^\mu|\,\epsilon_i\rangle \\ &= |\langle\epsilon_i\,|\sigma_z^\mu|\,\epsilon_j\rangle|^2 \\ &= a_{ij}^2\end{aligned} \tag{3.19}$$

remembering that $(\sigma_z^\mu)^\dagger = (\sigma_z^\mu)$.

The double sum over all i and j in (3.17) can be broken into three parts: $j = i$, $j < i$, and $j > i$. Since

$$\begin{aligned}\sum_i\sum_{j<i} &= \sum_j\sum_{i>j} \\ \omega_{ij} &= -\omega_{ji},\end{aligned} \tag{3.20}$$

we can modify the summation indices to obtain

$$P_z(t) = \frac{1}{K}\sum_i a_{ii}^2 + \frac{2}{K}\sum_i\sum_{j>i}\cos\omega_{ij}t \tag{3.21}$$

Simplification of the first term is straightforward. First, we recall that $\sigma_z^2 = 1$. Once again multiplying by the identity operator and taking the trace of both sides:

$$\begin{aligned}\sum_s \sigma_z^\mu \left|\epsilon_s\right\rangle\left\langle\epsilon_s\right| \sigma_z^\mu &= 1 \\ \sum_r\sum_s \left\langle\epsilon_r\right|\sigma_z^\mu\left|\epsilon_s\right\rangle\left\langle\epsilon_s\right|\sigma_z^\mu\left|\epsilon_r\right\rangle &= \sum_r 1 \\ a_{rs}^2 &= K\end{aligned} \tag{3.22}$$

Using this fact, we do the same as above: break $\sum a_{rs}^2$ into three parts and modify the summation indices; the polarization thus simplifies to

$$P_z(t) = 1 - \frac{2}{K}\sum_i\sum_{j>i} a_{ij}^2 + \frac{2}{N}\sum_i\sum_{j>i} a_{ij}^2 \cos\omega_{ij}t \tag{3.23}$$

Combining like terms, we arrive at the final form for the polarization:

$$P_z(t) = 1 - \frac{2}{K}\sum_i\sum_{j>i} a_{ij}^2(1-\cos\omega_{ij}t) \tag{3.24}$$

Although we have assumed that the magnetic field is along z, this formula is still very general. The only other assumptions are based on properties of the Pauli spin matrices, which always hold.

In zero applied field, the muon polarization will "decay" due to the influence of random dipole fields from the surrounding nuclei. Figure 3.1 shows $P_z(t)$ for a single Ga nucleus for different values of $\mathcal{D}^i$. As the dipole interaction increases in strength, the rate of damping of the polarization function increases. (Note that the quadrupole interaction has almost no effect on the rate of decay).

If we are not interested in the time-dependence of the polarization, we will often calculate the time-integral of (3.24) using (2.14). This is a straightforward calculation, giving

$$\bar{P}_z = 1 - \frac{2}{K}\sum_i\sum_{j>i} a_{ij}^2 \times \frac{\omega_{ij}^2}{\omega_{ij}^2 + 1/\tau_\mu^2} \tag{3.25}$$

This is the observable quantity of interest in μLCR experiments, as discussed in the following section.

3.3 Muon Level Crossing Resonance (μLCR)

The muon level crossing resonance (μLCR) technique (also known as quadrupole level crossing resonance and avoided level crossing) is an extremely powerful spectroscopic

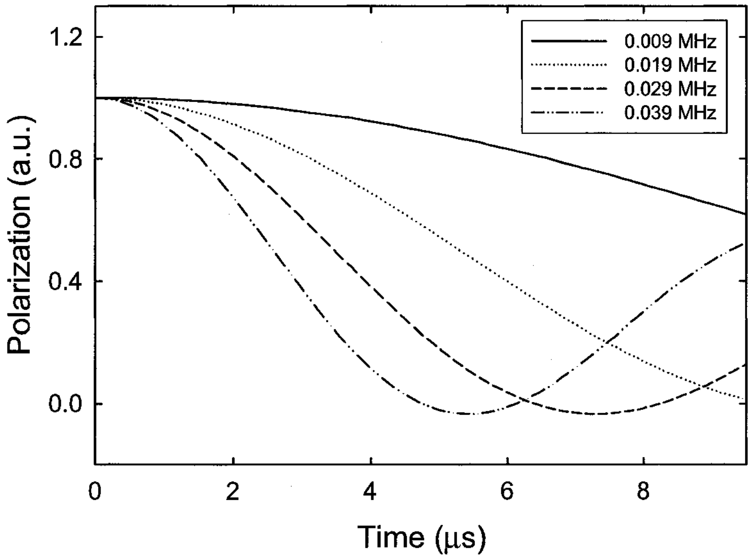

Figure 3.1: Zero field polarization for a single Ga nucleus for various values of the dipole parameter.

μSR technique used to probe the dipole and quadrupole interactions between the muon and surrounding nuclei. In this section, we give an overview of the fundamentals of the level crossing phenomenon which makes this technique so useful. For more details, see [9, 24].

To facilitate the discussion, we will consider a simple system consisting of a diamagnetic muon center (Mu^+ or Mu^-) and a single ^{71}Ga nucleus, both in an applied magnetic field $\mathbf{B}$ assumed to be parallel to $\hat{z}$. We assume that the initial muon spin is applied parallel to the magnetic field, such that $\bar{P}_z = 1$. For most magnetic fields, the Zeeman interaction will dominate the Hamiltonian (i.e. the dipole interaction is "quenched"), and this will remain the case.

Figure 3.2(a) and 3.2(b) shows the simulated energy levels for the muon and Ga nucleus respectively as a function of magnetic field. The muon energy is due exclusively to the Zeeman interaction; there are two levels, separated by an energy difference of $\tilde{\gamma}_\mu B$. The Ga energy levels are similar, except there are four lines since the Ga nucleus is spin 3/2. The presence of the quadrupole interaction acts to increase these levels. (In the absence of the quadrupole interaction, the Ga levels would be considerably smaller than those for the muon, since $\tilde{\gamma}_\mu >> \tilde{\gamma}_{Ga}$).

Let us now consider the energy differences (i.e. the separation between any two

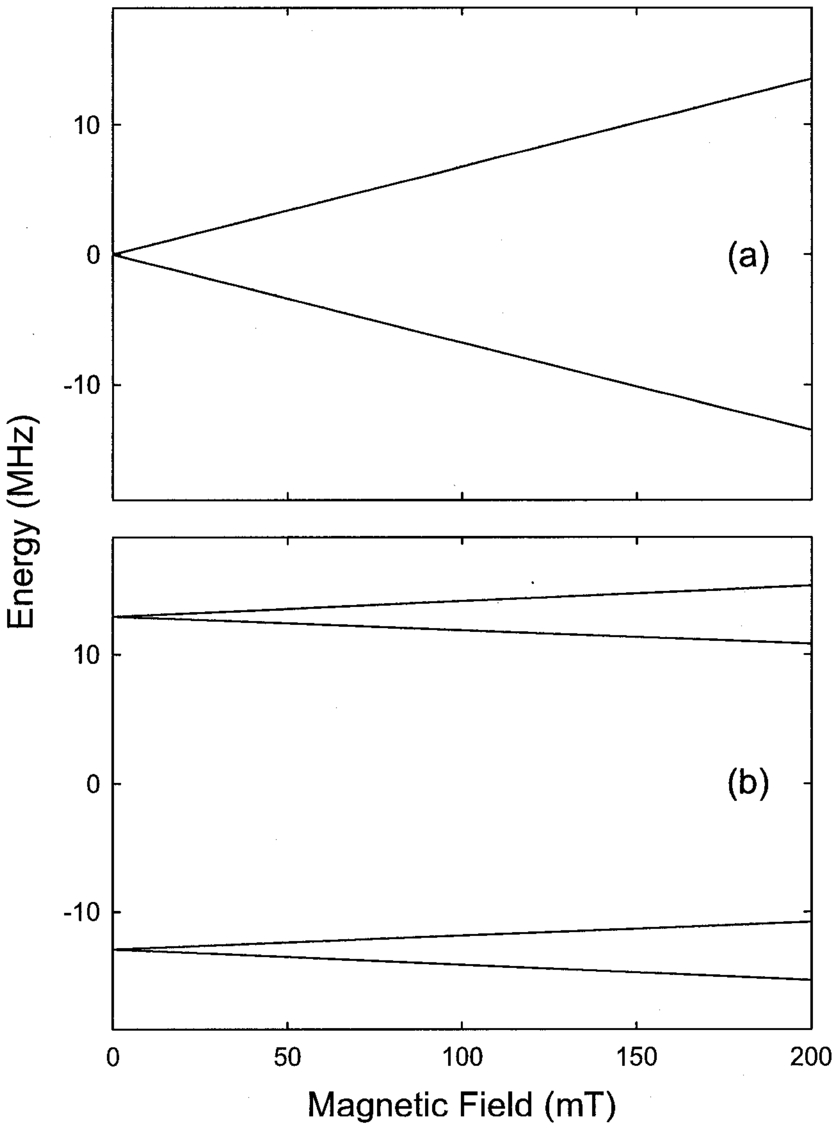

Figure 3.2: Energy levels for (a) the muon, and (b) a ^{71}Ga nucleus as a function of magnetic field, with $\mathbf{B} \parallel \langle 100 \rangle$.

energy levels) for both particles, shown in Figure 3.3(a). The dotted line indicates the energy splitting for the muon; the remaining lines are due to the Ga. For most magnetic fields, these splittings are quite different; however, at certain magnetic fields they can become equal. For example, in the figure, the splittings for both particles cross at 192.0 and 231.0 mT. When this happens, the muon and the nucleus can "talk" to each other via the dipole interaction. As a result, the muon will transfer some of its polarization to the nucleus, resulting in a dip in $\bar{P}_z$. This is known as a level crossing resonance (LCR) and is illustrated in Figure 3.3(b). The position and intensity of these resonances can provide information on the various interactions, allowing estimation of the parameters in the Hamiltonian (such as $\mathcal{Q}^i$, $\mathcal{D}^i$, φ, etc.). From these values, we can then infer the location of the muon and the muon-nuclear separations.

3.4 μLCR Simulations

A large part of the μLCR analysis in Chapter 4 involves the fitting of raw level crossing data to theoretical level crossing spectra. This section discusses the numerical simulation of these spectra. We begin with some technical details, including the process of generating spin matrices and the matrix form of the two-nucleus Hamiltonian (3.9). The step-by-step simulation procedure will be discussed next, including several details that complicate the calculations. Next, the theoretical dependence of resonance lineshapes on the Hamiltonian parameters ($\mathcal{D}^i$, $\mathcal{Q}^i$, φ, etc.) will be discussed. The Mathematica code used in the simulations can be found in Appendix B.

3.4.1 Hamiltonian Matrix Representation

Numerical calculation of the time-integrated polarization (3.25) requires first solving for the eigenvalues and eigenvectors of $\mathcal{H}$. To accomplish this, we must calculate the spin matrices for each particle explicitly in the basis for our system. The elements and dimension of each spin matrix depends explicitly on the size of this basis. The choice of basis is somewhat arbitrary, but one must be careful to remain consistent in all calculations. The basis for the simulations discussed here was taken to be $|\,\mu^+ \text{ Ga As}\rangle$; the dimension of the Hamiltonian will therefore be $d = 2 \times 4 \times 4 = 32$.

Let the single particle state space for the muon, Ga, and As be S_μ, S_{Ga}, and S_{As} respectively. In the two dimensional space of the muon (spin 1/2), the spin matrices are just the Pauli matrices given in (3.12). We can derive four dimensional matrices for the

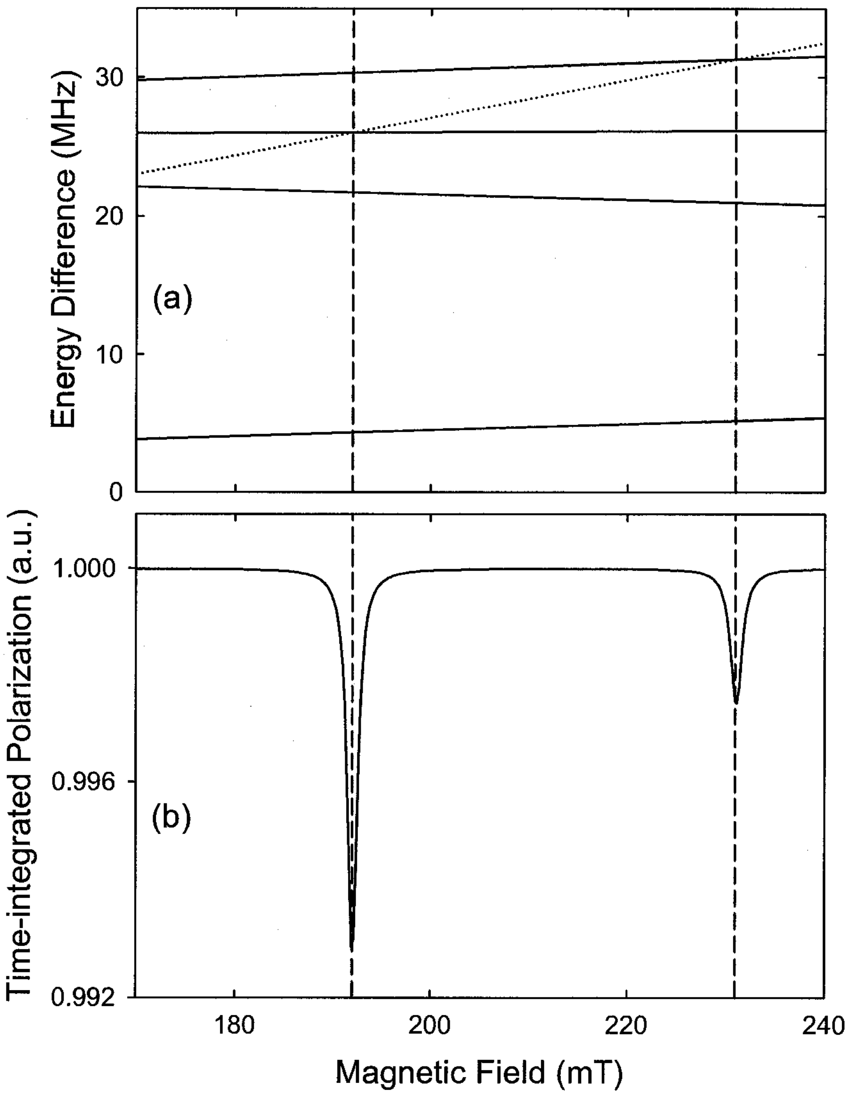

Figure 3.3: (a) Energy splittings for the muon (dotted line) and ^{71}Ga nucleus (dashed lines). (b) Time-integrated muon polarization. Vertical dashed lines indicate position of level crossing resonances.

nuclei (spin 3/2):

$$j_x = \frac{1}{2}\begin{pmatrix} 0 & \sqrt{3} & 0 & 0 \\ \sqrt{3} & 0 & 2 & 0 \\ 0 & 2 & 0 & \sqrt{3} \\ 0 & 0 & \sqrt{3} & 0 \end{pmatrix}$$

$$j_y = \frac{1}{2}\begin{pmatrix} 0 & -i\sqrt{3} & 0 & 0 \\ i\sqrt{3} & 0 & -2i & 0 \\ 0 & 2i & 0 & -i\sqrt{3} \\ 0 & 0 & i\sqrt{3} & 0 \end{pmatrix} \tag{3.26}$$

$$j_z = \frac{1}{2}\begin{pmatrix} 3 & 0 & 0 & 0 \\ 0 & 1 & 0 & 0 \\ 0 & 0 & -1 & 0 \\ 0 & 0 & 0 & -3 \end{pmatrix}$$

The composite state space for the complete three-particle system can be expressed as a direct product between the three single-particle spaces:

$$S = S_\mu \otimes S_{Ga} \otimes S_{As} \tag{3.27}$$

where the '$\otimes$' symbol represents the tensor product. In the framework of our numerical simulations, these products can be expressed as something called the matrix direct product (MDP). Consider two matrices **A** and **B**, with dimensions $(m \times n)$ and $(p \times q)$ respectively. Their matrix direct product **C** is an $(mp) \times (nq)$ matrix given by $\mathbf{C} = \mathbf{A} \otimes \mathbf{B}$. As an example, let **A** and **B** be 2×2. Their product is a 4×4 matrix

$$\mathbf{C} = \begin{pmatrix} a_{11}\mathbf{B} & a_{12}\mathbf{B} \\ a_{21}\mathbf{B} & a_{22}\mathbf{B} \end{pmatrix} = \begin{pmatrix} a_{11}b_{11} & a_{11}b_{12} & a_{12}b_{11} & a_{12}b_{12} \\ a_{11}b_{21} & a_{11}b_{22} & a_{12}b_{21} & a_{12}b_{22} \\ a_{21}b_{11} & a_{21}b_{12} & a_{22}b_{11} & a_{22}b_{12} \\ a_{21}b_{21} & a_{21}b_{22} & a_{22}b_{21} & a_{22}b_{22} \end{pmatrix} \tag{3.28}$$

For programming purposes, the MDP is easily represented in Mathematica by associating

$\otimes$ with the following function:

```
<<LinearAlgebra‘MatrixManipulation‘;
a_List?MatrixQ⊗b_List?MatrixQ := BlockMatrix[Outer[Times,a,b]];
```

As an example, let us consider the spin matrices representing the three components of the muon angular momentum in S (in the notation of our Hamiltonian, these matrices are labeled as $\mathbf{I}$). They are constructed as follows:

$$\begin{aligned} I_x &= \frac{\sigma_x}{2} \otimes I_4 \otimes I_4 \\ I_y &= \frac{\sigma_y}{2} \otimes I_4 \otimes I_4 \\ I_z &= \frac{\sigma_z}{2} \otimes I_4 \otimes I_4 \end{aligned} \tag{3.29}$$

where I_4 is the 4×4 identity matrix. Similarly, the composite spin matrices for the Ga nucleus can be constructed as follows:

$$\begin{aligned} J_x &= I_2 \otimes j_x \otimes I_4 \\ J_y &= I_2 \otimes j_y \otimes I_4 \\ J_z &= I_2 \otimes j_z \otimes I_4 \end{aligned} \tag{3.30}$$

where I_2 is the 2×2 identity matrix, and j_i are given in (3.26)[2]. Construction of the matrices for the As nuclei are done in a similar fashion. This technique can easily be extended to more than two nuclei, as long as order of operations is carefully observed.

3.4.2 Complications

Before discussing the actual simulation procedure, it is useful to first cover a couple points which complicate the simulations somewhat:

- Although the ^{75}As is 100% abundant, there are two distinct isotopes of Ga inside the lattice: ^{71}Ga (which is 39.8% abundant) and ^{69}Ga (which is 60.2% abundant). The differing values of $\tilde{\gamma}_N$ and eq^i (shown in Table 3.2) will lead to different dipole and quadrupole interactions with the muon respectively. As a result, we must account for the possibility that either nucleus could be a nearest neighbor to the muon. This is accomplished by constructing a separate Hamiltonian for each isotope; these Hamiltonians are identical, aside from the different parameters which

---

[2] Note that lowercase letters are used to represent the single-particle matrices, whereas uppercase are used to represent the composite matrices in the three-particle basis.

Orientation	φ (Degrees)	Number of equivalent nuclei
$\langle 100 \rangle$	54.74	4
$\langle 110 \rangle$	35.26	2
	90	2
$\langle 111 \rangle$	0	1
	70.53	3

Table 3.1: Angles φ between the nearest neighbor bond direction and magnetic field for **B** parallel to $\langle 100 \rangle$, $\langle 110 \rangle$, and $\langle 111 \rangle$, for a muon at the BC site.

Nucleus	$\tilde{\gamma}_N$ (μs^{-1} T^{-1})	eq^i (Cm^{-2})
^{71}Ga	12.984	0.112
^{69}Ga	10.219	0.178
^{75}As	7.292	0.3

Table 3.2: Gyromagnetic ratios and nuclear electric quadrupole moments for Ga and As nuclei.

are input. The eigenvalues and eigenvectors, as well as the corresponding polarization, must be calculated separately for each Hamiltonian. The "net" polarization is then calculated by taking a sum weighted by the isotopic abundance of each nucleus.

- For any particular orientation of **B** with respect to the lattice, there are four possible nearest neighbor bonds, each of which is at some angle to the magnetic field. The possible angles for three important orientations are shown in Table 3.1 (assuming the muon is at the BC site, which will be justified in the next chapter). For each of the Hamiltonians mentioned above, we must therefore calculate the polarization for each possible angle, and once again take a weighted sum (which this time is the "angular abundance").

3.4.3 Simulation Procedure

Below, the step-by-step procedure for simulating μLCR spectra will be briefly outlined:

1. Spin matrices for the muon, Ga, and As are calculated using the MDP prescription discussed in Section 3.4.1.

2. All spin matrices are transformed into the primed coordinate system, as per (3.7). At this stage, the matrices now contain the variable φ, which will eventually need to be substituted explicitly.

3. Hamiltonians for the Zeeman ($\mathcal{H}_{\mathcal{Z}}$), dipole ($\mathcal{H}_{\mathcal{D}}$), and quadrupole ($\mathcal{H}_{\mathcal{Q}}$) interactions are constructed. (The matrices now contain a second variable, the magnetic field B).

4. The total spin Hamiltonian is constructed by adding the three interactions; we now have two Hamiltonians, one for each isotope of Ga ($\mathcal{H}^{71}$ and $\mathcal{H}^{69}$). These matrices differ only by the values of $\tilde{\gamma}_N$, $\mathcal{D}^i$, and $\mathcal{Q}^i$ input for each isotope.

5. At this stage, we can now calculate $\bar{P}_z$. An appropriate range for B is set, as well as the number of points n which will be simulated. Care must be taken to choose an appropriate value for n: too few points results in an inaccurate lineshape, while too many can make the computation time cumbersome. For a field range of 100 mT or so, $200 - 300$ points is generally sufficient, resulting in a simulation time of a few minutes. For each field point B in the scan, we must do the following:

   (a) Each of the two isotopic Hamiltonians is calculated explicitly for each of the possible angles, and at three different magnetic fields: B and $B \pm \Delta^{\pm}$, where $\Delta^{\pm}$ are the so-called flip fields (the reason for doing this is discussed in detail in Chapter 4). As a result, we must calculate up to 12 separate Hamiltonians.

   (b) $\bar{P}_z(B, i, \varphi)$ is calculated for each individual case, where i represents the Hamiltonian for a particular isotope of Ga. Assuming there are two possible angles φ_1 and φ_2, the net polarization for each angle is

$$\begin{aligned} \bar{P}_z(B, \varphi_1) &= A_{71}\bar{P}_z(B, 71, \varphi_1) + A_{69}\bar{P}_z(B, 69, \varphi_1) \\ \bar{P}_z(B, \varphi_2) &= A_{71}\bar{P}_z(B, 71, \varphi_2) + A_{69}\bar{P}_z(B, 69, \varphi_2) \end{aligned} \tag{3.31}$$

   where A_i represents the respective abundances of the Ga isotopes.

   (c) The μLCR spectra is also calculated. This is simply the difference between polarizations at $B+\Delta^+$ and $B-\Delta^-$. Representing this difference by D:

$$\begin{aligned}
D(B,\varphi_1) &= A_{71}\left[\bar{P}_z(B+\Delta^+,71,\varphi_1)-\bar{P}_z(B-\Delta^-,71,\varphi_1)\right]\\
&\quad + A_{69}\left[\bar{P}_z(B+\Delta^+,69,\varphi_1)-\bar{P}_z(B-\Delta^-,69,\varphi_1)\right]\\
D(B,\varphi_2) &= A_{71}\left[\bar{P}_z(B+\Delta^+,71,\varphi_2)-\bar{P}_z(B-\Delta^-,71,\varphi_2)\right]\\
&\quad + A_{69}\left[\bar{P}_z(B+\Delta^+,69,\varphi_2)-\bar{P}_z(B-\Delta^-,69,\varphi_2)\right]
\end{aligned} \tag{3.32}$$

where we have once again weighted the sum by the isotopic abundances. To obtain the final values for $\bar{P}_z$ and D, we now weight the sum by the relative abundances of φ_1 and φ_2 (a_1 and a_2 respectively):

$$\begin{aligned}
\bar{P}_z(B) &= a_1\bar{P}_z(B,\varphi_1)+a_2\bar{P}_z(B,\varphi_2)\\
D(B) &= a_1 D(B,\varphi_1)+a_2 D(B,\varphi_2)
\end{aligned} \tag{3.33}$$

These two numbers are calculated for each field point B in the range of the simulation.

6. Once the polarization and/or resonance lineshape has been calculated, a number of things can be done. Typically, the simulations are automatically plotted over the experimental data in order to aid in fitting, and exported to raw text files for import into an external plotting package.

This procedure can be easily modified to account for changes in the system, such as rotating the magnetic field (which can result in four unique angles, instead of the two discussed above).

3.4.4 Parameter Dependence

The Hamiltonian given by (3.9) depends on three main parameters: the bond angle φ, dipole parameter $\mathcal{D}^i$, and quadrupole parameter $\mathcal{Q}^i$. In this section we will discuss how LCRs depend on each of these.

Bond Angle

Figure 3.4(a) shows $\bar{P}_z$ for a ^{75}As nucleus at a variety of bond angles with $\mathbf{B} \parallel \langle 100\rangle$. Changing the angle has two main effects: (1) the positions of the LCRs change, and (2) the separation between the main resonance and its high-field companion changes. As the angle is increased, we see that the separation increases. This is illustrated more clearly in Figure 3.4(b), which shows the same polarization curves as the first part of the graph, but shifted so that the positions of the main resonance are the same. Both the absolute shift and separation of the large and small resonance can hence be used to determine φ.

Quadrupole Parameter

We saw in Section 3.3 that the position of a level crossing resonance depends on the field at which the level splittings between the muon and nucleus match. This is determined not only by the Zeeman interaction of each particle, but on the quadrupole interaction as well. As a result, we would expect that the position of a resonance should depend strongly on the quadrupole parameter $\mathcal{Q}$. Figure 3.5(b) shows the dependence of the LCR position on $\mathcal{Q}$, for a ^{71}Ga nucleus with $\mathbf{B} \parallel \langle 100 \rangle$. (Figure 3.5(a) shows $\bar{P}_z$ for various values of the quadrupole parameter). The position varies linearly with $\mathcal{Q}$. The shift in position is due to the fact that as the quadrupole interaction changes, the energy levels (and energy splittings) will also change; this in turn shifts the field at which the LCR occurs.

Dipole Parameter

The amount of polarization transferred to the nucleus at a LCR depends on the strength of the dipole coupling. As a result, the larger $\mathcal{D}$ becomes (corresponding to a decrease in the muon-nuclear separation r), the more intense the resulting LCR will be. This is shown in Figure 3.6(a), where we see $\bar{P}_z$ for a variety of values for $\mathcal{D}$ (the graphs have been shifted vertically for clarity). Figure 3.6(b) shows the dependence of the maximum polarization lost (i.e. the minimum of $\bar{P}_z$) on the dipole parameter.

Since the quadrupole and Zeeman energies for Ga and As are very different, it is generally assumed that the resonances due to nuclei of different species are independent of each other. Explicitly, there *is* a small dependence; for example, as $\mathcal{D}^{71}$ is altered, there will be a small change in the amplitude of the ^{75}As LCR along that same orientation (the position is unaffected). This is illustrated in Figure 3.7, where $\bar{P}_z$ for the ^{75}As nuclei is plotted for various values of $\mathcal{D}^{71}$ with $\mathbf{B} \parallel \langle 111 \rangle$. We see that there is a small change in $\bar{P}_z$; however, if the interactions are weak (which is certainly the case for GaAs), then this affect can generally be ignored. This is one of the main assumptions made during the fitting of the μLCR data discussed in Chapter 4.

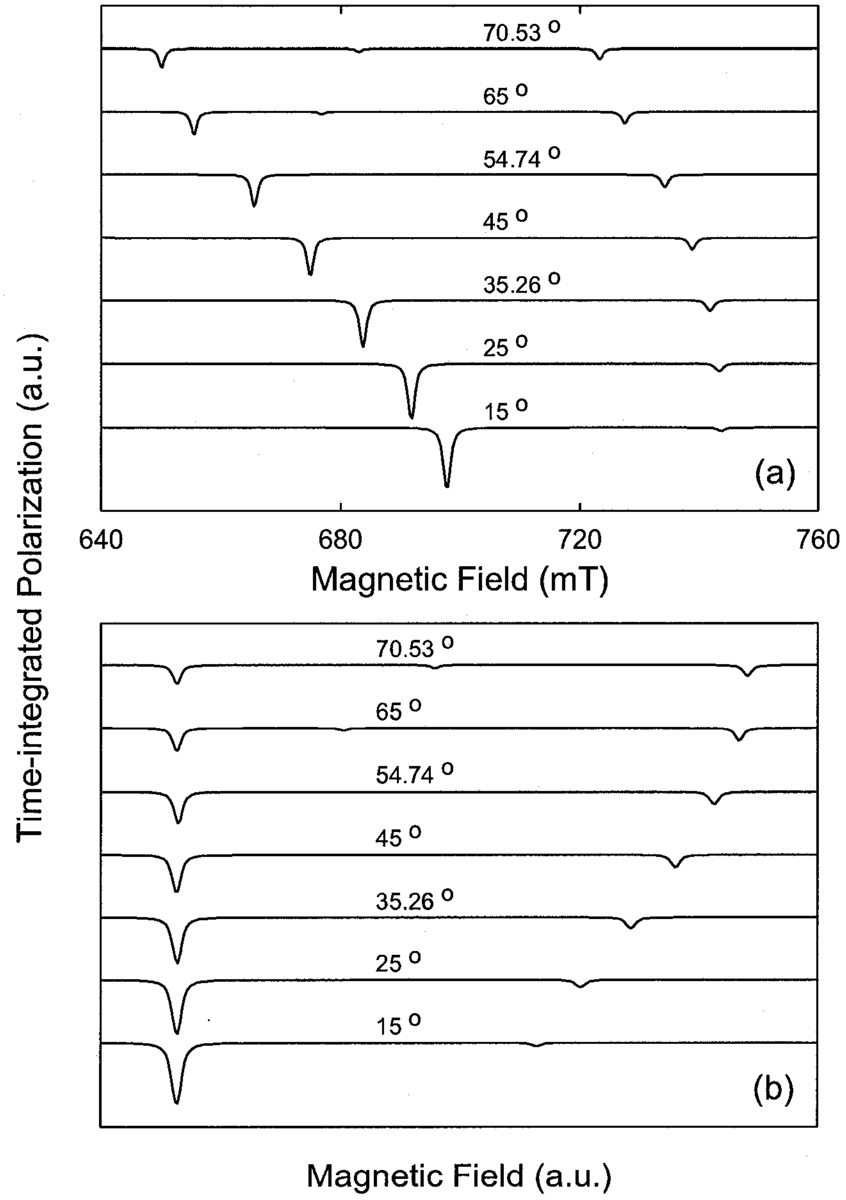

Figure 3.4: (a) $\bar{P}_z$ with $\mathbf{B} \parallel \langle 100 \rangle$ for a ^{75}As nucleus for various angles φ. (b) Same time-integrated polarization, shifted to more clearly show change in separation between LCRs.

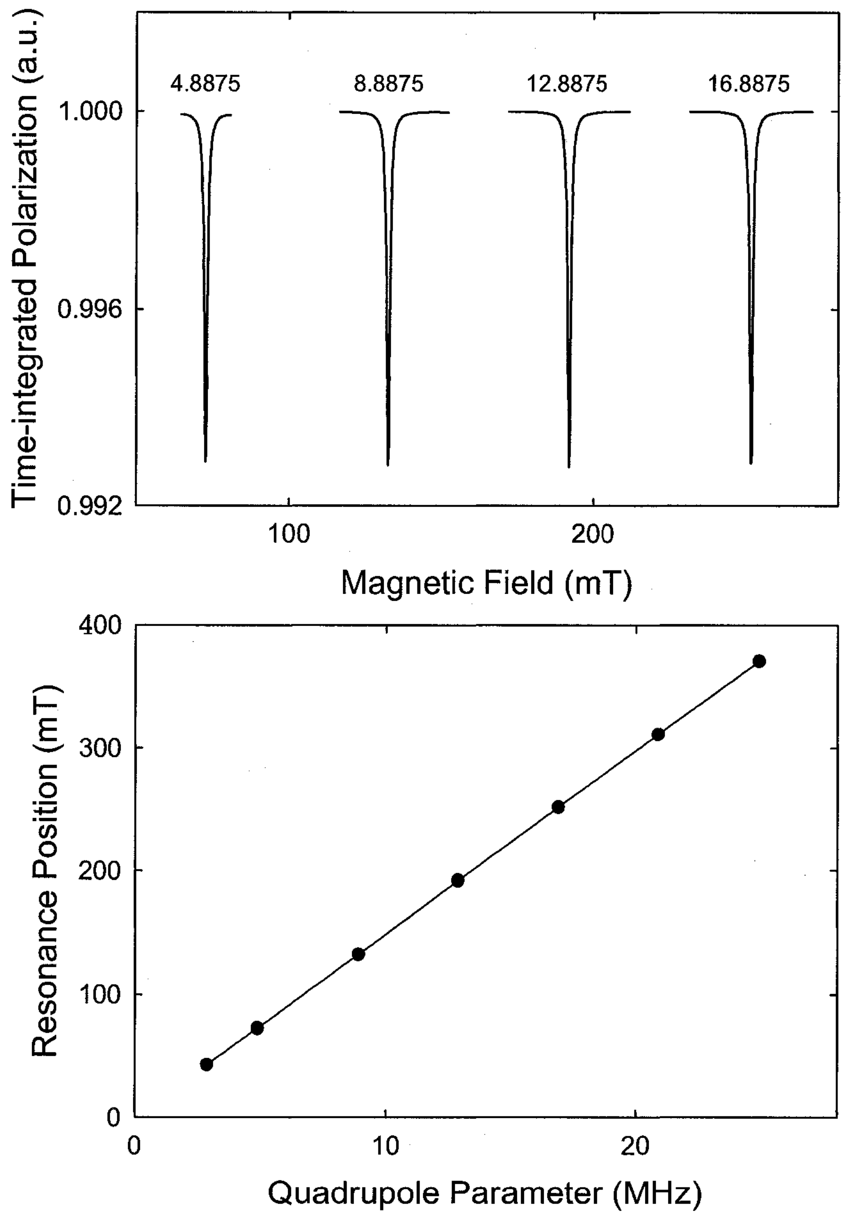

Figure 3.5: (a) $\bar{P}_z$ for a ^{71}Ga nucleus with $\mathbf{B} \parallel \langle 100 \rangle$ for (left to right): $Q^{71} = 4.8875$, $Q^{71} = 8.8875$, $Q^{71} = 12.8875$, and $Q^{71} = 16.8875$ MHz. (b) Dependence of resonance position on Q^{71}. Solid line is a linear fit to the data.

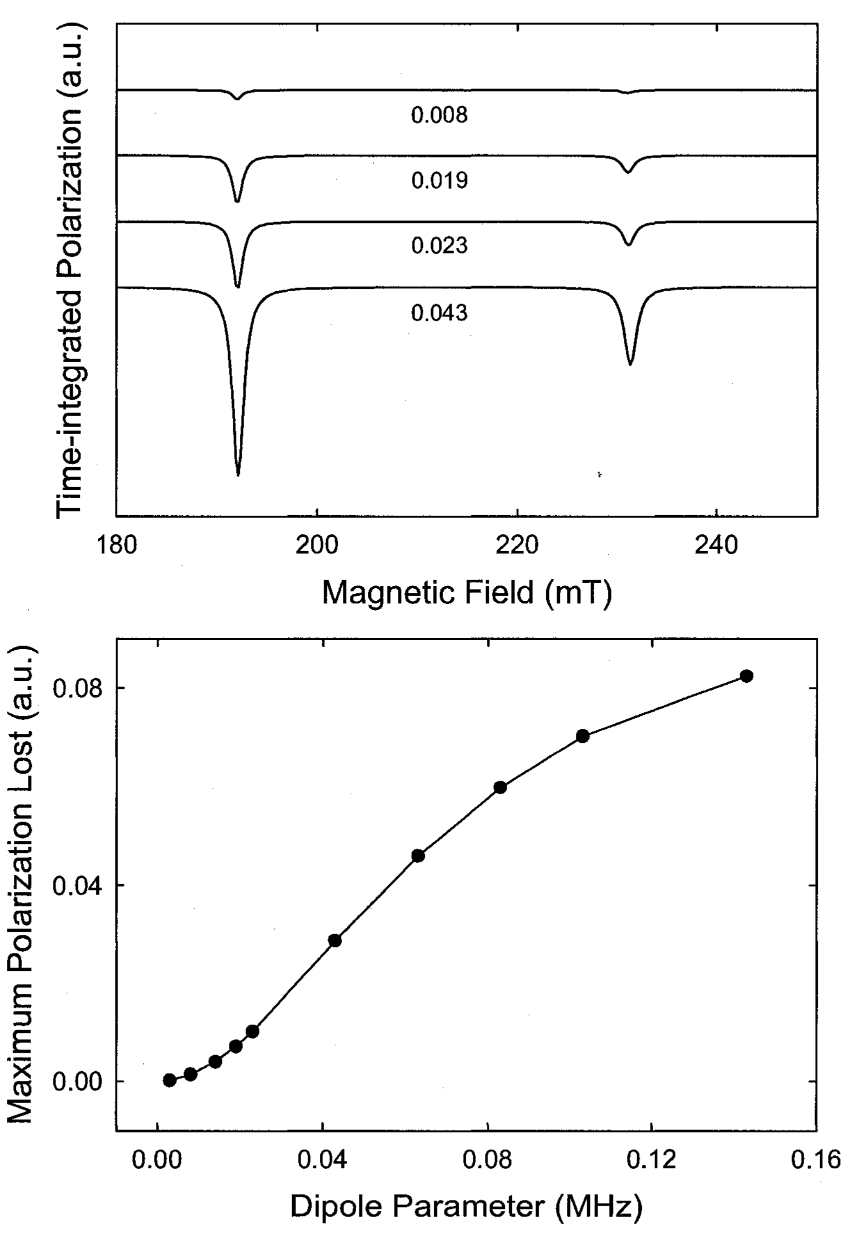

Figure 3.6: (a) $\bar{P}_z$ for a ^{71}Ga nucleus with $\mathbf{B} \parallel \langle 100 \rangle$ for (top to bottom): $\mathcal{D}^{71} = 0.008$, $\mathcal{D}^{71} = 0.019$, $\mathcal{D}^{71} = 0.023$, and $\mathcal{D}^{71} = 0.043$ MHz. (b) Maximum amount of $\bar{P}_z$ transferred to nucleus for various values of $\mathcal{D}^{71}$.

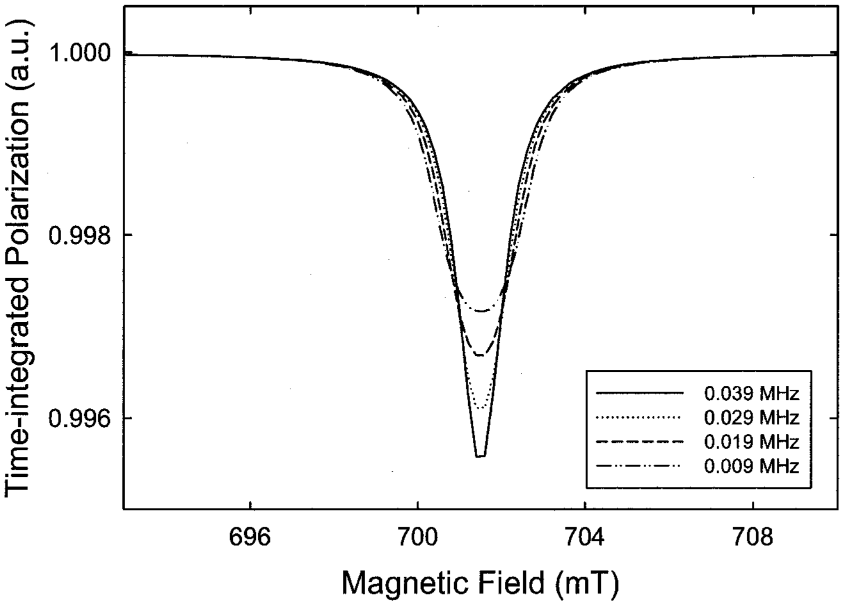

Figure 3.7: ^{75}As LCR with $\mathbf{B} \parallel \langle 111 \rangle$ for various values of $\mathcal{D}^{71}$.

3.5 Transverse-Field Depolarization

Let us consider a transverse field setup, where the muon spin is initially perpendicular to the applied field $\mathbf{B}_{app}$. We saw in Chapter 2 that this will lead to a precession of the muon spin about the field. If the applied field was the only one present (e.g. the muon was in a vacuum, or a sample where nuclear spins are zero), then every implanted muon would precess at the exact same frequency (the Larmor frequency) given by

$$\omega_\mu = \frac{\tilde{\gamma}_\mu}{B_{app}} \tag{3.34}$$

The TF signal would thus be a sinusoidal function with frequency ω_μ, which would oscillate "forever"; i.e. there would be no damping or relaxation of the signal. (We have ignored any possible inhomogeneities in the applied field across the width of the sample). However, inside a sample which has nuclei with non-zero spins (such as GaAs), the situation is very different. The net field will now be given by $\mathbf{B} = \mathbf{B}_{app} + \mathbf{B}_{dip}$, where $\mathbf{B}_{dip}$ is the field due to the presence of nuclear dipoles. If we assume that the nuclear spins are static and randomly oriented, then the dipole field will be slightly different for each implanted muon. This will lead to a spread in fields around B_{app} (and a corresponding spread in frequencies around ω_μ). This frequency distribution results in a relaxation (or depolarization) of the muon signal [as seen in Figure 2.3(b)]. In GaAs, this relaxation is phenomenologically well described by a Gaussian damping function $\exp(-\sigma^2 t^2)$ [8], where the relaxation (or depolarization) rate σ controls how quickly the signal relaxes.

When analysing TF data in this thesis, the parameter of interest is usually σ. If the system being studied contains a large number of nuclei, exact calculation of the polarization using the Hamiltonian can be cumbersome. Fortunately, σ can be calculated from secular contributions to the Hamiltonian (that is, terms which change the muon Zeeman energy to first order). It can be shown [25] that σ is proportional to the second moment [22] M_2 of the field distribution. Let us consider the single nucleus Hamiltonian

$$\mathcal{H} = -\tilde{\gamma}_N B J_z + \mathcal{Q}\left[J_{z'}^2 - \frac{J(J+1)}{3}\right] \tag{3.35}$$

The form of the eigenfunctions $|u_k\rangle$ depends on the strength of the magnetic field [26]. At high fields where the Zeeman interaction dominates, the field direction $\hat{z}$ is a good axis of quantization, and the basis set $|m_J\rangle$ are eigenfunctions of (3.35). At low fields, where the Zeeman interaction is weaker than (or comparable to) the quadrupole interaction, this is no longer the case. By calculating the expectation value of the secular dipole Hamiltonian, we can express the second moment as [27]

$$\begin{aligned} M_2 = \frac{1}{2J+1}\sum_k \left(\frac{\mu_0 h\tilde{\gamma}_N}{4\pi r^3}\right)^2 & \left[\langle u_k\,|J_z|\,u_k\rangle\left(3\cos^2\varphi - 1\right)\right. \\ & \left. + \langle u_k\,|J_x|\,u_k\rangle 3\cos\varphi\sin\varphi\right]^2 \end{aligned} \tag{3.36}$$

where the sum extends over the $2J+1$ eigenstates of the single nucleus Hamiltonian. Second moments are additive, so we need only consider the moment for a single nucleus, and then multiply by the number of equivalent nuclei. Summing over all nuclei, we can then calculate the relaxation rate from the second moment:

$$\sigma^2 = \frac{\tilde{\gamma}_N^2 M_2}{2} \tag{3.37}$$

Figure 3.8 shows the field dependence of σ for a variety of angles. (This is known as a Hartmann quenching curve). In the high field limit, (3.36) reduces to the field-independent Van Vleck expression for the dipole coupling [28]:

$$M_2 = \left(\frac{\mu_0 h\tilde{\gamma}_N}{4\pi r^3}\right)^2 \frac{\left(3\cos^2\varphi - 1\right)^2}{r^6}\frac{J(J+1)}{3} \tag{3.38}$$

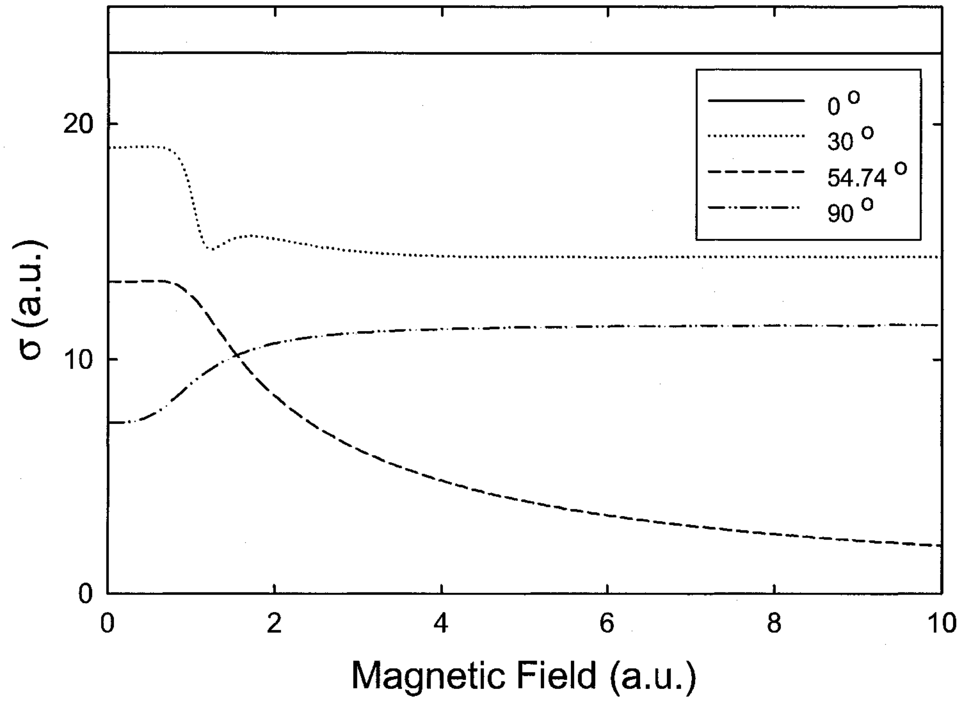

Figure 3.8: Field dependence of the transverse field relaxation σ as a function of φ for a system consisting of a muon and a single spin 3/2 nucleus.

For $\varphi = 54.74°$, M_2 will go to zero as $3\cos^2\varphi - 1$ does the same. This results in a prominent drop in σ for this angle. This field dependence will be utilized in Chapter 4 to aid in the search for level crossing resonances in GaAs, and also in Chapter 5 to enable one to distinguish between Mu^+ and Mu^-.

Chapter 4

Structure of Mu^+ in p-type GaAs

In this Chapter, we discuss the μLCR experiments conducted on heavily-doped p-type GaAs. The goal of these experiments was to determine the local structure of Mu^+, as was done for Mu^- in n-type GaAs [16]. To characterize the structure of a muonium center, we need to:

1. Identify the nearest neighbor host atom(s).
2. Determine the symmetry of the neighbors with respect to the muon (i.e. the orientation of the neighbors with respect to the muon and applied magnetic field).
3. Estimate the separation between the muon and nearest neighbors.

This information will allow us to assign the muon to a particular site in the lattice. In this Chapter we will discuss how this is accomplished. The main results in this chapter have also been accepted for publication [29].

In Section 4.1 the μLCR experimental method will be discussed, including a brief description of the equipment used and samples studied. This is followed in Section 4.2 by a discussion of the procedure used to locate the level crossing resonances (LCRs). A detailed qualitative and quantitative analysis of these resonances will be given in Section 4.3. Numerical estimates for the muon-nuclear separation will be calculated, and compared to existing theoretical calculations for H^+ in GaAs.

4.1 Experimental

Experimentally, a level crossing experiment involves measuring the time-integrated muon polarization $\bar{P}_z$ as a function of magnetic field, looking for dips which are characteristic of a level crossing. (Refer to Section 3.3 for more information on the level crossing phenomenon). This can entail a lengthy experiment, because (1) we must first locate a resonance, and (2) scan that resonance in detail to improve the signal-to-noise. Since the polarization lost to the nucleus through cross relaxation can be very small, this requires very high decay statistics.

A μLCR experiment utilizes a standard time-integral LF setup, with two counters (forward and back) used to collect data. If the signal is weak, we must be concerned with fluctuations of the muon beam. Such fluctuations could potentially wash out the signal we are interested in studying. To account for this, a field modulation technique is utilized, whereby small "flip" fields ($\Delta^{\pm} \approx 2$ mT) are applied parallel or antiparallel to the main field $\mathbf{B}$. The flip fields will act to increase or decrease the net field, and data are collected at both points. The signal is then plotted as a difference in asymmetry between the two points:

$$\Delta A = A^{+} - A^{-} \tag{4.1}$$

where $A^{\pm} = A(B \pm \Delta^{\pm})$. The asymmetry at a particular magnetic field B is given by

$$A(B) = \frac{\eta_B(B) - \eta_F(B)}{\eta_B(B) + \eta_F(B)} \tag{4.2}$$

where $\eta_{B,F}$ are the total time-integrated counts in the backward and forward counters, as defined in (2.13). A combination of this type will average out any systematic effects on the asymmetry introduced by beam fluctuations, and leads to the distinctive derivative-like lineshape seen in LCR data. This is illustrated in Figure 4.1.

All three spectrometers listed in Section 2.2 were used to generate the required magnetic fields and collect the data. In addition, a variety of other equipment was required to run the experiments:

- Cryostats are used to cool the sample down to the necessary temperatures (in the case of our μLCR data, 50 K). We used both cold finger (CF) and horizontal gas flow (HGF) cryostats from Cryo Industries. Both cryostats have axial access for sample insertion, and a temperature range of 2.8–330 K.
- The temperature of both the sample and cryostat diffuser were controlled by Lakeshore 330/331 autotuning temperature controllers. Accurate measurement of the temperature was accomplished using a variety of sensors, primarily made from Pt and AlGaAs.
- Special sample rods/holders are required to mount the sample inside the cryostat.

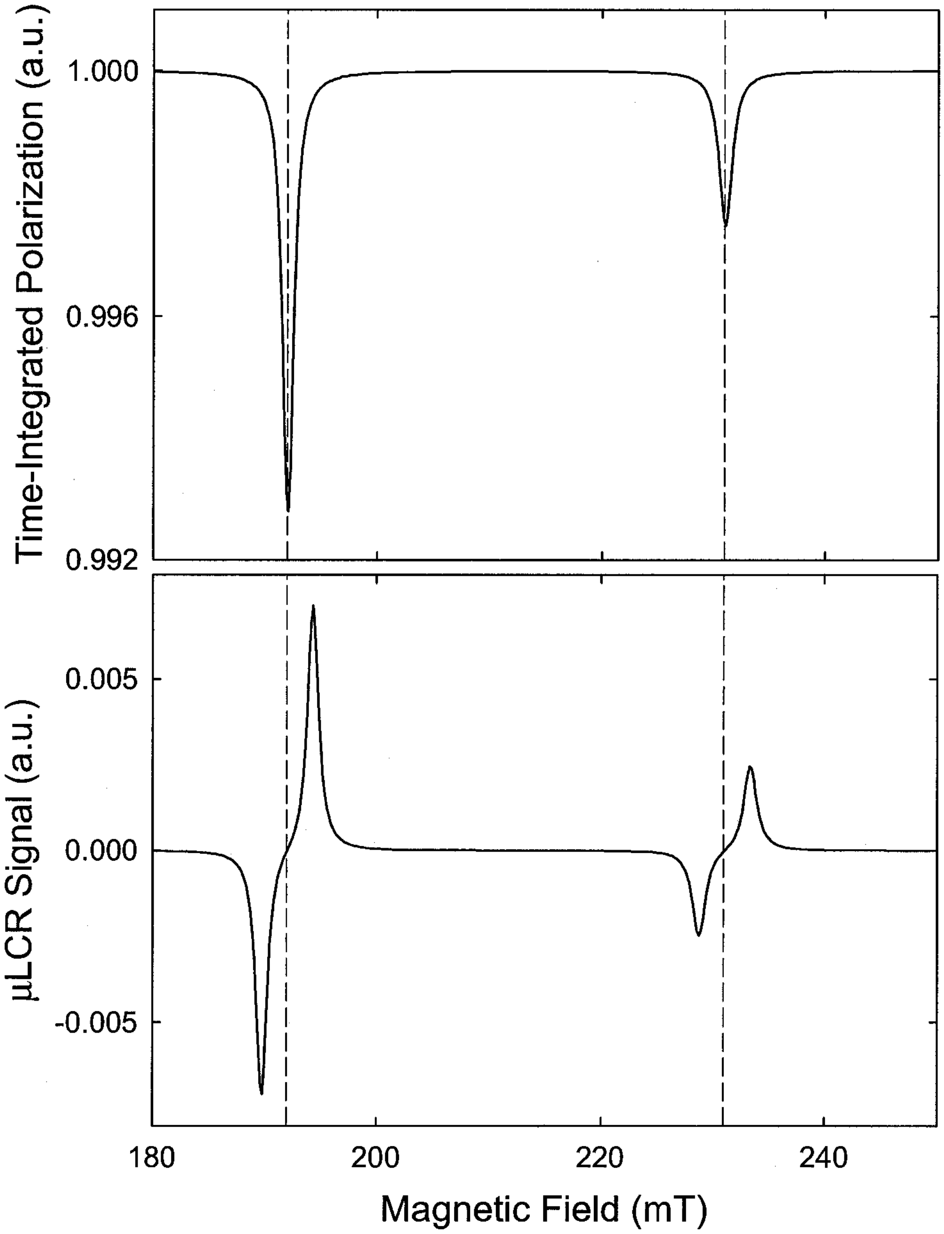

Figure 4.1: (a) Time-integrated polarization with $\mathbf{B} \parallel \langle 100 \rangle$. (b) μLCR signal after applying flip fields of $\Delta^{\pm} \approx 2$ mT.

Sample	Company	Orientation	Dopant Concentration (cm^{-3})	Approx. Size $l \times w \times t$ (mm)
GaAs–p1	CSI	$\langle 100\rangle$	$1.84 - 4.37 \times 10^{19}$	$25 \times 25 \times 0.35$
GaAs–p2	Laser Diode	$\langle 100\rangle$	2.8×10^{19}	$25 \times 25 \times 0.35$
GaAs–p3	Atomergic	$\langle 111\rangle$	4×10^{18}	$25 \times 25 \times 0.35$

Table 4.1: Heavily-doped p-type GaAs:Zn samples used for the μLCR experiments.

The HGF cryostat uses a long metal rod with a silver plate at one end to attach the sample to. The CF cryostat uses a copper holder which provides good thermal conductance. Samples are attached to the holders using a combination of plastic wrap, Mylar foil, thermal grease, and Mylar tape.

The p-type GaAs samples studied are listed in Table 4.1. All three wafers were heavily doped with Zn, with concentrations on the order of 10^{18}–10^{19} cm^{-3}. All samples were cut to approximately the same size (≈ 625 mm^2) to allow mounting and insertion into the cryostats. The $\langle 100\rangle$ and $\langle 111\rangle$ wafers were used to collect data along those respective orientations; the $\langle 110\rangle$ data were done with samples GaAs–p1 and GaAs–p2 rotated in an appropriate fashion with respect to $\mathbf{B}$.

4.2 Location of Level Crossing Spectra

Prior to starting these experiments, it was extremely difficult to anticipate where LCRs for Mu^+ would be located (or if they could be found at all). Theoretical estimates of the quadrupole parameter would have been helpful, but such calculations are difficult and do not exist. In principle, we could simply perform magnetic field scans over some large range in the hopes of getting "lucky". However, this is not practical given the time consuming nature of the μLCR technique. (Most μLCR scans take a minimum of 12–24 hours). Therefore, we require some way to define a reasonable initial scan region that does not require extensive beamtime.

Fortunately, some guidance for where to hunt for μLCRs came from previous experiments conducted on GaAs:Zn [15], which studied the behavior of the transverse field relaxation σ as a function of magnetic field for $\mathbf{B} \parallel \langle 100\rangle$. A reproduction of these data are shown in Figure 4.2 (recall from Chapter 3 that this is known as a Hartmann quenching curve). The data show a strong dependence on field: the relaxation is constant until

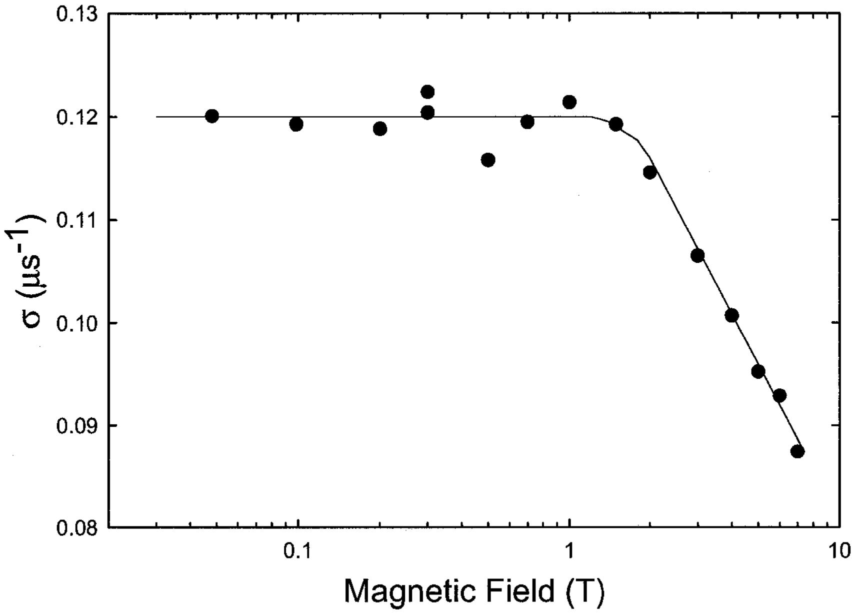

Figure 4.2: Relaxation of the transverse field signal for Mu$^+$ at various magnetic fields with $\mathbf{B} \parallel \langle 100 \rangle$. Reproduced from [15].

approximately 2 Tesla, where it begins to quickly drop off as the field is increased. The crossover field where this occurs (B_{cr}) acts as a "boundary" between the so-called low and high field regions, where the quadrupole and nuclear Zeeman interactions dominate respectively. At the crossover field the two interactions are comparable. Hence,

$$\mathcal{Q} \approx \tilde{\gamma}_N B_{cr}. \tag{4.3}$$

In addition, we know that LCRs occur at fields where the energy splittings due to the muon Zeeman interaction match those due to the nuclear quadrupole interaction (ignoring the nuclear Zeeman interaction, since $\tilde{\gamma}_\mu >> \tilde{\gamma}_N$). As a result,

$$\mathcal{Q} \approx \tilde{\gamma}_\mu B_{res}, \tag{4.4}$$

where B_{res} is the magnetic field where the level crossing occurs. Combining these two estimates, we obtain an approximate expression for B_{res}:

$$B_{res} = \left(\frac{\tilde{\gamma}_N}{\tilde{\gamma}_\mu}\right) B_{cr}. \tag{4.5}$$

Although somewhat crude, this equation can be used to narrow down an initial field region around which to scan. From Figure 4.2, we see that for GaAs, $B_{cr} \approx 2$ T. Assuming $\tilde{\gamma}_N \approx 10$ MHz/T, we see that $B_{res} \approx 200$ mT.

Armed with an estimate for the location of a LCR, a detailed search for resonances due to both Ga and As could begin. Spectra were collected for the magnetic field parallel to three crystal axes: $\langle 100 \rangle$, $\langle 110 \rangle$, and $\langle 111 \rangle$. Initially, experiments concentrated on searching for resonances with $\mathbf{B} \parallel \langle 100 \rangle$, since such data will allow the identification of the nearest neighbor host atoms. The procedure used to find these resonances is described in detail below:

1. Before searching for the main spectra, it is useful to first look near zero applied field. At these low fields, the muon polarization "decays" as it evolves in the randomly oriented magnetic dipole fields due to the surrounding nuclei. This leads to a $\bar{P}_z$ that looks like a giant resonance centered at $B = 0$ T (forming a so-called "zero crossing"). Figure 4.3 shows an example of such a crossing, with a scan range of 0–8 mT. The purpose of this scan is to aid in identification of the "real" resonances, located at larger fields which are much smaller. With the same experimental setup, all LCRs should have the same distinctive shape (in this case, the μLCR signal should go down and then up), regardless of their position. (The scan range is positive, so only half the resonance is visible). Knowing this can help to separate real signals from experimental noise.

2. With the estimate of B_{res} in mind, a scan was first performed over a field range of $B = 229.9 - 370.0$ mT, with $\mathbf{B} \parallel \langle 100 \rangle$. A possible resonance was observed, and the scan range was narrowed to $B = 283.0 - 325.8$ mT to try and resolve the signal in more detail. The data for this scan are shown in the inset of Figure 4.5(a). The data shown in the main part of the graph are from a later set of scans done to better establish the position of this resonance, since the field was not calibrated accurately in this initial data set. The location of this resonance is at 304.0 mT. At this point, there is no way to know whether this μLCR is due to one of the Ga isotopes or the As.

3. Arbitrarily, the resonance seen above was assigned to ^{71}Ga. From (3.8), we see that $Q^i \propto eq^i$, where eq^i is known for ^{71}Ga, ^{69}Ga, and ^{75}As (see Table 3.2). Since the position of each resonance depends on Q^i,

$$\frac{Q^{71}}{Q^{69}} = \frac{B^{71}_{res}}{B^{69}_{res}} = \frac{eq^{71}}{eq^{69}} \approx 0.629 \tag{4.6}$$

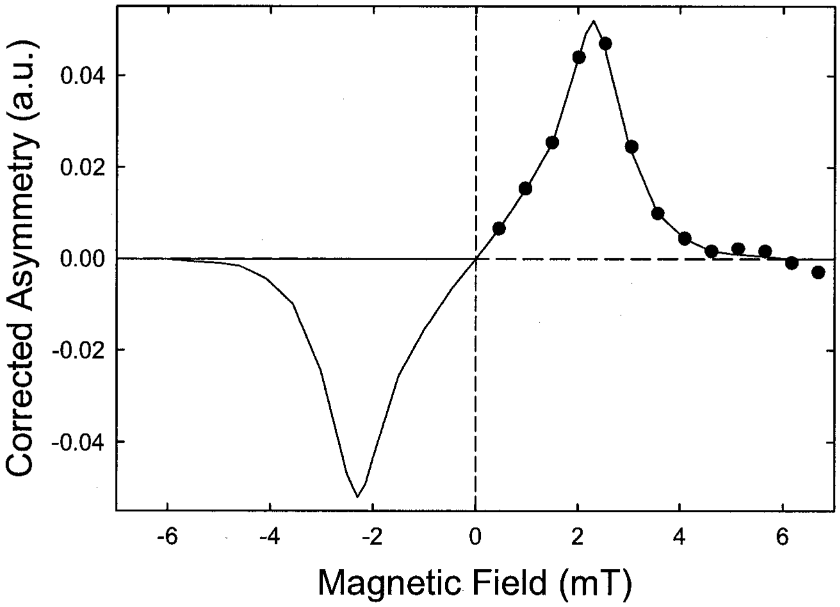

Figure 4.3: Zero crossing for GaAs:Zn with **B** || ⟨100⟩. Solid line is a guide to the eye.

The position of the Ga resonances should scale by this ratio. If the resonance at 304.0 mT was in fact due to ^{71}Ga, then there should be another resonance due to ^{69}Ga located near 483 mT. Two scans from 451.8–514.4 mT and 462.2–503.9 mT revealed no noticeable signature in this region. As a result, we can narrow down the candidates for the first resonance to ^{69}Ga or ^{75}As.

4. Next, it was assumed that the LCR at 304.0 mT was due to ^{69}Ga. A resonance due to the second isotope should therefore be located near 191 mT. Four scans were performed, encompassing a range of fields from 170.2 mT to 245.3 mT. A clear resonance was found at 192.0 mT, exactly where predicted [Figure 4.4(a)]. With some confidence, we can therefore assign the resonances at 192.0 mT and 304.0 mT to ^{71}Ga and ^{69}Ga respectively.

5. With both Ga resonances assigned, the only remaining signature is that due to As. Since ^{75}As is 100% abundant, it does not possess an isotopic signature. A number of scans were performed over a large range, from 503.7–754.4 mT. A large resonance was finally observed at 665.6 mT [Figure 4.6(a)]. Although these resonances are almost certainly due to As, a final check was done: assuming this LCR was in fact due to ^{71}Ga, a scan was done from 1034.2–1085.4 mT to search for the

Orientation	Resonance Position (mT)	Nucleus
⟨100⟩	192.0	^{71}Ga
⟨100⟩	304.0	^{69}Ga
⟨100⟩	665.6	^{75}As
	734.4 *	
⟨110⟩	315.6	^{69}Ga
⟨111⟩	210.6	^{71}Ga
	201.5 *	
	224.7 *	
⟨111⟩	701.5	^{75}As

Table 4.2: Summary of LCR locations for Mu$^+$ in p-type GaAs. Resonances marked with a * are smaller companions to the main lines which were within the experimental scan range. Positions are based on best fits to the experimental data discussed in the text.

accompanying ^{69}Ga resonance. As expected, there was no evidence of a line in this range.

With the ⟨100⟩ resonances successfully assigned, it is possible (with careful analysis) to find resonances along the other two orientations. Table 4.2 summarizes the position of the main ⟨100⟩ resonances discussed above, as well as LCRs for the other orientations. Data for ^{69}Ga with **B** ∥ ⟨110⟩ are shown in Figure 4.5(b). Data with **B** ∥ ⟨111⟩ are shown in Figure 4.4(b) and Figure 4.6(b) for ^{71}Ga and ^{75}As respectively. These LCRs, along with the companions resonances, will be required to establish the muon site and estimate the muon nuclear separation.

4.3 Analysis of Spectra

In this Section we discuss further analysis of the μLCR data. The ultimate goal will be to assign the muon to a site in the GaAs lattice. For the analysis, we will make two main assumptions:

1. Only nearest neighbor interactions are considered to be important. Since $\mathcal{D}^i \propto r^{-3}$, coupling between the muon and next nearest (and further) neighbors should lead to very small signals. (This will be justified *a posteriori* later in this section).

2. As discussed in Section 3.4.4, LCRs due to different atomic species do not affect each other and can therefore be fit independently. This is valid for weak interactions, which is certainly the case in GaAs.

Let us begin by examining the ⟨100⟩ resonances in more detail. Figures 4.4(a), 4.5(a), and 4.6(a) show the data along this orientation for ^{71}Ga, ^{69}Ga, and ^{75}As respectively. The presence of both Ga and As LCRs along this orientation is evidence that both nuclei are nearest neighbors to the muon. This result suggests that the interstitial tetrahedral T_{Ga} and T_{As} sites, which possess nearest neighbors of one species only, can be ruled out. However, we must determine the orientation of the nearest neighbors which respect to the muon in order to accurately assign the site.

The symmetry of the muon site can be determined by studying the shift in position of the LCRs when **B** is applied parallel to other crystallographics directions. Figure 4.5(b) shows data for ^{69}Ga with $\mathbf{B} \parallel \langle 110 \rangle$, and Figures 4.4(b) and 4.6(b) show data with $\mathbf{B} \parallel \langle 111 \rangle$ for ^{71}Ga and ^{75}As respectively. Clearly, there is a significant shift in the resonance positions as the magnetic field direction is altered. Comparison of the data with theoretical simulations of (3.9) indicates that both the Ga and As nuclei lie along a ⟨111⟩, i.e. bond, direction. The values of φ (i.e. the angle between **B** and the bond direction) are consistent with this conclusion. Specifically, the ⟨100⟩ spectra are due to $\varphi = 54.74°$, while the ⟨110⟩ and ⟨111⟩ data have contributions from $\varphi = 35.26°$, 90° and $\varphi = 0°, 70.53°$ respectively. Note that the μLCR spectra for all angles can be reproduced with single values of $\mathcal{Q}^{71} = 12.8875 \pm 0.0015$ MHz and $\mathcal{Q}^{75} = 44.970 \pm 0.004$ MHz. As a further consistency check of the symmetry, we note that the 734.4 mT ^{75}As companion line with $\mathbf{B} \parallel \langle 100 \rangle$ is reproduced for $\varphi = 54.74°$. As discussed in Chapter 3.4.4, the position of this line is very sensitive to the orientation of the magnetic field with respect to the bond axis.

The ⟨111⟩ symmetry of the nearest neighbors rules out the T sites as locations for the muon, leaving the BC and AB sites as possible candidates. The position and symmetry of the resonances is insufficient to rule either one out; we must therefore estimate the separation between the muon and nearest neighbors. The muon-nuclear separation can be estimated from the size of the LCRs. Specifically, the experimental data must be carefully fit to extract values for $\mathcal{D}^i$, from which r_i can be calculated using (3.8). Certain orientations are more appropriate for determining the dipole parameter than others. For example, consider the ^{71}Ga signal when $\mathbf{B} \parallel \langle 100 \rangle$ [see Figure 4.4(a)]. For any arbitrary orientation there are four nearest neighbor bonds, and hence four unique values of φ. If **B** is exactly parallel to ⟨100⟩, then all four bonds are at the same angle; i.e. $\varphi = 54.74°$. If the crystal was misaligned such that $\mathbf{B} \nparallel \langle 100 \rangle$, each of the four bonds would be at a

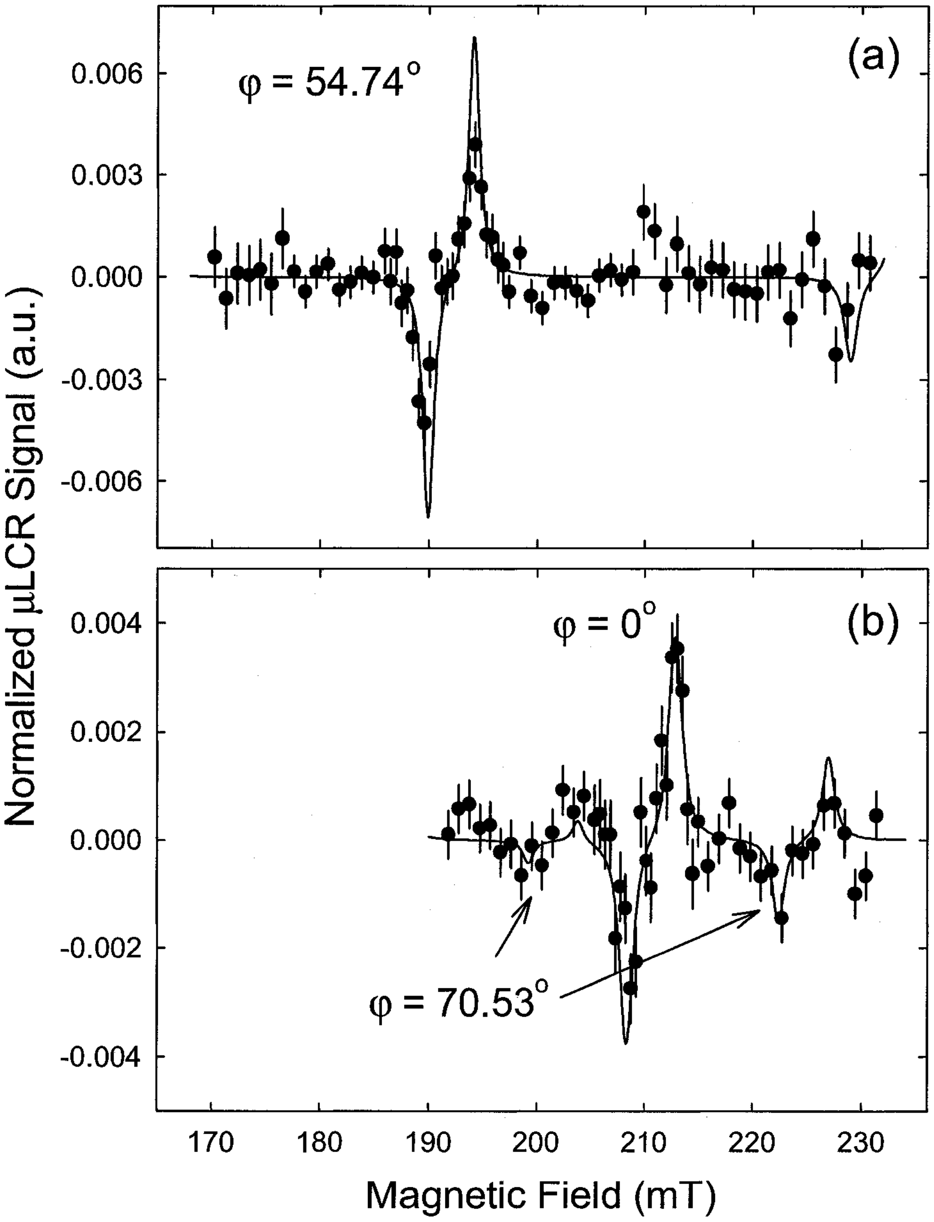

Figure 4.4: Experimental μLCR data for ^{71}Ga with (a) **B** $\parallel$ $\langle 100 \rangle$ ($\varphi = 54.74°$) and (b) **B** $\parallel$ $\langle 111 \rangle$ ($\varphi = 0°$, $\varphi = 70.53°$). Solid lines are simulations using best fit parameters described in text.

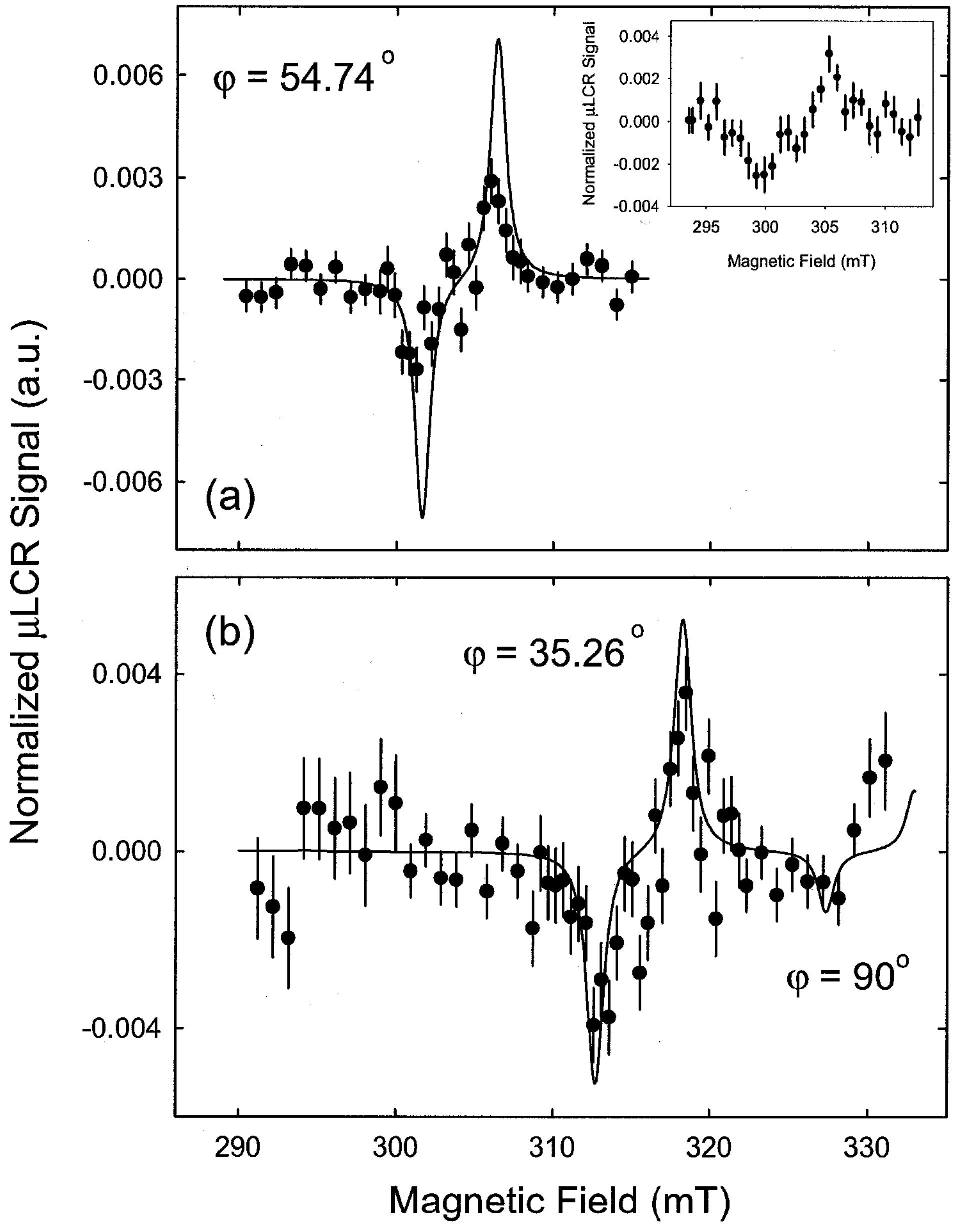

Figure 4.5: Experimental μLCR data for ^{69}Ga with (a) $\mathbf{B} \parallel \langle 100 \rangle$ ($\varphi = 54.74°$) and (b) $\mathbf{B} \parallel \langle 110 \rangle$ ($\varphi = 35.26°$, $\varphi = 90°$). Solid lines are simulations using best fit parameters described in text. Inset shows previously obtained ^{69}Ga data, where the field calibrations were not accurate.

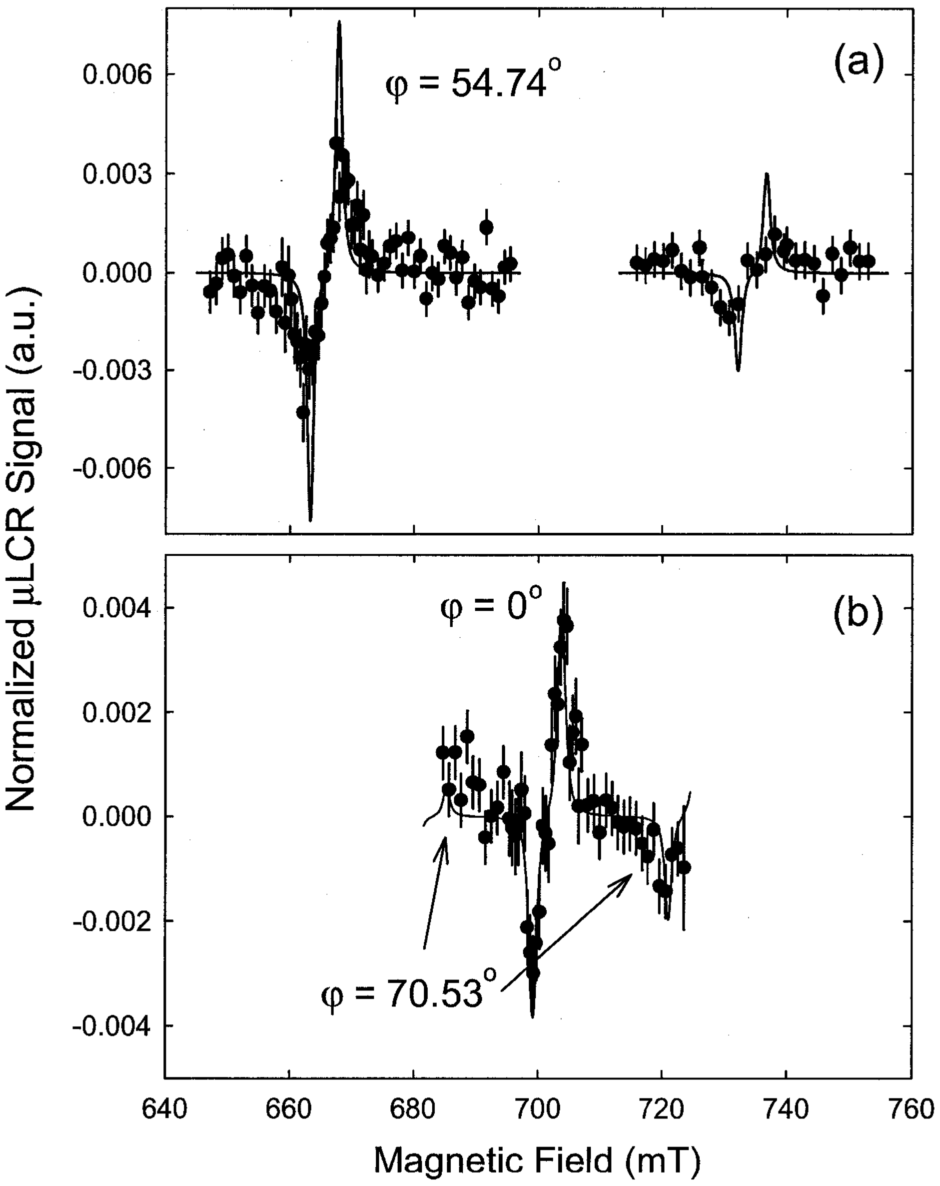

Figure 4.6: Experimental μLCR data for ^{75}As with (a) $\mathbf{B} \parallel \langle 100 \rangle$ ($\varphi = 54.74°$) and (b) $\mathbf{B} \parallel \langle 111 \rangle$ ($\varphi = 0°$, $\varphi = 70.53°$). Solid lines are simulations using best fit parameters described in text.

different angle, slightly different from 54.74°. The effect on the LCR is shown in Figure 4.7(b) (part (a) shows the graph of $\bar{P}_z$) for the ^{71}Ga resonance. The dotted and dashed lines correspond to the case where **B** was rotated 1° and 2° respectively. Rotations were done in three dimensions, around $\hat{z}$, $\hat{x}$, and $\hat{y}$ by the same angle (in that order). (As a result of this transformation, the angle between the "new" field and $\langle 100 \rangle$ was approximately 2°). As the misalignment increases, there are two key changes to the lineshape. First, the single peak becomes two distinct peaks. This is due to the fact that the rotation creates four unique angles, with two pairs almost identical (shown in Table 4.3). As a result, two resonances for $\theta \approx 53°$ and $\theta \approx 56°$ begin to appear. The second (and most important) change is the fact that the amplitude of the LCR decreases by approximately 50%. Note that the two distinct peaks seen in the simulations are likely unresolvable experimentally with the field step used in the scan. Analogous simulations are shown in Figure 4.8 for $\mathbf{B} \nparallel \langle 111 \rangle$. (Recall that for $\mathbf{B} \parallel \langle 111 \rangle$, there is one bond at $\varphi = 0°$ and three at $\varphi = 70.53°$). In this orientation, the influence of misalignment of the crystal is much weaker; this is clearly seen in part (b) of the figure. The large resonance at 210.6 mT (due to the single bond at 0° when **B** is perfectly parallel to $\langle 111 \rangle$) is not affected, whereas the satellite resonances (due to the remaining three bonds at 70.53°) exhibit the same splitting behavior and decreases in amplitude for small misorientations.

Since the main line ($\varphi = 0°$) along $\langle 111 \rangle$ is largely unaffected by small misorientations of the sample, data for the Ga and As lines for $\mathbf{B} \parallel \langle 111 \rangle$ was used for estimating the strength of the muon-Ga and muon-As dipole interactions. However, given the spread and statistical error in the data, it is still difficult to judge a "best fit". To obtain a reasonable estimate to the error, each LCR was fit three times. First, the data were fit as closely as possible to the simulation. Next, minimum and maximum values were obtained by varying the dipole parameter, until the fit was judged to be particularly poor. Although this is approximate, the values obtained should still give us a reasonable estimate for a range of $\mathcal{D}^i$ values. In this fashion, final values and errors for the dipole parameter were calculated using the following formulas:

$$\mathcal{D}^i = \frac{\mathcal{D}^i_{max} + \mathcal{D}^i_{min}}{2}; \qquad \delta\mathcal{D}^i = \frac{\mathcal{D}^i_{max} - \mathcal{D}^i_{min}}{2}. \tag{4.7}$$

Final numerical values are therefore $\mathcal{D}^{71} = 0.019 \pm 0.003$ MHz and $\mathcal{D}^{75} = 0.012 \pm 0.002$ MHz. The estimates for $\mathcal{D}^i$ obtained do not accurately reproduce the experimental amplitudes for the $\langle 100 \rangle$ and $\langle 110 \rangle$ spectra; this discrepancy is attributed to misorientation of the crystal as described previously.

Orientation	Rotation Angle (Degrees)	Bond Angle(s) (Degrees)
⟨100⟩	0	54.74 (×4)
	1	53.3217 53.3468 56.1496 56.1738
	2	51.9092 52.0115 57.5621 57.6575
⟨111⟩	0	0 70.53 (×3)
	1	1.41412 69.8080 69.8450 71.9427
	2	2.82771 69.0604 69.2089 73.3552

Table 4.3: Angles between nearest neighbor bonds and the magnetic field after rotating the crystal. The magnetic field is rotated around all three axes (x, y, z) by the rotation angle.

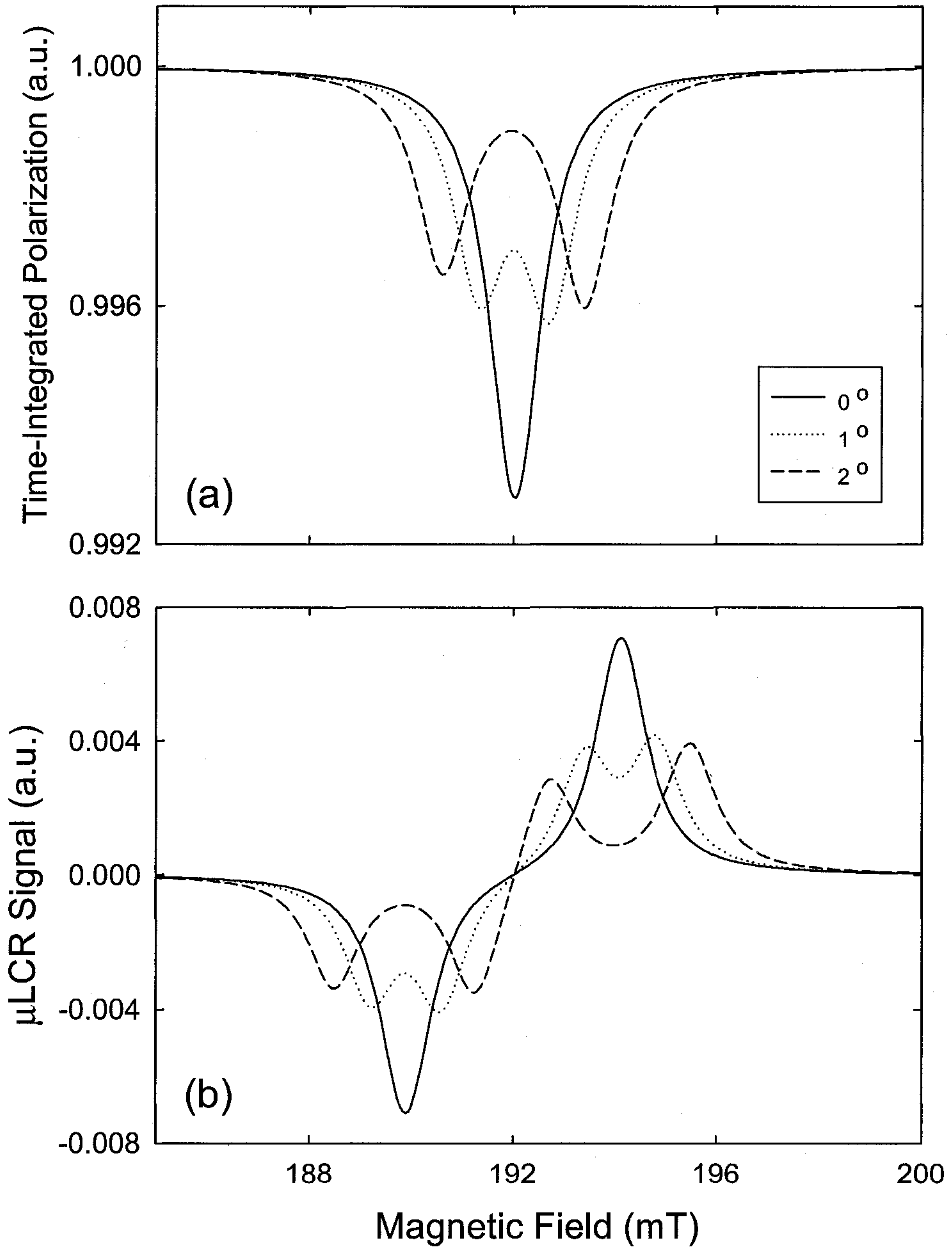

Figure 4.7: Simulations showing effect of tilting **B** with respect to $\langle 100 \rangle$ on the (a) time-integrated polarization, and (b) μLCR signal.

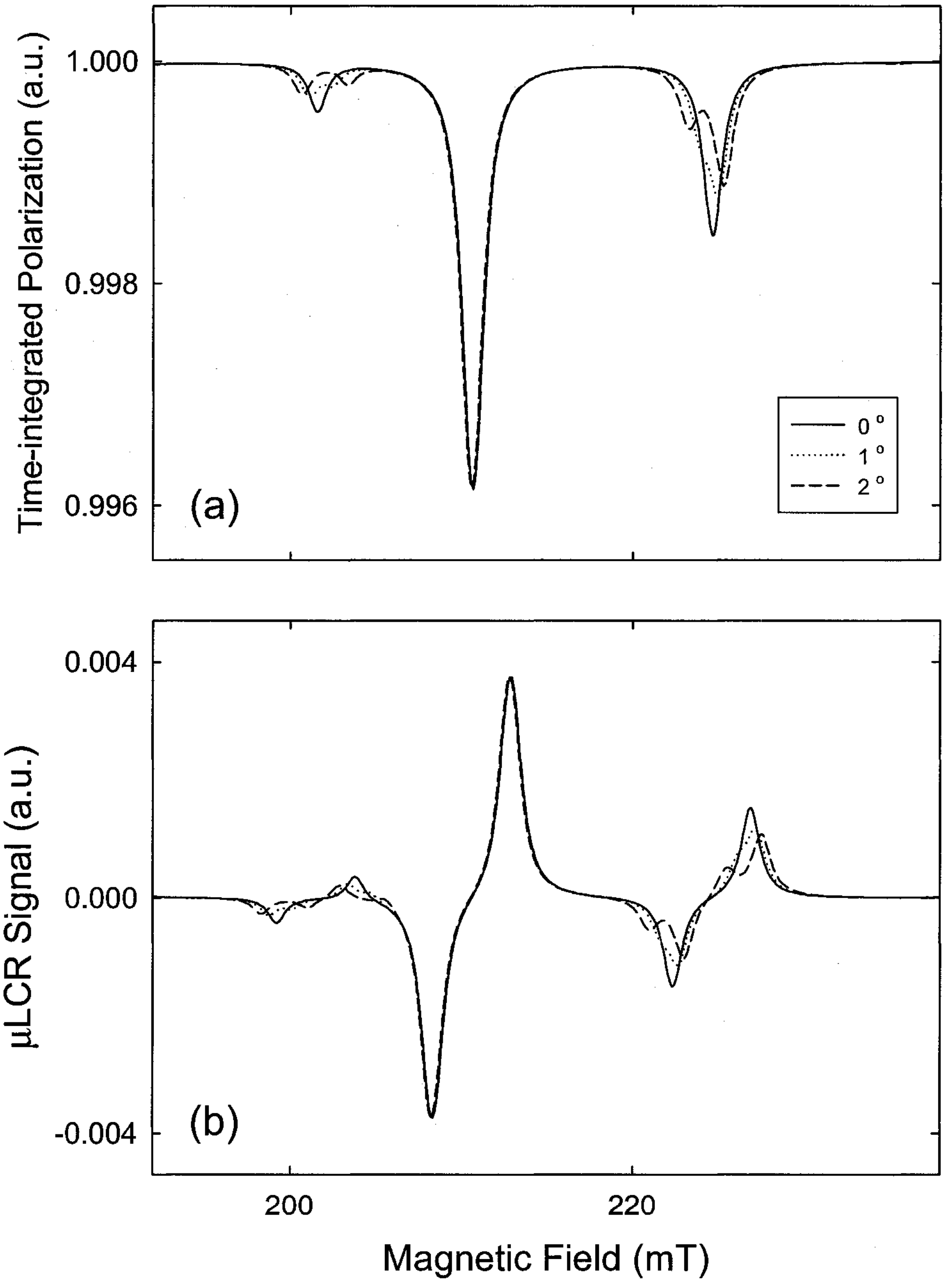

Figure 4.8: Simulations showing effect of tilting **B** with respect to ⟨111⟩ on the (a) time-integrated polarization, and (b) μLCR signal.

Using (3.8), we can now estimate the muon-nuclear separation. Solving for r_i,

$$r_i = \left(\frac{\mu_0 h\tilde{\gamma}_\mu \tilde{\gamma}_N}{4\pi \mathcal{D}^i}\right)^{1/3} \quad ; \quad \delta r_i = \frac{1}{3}\left(\frac{\mu_0 h\tilde{\gamma}_\mu \tilde{\gamma}_N}{4\pi}\right)^{1/3} \frac{\delta \mathcal{D}^i}{(\mathcal{D}^i)^{4/3}}, \tag{4.8}$$

where δr_i was calculated using standard error propagation. Substituting our final values for the dipole parameter, we get

$$\begin{aligned} r_{Ga} &= 1.83 \pm 0.10 \text{ Å} \\ r_{As} &= 1.76 \pm 0.10 \text{ Å} \end{aligned} \tag{4.9}$$

The similarity between the values of r_{Ga} and r_{As} rule out the AB site as a possible location; the data therefore suggest that the muon is located at the BC site. These values for the nearest neighbor separation lead to an estimated Ga–As bond length of 3.59 ± 0.20 Å, a stretch of $\approx 47\%$ over the undistorted length of 2.45 Å at 50 K [30].

In order to confirm that the observed LCRs are due to the nearest neighbors to the muon, we measured $P_z(t)$ in the absence of an external magnetic field. In ZF, the muon polarization evolves under the influence of the dipole interaction; the strength of the interaction will determine how quickly the signal decays (see Section 3.2). Figure 4.9 shows experimental data for $T = 50$ K and $\varphi = 54.74°$. The solid lines are simulations done using (3.9); the top and bottom lines correspond to $\mathcal{D}^i_{min}$ and $\mathcal{D}^i_{max}$ respectively. Clearly, the experimental data agree very well with the possible range of values obtained from the fits. As a result, we can conclude that the resonances found are the primary ones, i.e. there are no large resonances outside the scan range. The data fall closer to the line corresponding to $\mathcal{D}^i_{max}$, indicating that if anything our estimates for $\mathcal{D}^i$ are on the conservative side. This deviation could be due to the effect of next (and further) nearest neighbor nuclei.

Nucleus	$\mathcal{Q}^i$ (MHz)	$\mathcal{D}^i$ (MHz)
^{71}Ga	12.8875 ± 0.0015	0.019 ± 0.003
^{69}Ga	20.482 ± 0.002	0.015 ± 0.002
^{75}As	44.970 ± 0.004	0.012 ± 0.002

Table 4.4: Summary of $\mathcal{Q}^i$ and $\mathcal{D}^i$ values obtained from fits to the experimental data. Values for ^{69}Ga were calculated using $\mathcal{Q}^{69} = (eq^{69}/eq^{71})\mathcal{Q}^{71}$ and $\mathcal{D}^{69} = (\tilde{\gamma}_N^{69}/\tilde{\gamma}_N^{71})\mathcal{D}^{71}$. Errors are statistical.

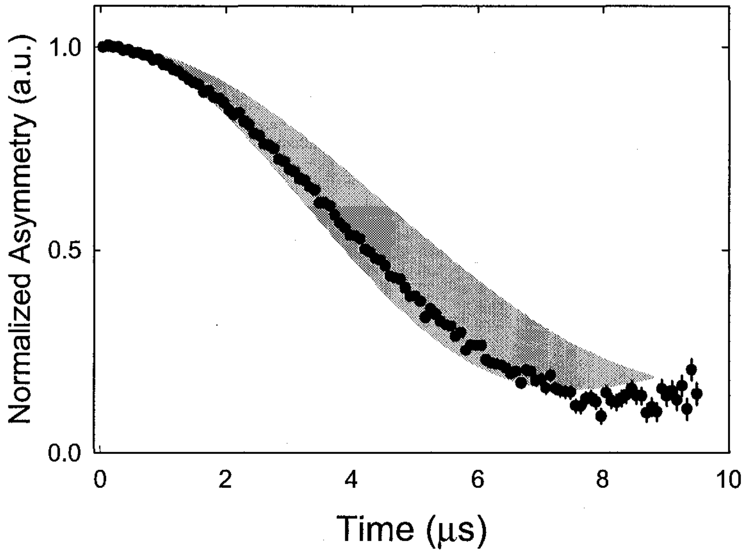

Figure 4.9: Time dependence of zero-field muon polarization for $T = 50$ K and $\varphi = 54.74°$. Shaded area represents uncertainty in the $\mathcal{D}^i$ values obtained from the fits (see text).

Our experimental results for r_i can be compared to theoretical calculations for H^+. Pavesi *et al.* [13] performed first-principles total energy calculations using a 32-atom supercell, in the low-density approximation. Their results indicate that when the lattice is allowed to relax, H^+ is most likely to be located in regions of high valence charge, such as the BC site; this is the lowest energy configuration of the available sites in the lattice. This will result in a large relaxation of the Ga–As bond. The separations between the muon and the Ga and As are found to be 1.80 Å and 1.52 Å respectively (resulting in a bond length of 3.32 Å). (The muon binds preferentially to the As due to its higher electronegativity). Breuer *et al.* [31] used density functional calculations with an 87-atom cluster to investigate the stable sites of interstitial H. Once again, the BC site was found to be the lowest energy configuration, with Ga and As separations of 2.14 Å and 1.50 Å respectively (resulting in a bond length of 3.64 Å). In comparison to our experimental measurements, there are a few points to note:

- The LCRs place μ^+ at the BC site, consistent with the theoretical position of H^+.
- Our estimate for r_{Ga} agrees very well with Pavesi's result, but is significantly smaller than that predicted by Breuer.

- Both theoretical results for r_{As} are comparable, but significantly smaller than our experimental value.

The discrepancy in the μ^+–As separation is interesting. Our results indicate that the muon is much closer to the geometrical bond center, with almost equal spacing from the Ga and As. One possible explanation is that the larger zero point energy of the muon, combined with an anharmonic potential along the bond, could cause the muon to be closer to the bond center on average. More detailed theoretical calculations could help to shed some light on this.

Chapter 5

Electric Field Enhanced Diamagnetic Muonium in SI-GaAs

In this Chapter we discuss the formation of diamagnetic muonium (i.e. Mu^+ and Mu^-) in SI-GaAs, in the presence of an electric field. At low temperatures, only Mu^0 will form in high-resistivity GaAs [32]. By applying an electric field across the sample, we can increase the diamagnetic single at the expense of the neutral centers. Relatively little is known about the formation processes which occur between implantation of the bare muon and the subsequent decay of the final charge state, due to the very short timescales over which they occur (on the order of nanoseconds). By studying both the transverse field muon precession and level crossing resonances in the presence of an electric field, we can determine which charge state is forming, and possibly gain insight into the formation process itself. As well, this information may make it possible to control whether Mu^+ or Mu^- is forming.

Section 5.1 discusses details of the experiments used to collect the data. A description of the fitting and analysis of TF data will follow in Section 5.2. Analysis and discussion of the EF enhanced data is presented in Section 5.3, including a brief discussion of muonium formation.

5.1 Experimental

EF-μSR experiments were conducted using both TF and μLCR configurations. The μLCR experiments were performed in exactly the same way as discussed in the previous

Sample #	Company	Orientation	Approx. Size $l \times w \times t$ (mm)
GaAs–s1	AXT	$\langle 100 \rangle$	$20 \times 23 \times 0.35$
GaAs–s2	AXT	$\langle 100 \rangle$	$25 \times 25 \times 0.35$
GaAs–s3	AXT	$\langle 100 \rangle$	$25 \times 25 \times 0.35$

Table 5.1: SI-GaAs samples used for the EF-μSR experiments.

chapter, except for the presence of an electric field. The TF experiments were standard TD, with four counters used for data collection (see Figure 2.2). The muon was spin rotated before entering the sample, so that the spin was perpendicular to the applied magnetic field. For all TF data, the magnetic field strength was 1 Tesla (the reason for which will be discussed shortly).

Electric fields ranging from $0 - 20$ kV/cm were applied across the samples using a switching power supply. Silver with a thickness of ≈ 1 μm was deposited onto both sides of the GaAs samples to act as electrodes, essentially forming a parallel plate capacitor. Wires were then soldered onto the Ag plates, allowing a uniform EF to be applied across the sample. In order to prevent charge accumulation on the surface of the sample which could produce an undesirable screening effect, the EF was switched periodically between pointing parallel and antiparallel to the incoming muon momentum [19]. The switching rate was 10 Hz, which is high enough to saturate the diamagnetic signal in SI-GaAs. Data for each field direction are routed to a separate set of histograms and analysed independently.

The same spectrometers, cryostats, etc. discussed in Chapter 4 were utilized in the TF-μSR experiments. The SI-GaAs samples used are shown in Table 5.1.

5.2 Fitting of Transverse Field Data

Transverse field data are of the form shown in Figure 2.3(b); that is, a time-dependent damped oscillation. There are four parameters of interest which can be extracted from such a signal: the asymmetry (amplitude) A, relaxation rate σ, precession frequency ω_μ, and phase ϕ. The fitting of the TF data in this thesis was done using a program called MSRFIT, which utilizes the functional minimization program MINUIT [33] to analyse time-differential data; MINUIT in turn minimizes the weighted least squares function.

(All errors quoted for fit parameters in this chapter are direct statistical errors taken from the fitting). The program accepts initial guesses for the above parameters, and fits an arbitrary signal function input by the user. The signal function can be in the form of a single term, or the sum of multiple signals. The form of the function also depends on the configuration of the experiment; i.e. whether it is TF, LF, or ZF. In this section, we will discuss the fitting procedure for TF-μSR data.

Consider a TF experimental setup with the magnetic field applied along $\hat{z}$, parallel to the incoming muon momentum. After spin rotation, the muon spin will be polarized along $\hat{x}$. We will consider the component of the polarization along $\hat{y}$. From Eq. (3.24), the polarization will be of the form

$$P_y(t) \propto \cos \omega_\mu t \tag{5.1}$$

For an isolated muon, this would be exact. However, as discussed in Section 3.5, the presence of random dipolar fields due to nuclear spins will cause the muon signal to undergo depolarization. As a result, the free precession described by (5.1) will be damped in some fashion. The polarization thus has the form

$$P_y(t) = AD(t) \cos(\omega_\mu t + \phi) \tag{5.2}$$

where $D(t)$ is a time-dependent damping factor. The exact form of $D(t)$ depends on the properties of the physical system; for a random distribution of static nuclear dipoles (such as in GaAs), the damping can be well described phenomenologically [8] by a Gaussian:

$$D(t) = \exp\left(-\sigma^2 t^2\right) \tag{5.3}$$

The relaxation (or depolarization) rate σ, i.e. the amount of damping, depends on both dipole and quadrupole interactions between the muon and surrounding nuclei.

For samples GaAs–s2 and GaAs–s3, a single oscillating term [like in (5.2)] describes the data well and enables us to reliably extract the relaxation rate. Both samples were large, resulting in a small background asymmetry of ≈ 0.002. (The background signal corresponds to muons which miss the sample, stopping elsewhere). However, sample GaAs–s1 was quite a bit smaller, with a background asymmetry almost four times larger. In order to account for a large background, we must modify the fitting function to accommodate a second signal. This is equivalent to adding two signals together: one from the sample of interest (i.e. the GaAs) and one from the background (due mostly to a diamagnetic signal from the Cu sample holder). In other words,

$$\begin{aligned} P_y(t) = & A_{GaAs} \exp\left(\sigma_{GaAs}^2 t^2\right) \cos\left(\omega_\mu^{GaAs} t + \phi_{GaAs}\right) \\ & + A_{Cu} \exp\left(\sigma_{Cu}^2 t^2\right) \cos\left(\omega_\mu^{Cu} t + \phi_{Cu}\right) \end{aligned} \tag{5.4}$$

The asymmetry and relaxation of the background signal (A_{Cu}, σ_{Cu}) are assumed to remain constant with electric field. These are then estimated from fitting a run with $E = 0$ where there should be no diamagnetic contribution from the GaAs, and then fixed in all subsequent fits to the $E \neq 0$ data. As well, we assume that the frequency and phase of the background is the same as that in the GaAs. With the Cu signal fixed, MSRFIT is used to fit the sum of both signals, allowing one to extract fit parameters for the GaAs. (In addition, "high" TF data is usually transformed to the rotating reference frame (see Appendix A) for more efficient display and fitting).

Once the raw data have been fit, we must normalize it with respect to the maximum possible diamagnetic asymmetry; this gives us the so-called "diamagnetic fraction", which tells us the fraction of implanted muons that end up as Mu^+ or Mu^-. To get the maximum asymmetry, we collect data from a sample of Ag under identical experimental conditions. Due primarily to electron screening effects in the metal, only Mu^+ will form in Ag; as well, the diamagnetic signal experiences a very small relaxation. The silver sample is therefore used to measure the spread of the magnetic field through the sample. (This is assumed to be the same for the GaAs samples, which are essentially the same size and located in the same position). This spread in fields will lead to a relaxation, which must be taken into account. The corrected values for asymmetry and relaxation are therefore given by

$$A_{corr} = \frac{A_{raw}}{A_{Ag}}; \qquad \sigma_{corr}^2 = \sigma_{raw}^2 - \sigma_{Ag}^2 \tag{5.5}$$

5.3 Results and Discussion

Before discussing the current experimental data, it is useful to examine the behavior of the relaxation of the different diamagnetic states as a function of magnetic field from previous measurements. Figure 5.1 shows a reproduction of Hartmann curves for Mu^+ [15] and Mu^- [16], with $\mathbf{B} \parallel \langle 100 \rangle$. For low magnetic fields (< 100 mT), the relaxation rates have (coincidentally) almost identical values of $\approx 0.12\ \mu\mathrm{s}^{-1}$. As the field is increased, the value for Mu^+ remains the same, but the value for Mu^- begins to decrease rapidly. At $B = 1$ T (indicated by the dashed line), σ for Mu^- is approximately 0.06 $\mu\mathrm{s}^{-1}$, almost half the value for the positive center. This is the field at which the TF data

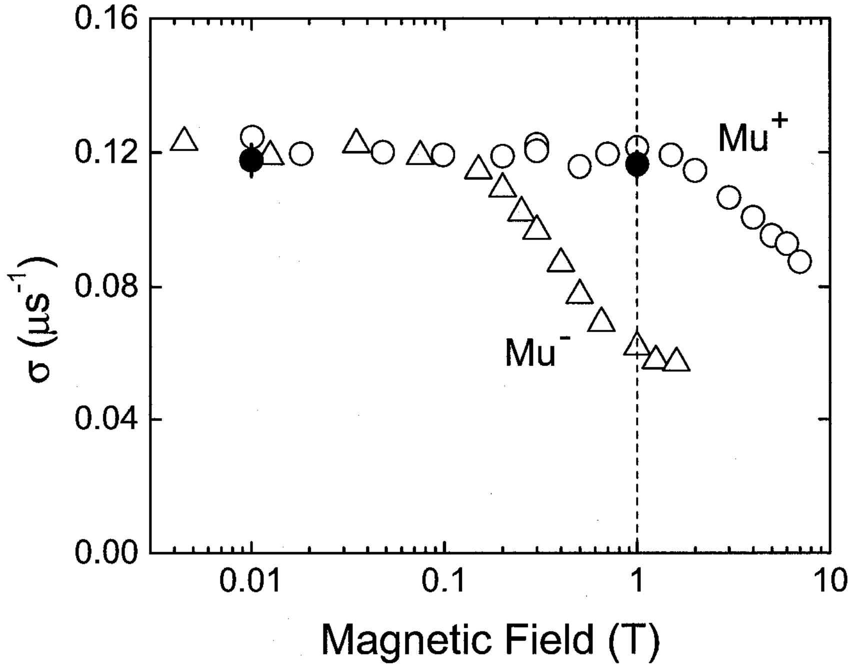

Figure 5.1: Relaxation of the transverse field signal at various magnetic fields. The hollow circles and triangles correspond to σ values for Mu$^+$ [15] and Mu$^-$ [16] respectively. The filled circles are experimental values collected with $E = 14.3$ kV/cm. The vertical dashed line is located at $B = 1$ T, where the transverse field data in this thesis were collected.

in this thesis were taken; by comparing the relaxation of the data taken at each electric field to the known values at 1 Tesla, we can identify which diamagnetic center is present at that particular EF.

A typical graph of the diamagnetic fraction as a function of electric field is shown in Figure 5.2(a). There is a very small asymmetry at $E = 0$, which increases asymmetrically about zero field as the magnitude of the field is increased. The reason for this asymmetric behavior is not completely understood. It is possibly (at least in part) due to the forces acting on the electrons with respect to the muon; when the electric field is applied parallel to the incoming muon momentum (i.e. $E > 0$), electrons will tend to be pushed away from the muon. This will result in an increased diamagnetic asymmetry at any particular electric field, which is consistent with the behavior in Figure 5.2(a).

Figure 5.2(b) shows a graph of σ for all three samples as a function of electric field. The convention used for the electric field direction is that $E > 0$ corresponds to the field parallel to the incoming muon momentum, while $E < 0$ corresponds to the field

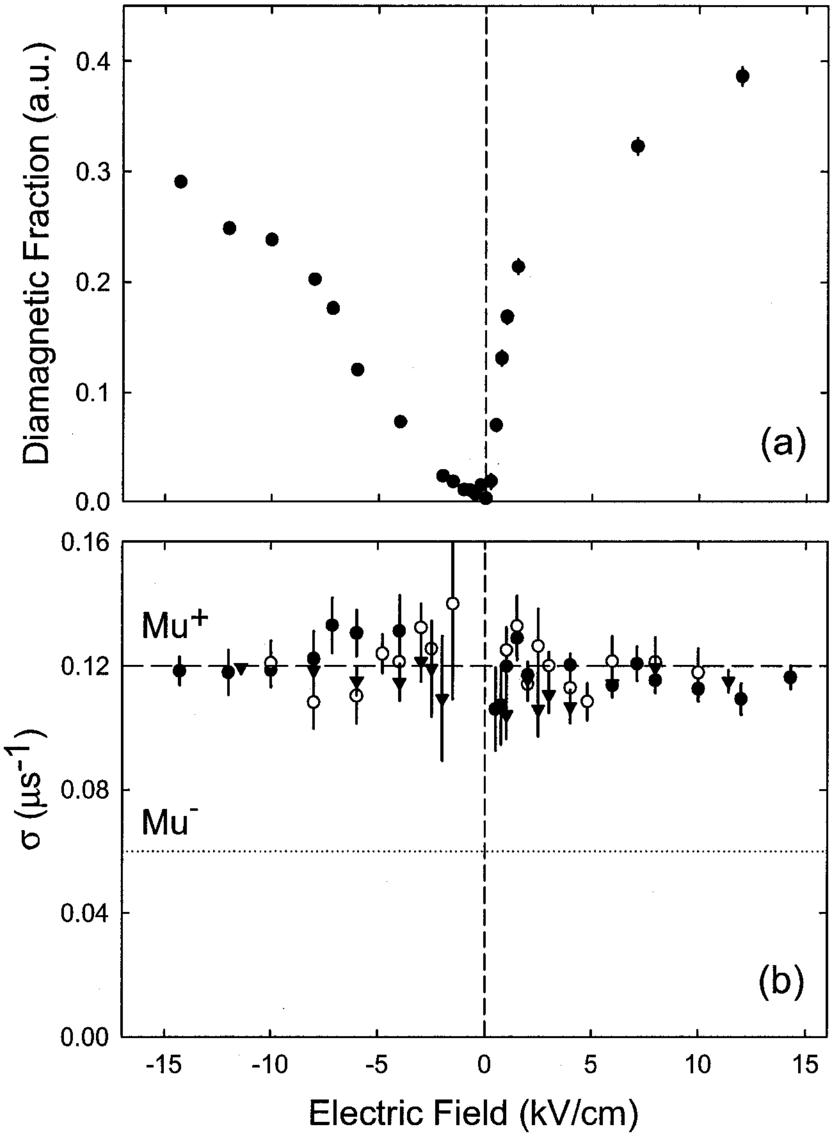

Figure 5.2: (a) Electric field dependence of the fraction of implanted muons that end up in the diamagnetic (Mu^+) state (sample GaAs–s3). $E > 0$ corresponds to the field direction applied parallel to the incoming muon momentum. (b) Relaxation of the transverse field diamagnetic signal at various electric fields. The different symbols correspond to the three samples studied. The dashed and dotted lines indicate the known experimental σ values for Mu^+ and Mu^- respectively.

opposite to the incoming muon momentum. Clearly, the data from all three samples are consistent with the value of σ due to Mu^+ (dashed line). The lack of data points for low fields (approximately < 1 kV/cm) is due to the fact that the Mu^+ fraction is very small, resulting in a weak signal and making it very difficult to extract statistically reliable fits for the relaxation rate. Therefore, in this region the experimental data do not explicitly rule out the formation of Mu^- (dotted line). However, the data for all other fields ($E > 1$ kV/cm) strongly indicate that Mu^+ is the observed state.

In addition to studying the behavior of σ as a function of electric field, μLCR experiments were also performed in the presence of an electric field to further confirm the identity of the charge state. Figure 5.3 shows the μLCR signal in SI-GaAs at $T = 10$ K, with $\mathbf{B} \parallel \langle 100 \rangle$ and $E = 20$ kV/cm. The data have been normalized to the diamagnetic asymmetry of a TF run taken at a low magnetic field ($B \approx 5$ mT) and at the same value of E. The top and bottom graphs correspond to $\mathbf{E}$ opposite and parallel to the incoming muon momentum respectively. The dashed line indicates the position of the μ^+–^{71}Ga resonance discussed in the previous chapter [Figure 4.4(a)]. The position of the LCR at 20 kV/cm is identical to that found in the heavily-doped GaAs sample. As well, the amplitude can be compared to the size of the signal seen in the p-type sample (≈ 0.0035). Within error, all of the diamagnetic fraction is accounted for in both EF directions. Therefore, the EF-μLCR data demonstrate that the electric field enhanced diamagnetic state at this electric field is in fact Mu^+. Note that μLCR data were only collected for this value of E; the time-consuming nature of level crossing experiments prohibited the taking of any further data, particularly at low electric fields where the fraction is very small. Therefore, both the TF-μSR and μLCR measurements at 10 K indicate that the application of an electric field leads to an enhanced signal for isolated Mu^+. This is true for electric fields in the range $\approx 1 - 15$ kV/cm (and in the case of μLCR, at 20 kV/cm as well) for either direction. This rules out any model in which the electric field leads to formation of Mu^-, at least at 10 K. (These results have been published in [34]).

In order to consider the formation of Mu^0 and Mu^+ in the context of our data, it is illustrative to first discuss what happens to the energetic muon ($E_\mu \approx 4$ MeV) after implantation [7, 8]. Immediately after entering the sample, the muon begins to give up energy to the lattice through inelastic scattering. Energy is lost to the lattice through a number of excitations, including the formation of electron-hole pairs (forming the so-called radiation track), slowing the muon down in the process. Once the muon has given up most of its energy and comes to a "stop", it is said to have "thermalized". (The center that has formed at this stage will be referred to as the initial state). After

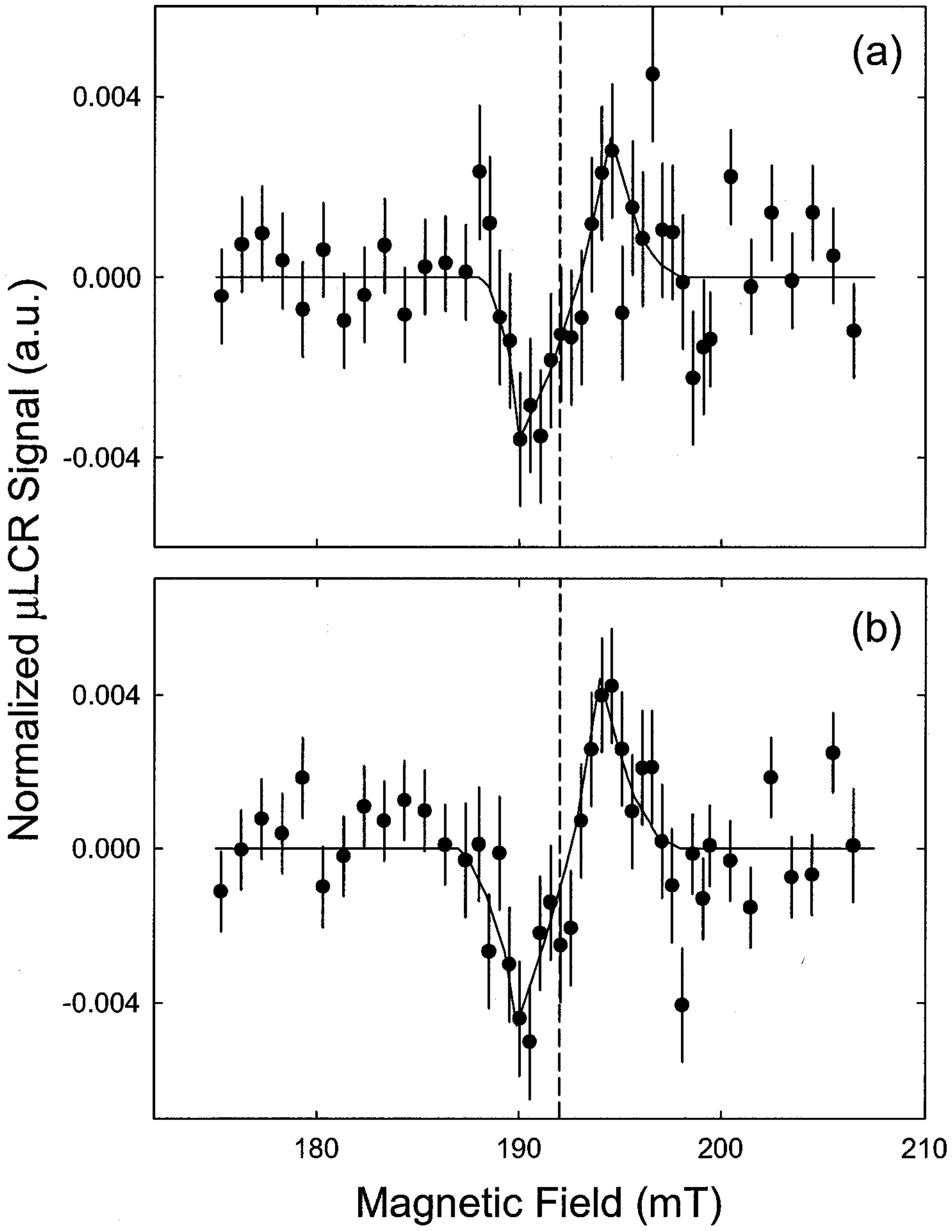

Figure 5.3: μLCR spectra for SI-GaAs with **B** $\parallel$ $\langle 100 \rangle$ and $E = 20$ kV/cm. (a) μLCR data for **E** opposite to incoming muon momentum. (b) μLCR data for **E** parallel to incoming muon momentum. In (a) and (b) the solid line is a guide to the eye. The vertical dashed line indicates the position of the μ^+–^{71}Ga resonance at 192.0 mT discussed in Chapter 4.

thermalization, the muonium can undergo some process (such as charge capture or loss) to form the center that is eventually detected; this will be referred to as the final state. In semiconductors, this entire process, from implantation to formation of the final state, happens extremely quickly compared to the window of muon decay ($\approx 10\ \mu$s).

The above process through which muonium forms can be classified into two main types: epithermal (i.e. prompt) formation, and delayed muonium formation (DMF) [35]. Epithermal formation occurs when the muon captures an electron from the radiation track sometime during the slow down phase, thermalizing as Mu^0. There are at least two mechanisms whereby it can become Mu^+: (1) through direct field-ionization, and (2) via capture of a thermalized hole from the radiation track:

$$\text{Mu}^0 + h^+ \rightarrow \text{Mu}^+ \tag{5.6}$$

The former can be ruled out by considering the magnitude of the EF necessary to ionize the center. Assuming the electron is in the ground state, the electric field necessary to overcome the Coulomb attraction to the muon is approximately

$$E = \frac{q_\mu}{4\pi\epsilon_0 a_0^2} \approx 5 \times 10^6\ \text{kV/cm} \tag{5.7}$$

where q_μ is the muon charge and a_0 is the Bohr radius. Therefore, the electric fields applied in this experiment are far too small to field ionize Mu^0. As a result we would not see any change in the diamagnetic fraction as the magnitude of the field was varied; Figure 5.2(a) clearly shows that this is not the case. The second mechanism, capture of a hole, can also be ruled out by looking at the phase of the diamagnetic precession signal for various electric fields. This is shown in Figure 5.4. If (5.6) happened "slowly", we would expect to see a different precession signal due to Mu^0 (either faster or slower than 135.54 MHz, depending on which neutral center was being observed), preceding that due to Mu^+ after capture of the hole. As a consequence, we would anticipate a change in phase as the electric field was varied. However, the data in Figure 5.4 indicate that ϕ is constant for all electric fields (except possibly for very low magnitudes, where the large statistical error once again makes it difficult to interpret the results). Therefore, we can rule out epithermal formation of Mu^0. Note that if (5.6) happened very quickly, then any phase difference would likely be negligible; as a result, we cannot explicitly rule out this possibility. Nonetheless, the data strongly indicate that Mu^+ is the initial state, as well as the final one.

Although epithermal formation is unlikely based on the experimental results, our data support a proposed DMF model [18, 36] whereby Mu^0 forms due to capture of an

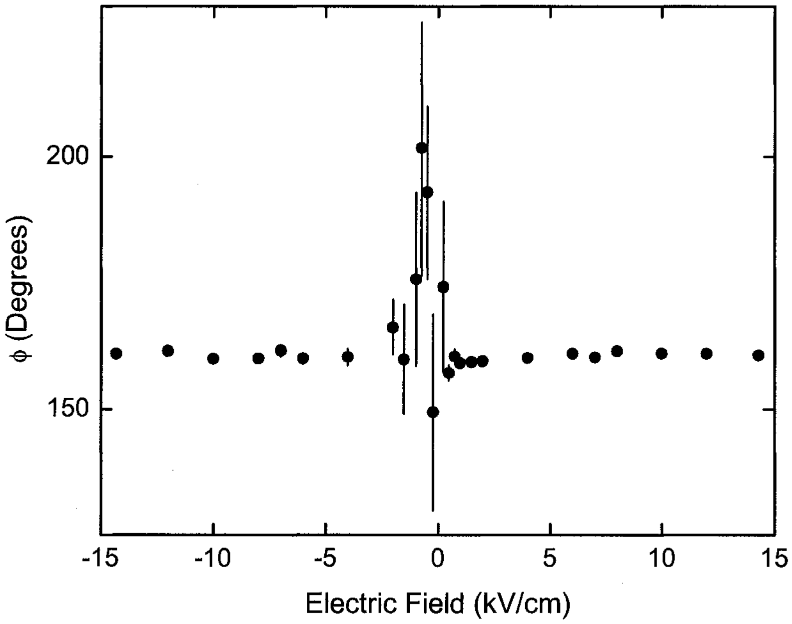

Figure 5.4: Phase of the diamagnetic signal for various electric fields.

electron from the radiation track into an *excited* state. In the absence of an electric field, the electron would likely decay into the ground state, to form Mu^0. The role of the electric field would thus be to field ionize the excited center before the electron has a chance to decay. (The magnitude of the fields applied in our experiments are consistent with the electric field required to ionize an excited center). Thus, the electric field would prohibit the formation of the neutral center, while enhancing the precession signal due to Mu^+.

Chapter 6

ZeroX: An Improved Technique for Studying Low-Spin Systems

ZeroX is a new μSR technique which was conceived to study diamagnetic centers in low-spin semiconductors (i.e. those that contain very few nuclear spins with $J > 0$). Conventional μSR techniques can be limited in these cases, since the muon spin only interacts with nuclei with non-zero spin. For example, in a material such as Si where only 5% of the nuclei have non-zero spin ($J = 1/2$), this results in a weak signal since only a small fraction of the implanted muons interact with a non-zero spin. In this Chapter the basics of the ZeroX technique will be discussed, including specifics of the experimental setup. Preliminary data collected in p-type GaAs and p-type Si will be discussed. Since much of the analysis is still ongoing, the discussion will remain qualitative.

Sample	Company	Orientation	Dopant Concentration (cm^{-3})	Size $l \times w \times t$ (mm)
GaAs–z1	CSI	$\langle 100 \rangle$	$1.9 - 4.1 \times 10^{19}$	$30 \times 30 \times 0.3$
GaAs–z2	CSI	$\langle 100 \rangle$	$1.84 - 4.37 \times 10^{19}$	$25 \times 25 \times 0.3$
Si–z1	SFJC	$\langle 100 \rangle$	10^{18}	$30 \times 30 \times 0.63$

Table 6.1: p-type GaAs:Zn and Si:B samples studied using the ZeroX technique.

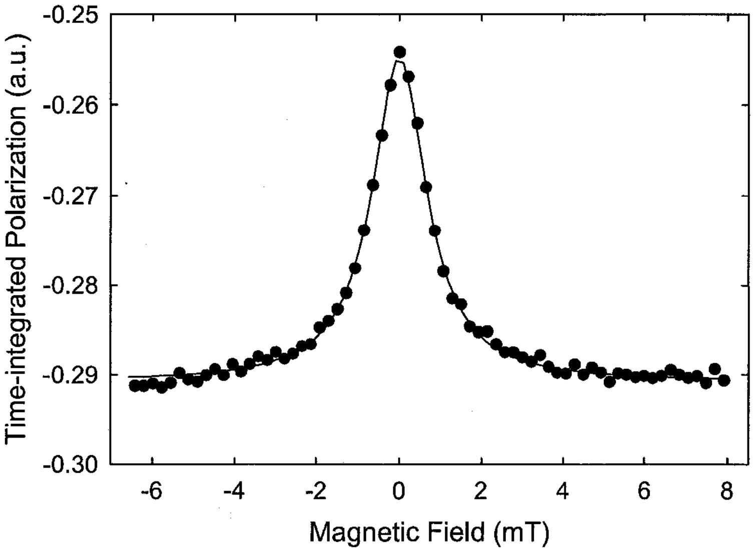

Figure 6.1: Typical ZeroX spectrum for a sample of p-type GaAs:Zn at 50 K. Solid line is a fit to a Lorentzian (discussed in text).

6.1 Discussion of Technique

ZeroX is a time-integral technique which utilizes a LF counter arrangement. The increased muon rate that TI experiments allow is what makes ZeroX more sensitive than conventional techniques, such as TD-LF experiments. In addition, there are two key differences which differentiate the ZeroX technique from a conventional LF-μSR experiment:

1. Instead of fixing the magnetic field along a particular direction (either parallel or antiparallel to the incoming muon momentum) such that $B > 0$, both positive and negative fields are used, with the field scans centered around $B = 0$.
2. The applied field is weak, with a magnitude on the order of a few milli-Tesla.

An example of ZeroX data is shown in Figure 6.1. The y-axis is graphed as $1 - \bar{P}_z$, so the polarization appears as a peak rather then a dip. The data are often fit to a Lorentzian lineshape of the form

$$L(B) = A\frac{w^2}{B^2 + w^2} + b \tag{6.1}$$

where A is the amplitude, w is the half-width half-max, and b is the background. The magnetic field is sometimes replaced by $B - B_0$ to account for any shifting about

$B = 0$. The amplitude represents the maximum amount of polarization lost due to dipole coupling at zero field. Note that magnetic fields of ≈ 10 mT are sufficient to completely quench the dipole interaction (i.e. the applied field along $\hat{z}$ is much stronger than the dipole fields).

The same spectrometers and other equipment (such as cryostats and sample holders) used in the μLCR and EF experiments are also used for ZeroX as necessary. However, a power supply capable of switching the direction of the current (field) is required.

The samples used in these preliminary ZeroX experiments are listed in Table 6.1. The GaAs and Si samples were doped with Zn and B respectively, making both samples p-type.

6.2 p-type GaAs Measurements

The data and analysis presented in the previous two chapters were possible due to the fact that all of the nuclei in GaAs are spin 3/2, and thus have abundant dipole and quadrupole interactions. Therefore, a highly sensitive method like ZeroX is not really required to study GaAs. However, it does provide a method to test the feasibility of the technique, since results on GaAs obtained using ZeroX should agree with those done using more conventional methods (such as TF-μSR).

Figure 6.2 shows a comparison of ZeroX (empty circles) and ZF (filled circles) data taken on samples of GaAs:Zn. The ZF data show the temperature dependence of the relaxation rate Δ [15] in zero applied magnetic field[1]; the ZeroX data show the fitted Lorentzian amplitude. The behavior of both sets of data can be explained as follows. Below approximately 180 K, Mu^+ is static [15]. As a result, both graphs are flat in this region. For $T > 180$ K, the sharp drop in the data is due to muon diffusion. As the muon begins to move faster through the lattice, the dipolar fields due to the Ga and As nuclei become motionally averaged; as a result, dipole coupling to the muon becomes weaker. Thus, we see that both the amount of muon polarization lost (measured by ZeroX) and the field spread Δ (measured by ZF-μSR) begin to decrease. Although both techniques are very different, qualitatively the agreement of the results are excellent. These data act as a proof-of-principle for the ZeroX technique.

---

[1] $\Delta = \gamma_\mu \langle B_\mu^2 \rangle^{1/2}$ measures the spread of the random dipolar fields seen by the muon in zero applied field. It appears in the static Kubo Toyabe function, which gives the functional form of $P(t)$ in ZF.

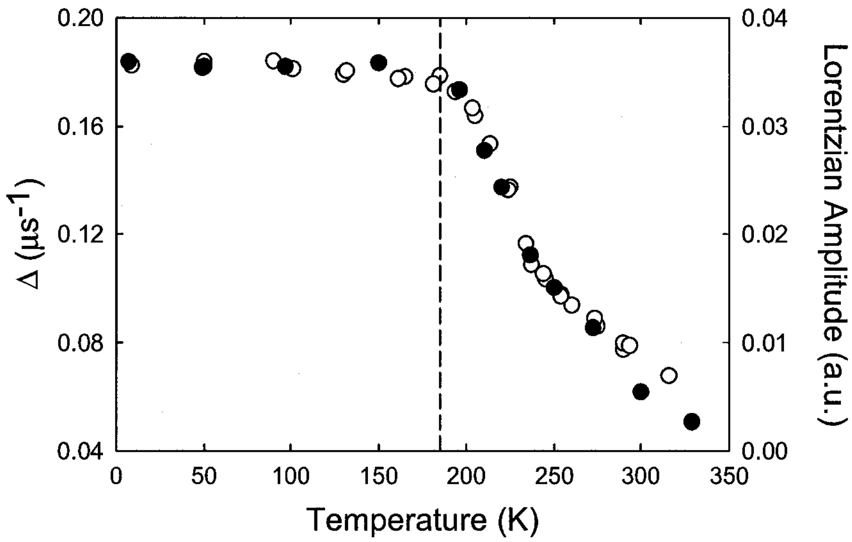

Figure 6.2: Graph showing the fitted Lorentzian amplitude (empty circles) and zero field relaxation Δ (filled circles) for various temperatures in samples of GaAs:Zn. The vertical dashed line indicates the approximate temperature where Mu^+ begins to diffuse.

6.3 *p*-type Si Measurements

In Figure 6.3, we see the behavior of the fitted Lorentzian amplitude as a function of temperature for a sample of Si:B. For "high" temperatures ($T > 50$ K) there is a decrease in A. This is attributed to motional averaging of the dipolar fields. However, in contrast to GaAs, the muon is diffusing at temperatures less than 180 K. For $T < 50$ K, the scatter in the data make it somewhat difficult to determine what is happening. However, it appears that the muon could be moving through the lattice even at very low temperatures.

Detailed analysis of the ZeroX data to extract hop rates, activation energies, etc. is ongoing; as a result, we will only briefly discuss possible models that could be used to simulate the data. One model that could be used is the strong collision model (SCM) [37], which makes two main assumptions:

1. After hopping to a new site, the muon experiences an abrupt change in local fields.
2. There is no correlation between fields before and after the jump (i.e. the muon "forgets" where it was before it hopped).

We therefore assume that the muon polarization $G_z(t)$ consists of contributions due to

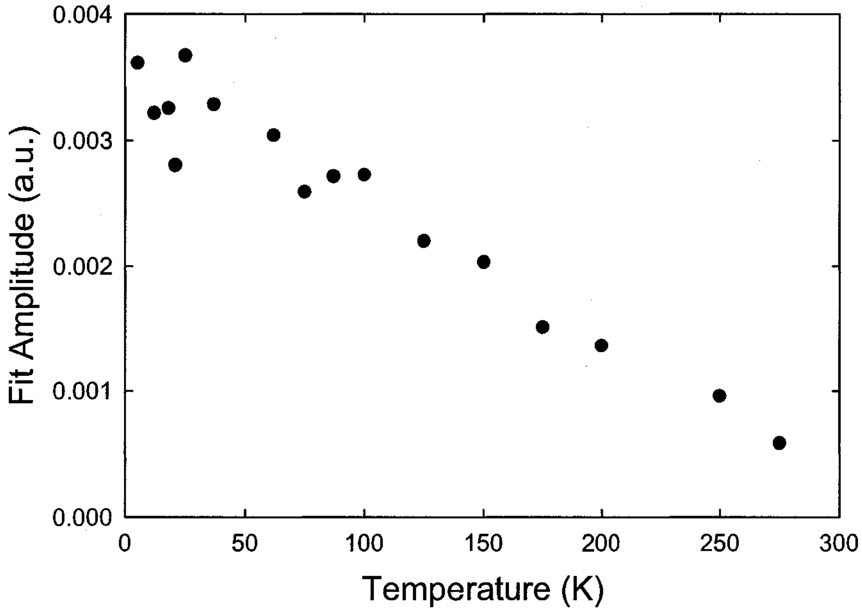

Figure 6.3: Fitted Lorentzian amplitude in Si:B at various temperatures.

muons that did not hop until time t, those that hopped once, etc. Explicitly,

$$G_z(t) = \sum_{n=0}^{\infty} g_z^{(n)}(t) \tag{6.2}$$

where $g_z^{(0)} = e^{-\nu t} g_z(t)$, $g_z(t)$ is the static muon polarization function given by (3.24), and ν is the hop rate (in MHz). This equation can be summed exactly to give

$$G_z(t) = g_z(t)e^{-\nu t} + \nu \int_0^t g_z(\tau)e^{-\nu\tau} G_z(t-\tau)d\tau \tag{6.3}$$

This is the dynamic Kubo Toyabe (dKT) function, which can be solved numerically for $G_z(t)$. This model is somewhat naive in that it assumes the muon forgets where it was after it hopped. Consider the system in Figure 6.4. Let us assume the muon starts at point A, on a bond between a ^{29}Si (lightly shaded circles) and spin-zero Si isotope (dark shaded circles). We also assume the muon then hops to one of the three bonds labeled by B (we limit ourselves to nearest neighbor hopping only). If the muon forgot the nuclear configuration after leaving B (as per the SCM), then the probability of seeing a ^{29}Si is just the natural abundance of that isotope ($\approx$ 5%). However, we see that all three

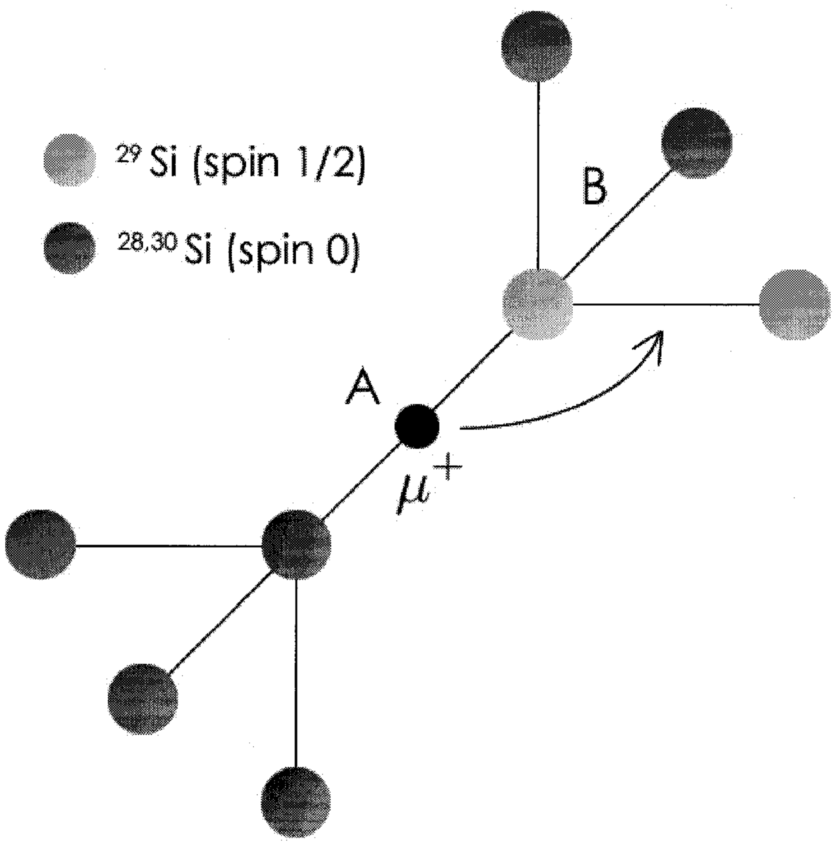

Figure 6.4: Schematic of nearest neighbor bonds open for the muon to hop to. Light and dark grey circles correspond to ^{29}Si and spin-zero isotopes respectively.

bonds at B contain at least one ^{29}Si isotope, and the muon is guaranteed to lose some of its polarization as a result. Clearly, the SCM would not adequately account for this. (Recall that the muon only interacts with the ^{29}Si isotope, which is spin 1/2).

The best method to simulate the behavior of $\bar{P}_z$ is most likely some sort of Monte Carlo algorithm. This would involve setting up an initial zincblende lattice randomly populated with Si atoms of various isotopes (based on their relative isotopic abundances), and then using a random walk to move the muon from site to site. The polarization would then be calculated at each point, and summed in an appropriate way to account for the entire diffusion process. It would be very interesting to see if this provides a reasonable description of the experimental data.

Chapter 7

Conclusion

In conclusion, we have used μSR to study diamagnetic muonium in GaAs and Si. A variety of techniques were utilized to characterize the structure and formation of Mu^+ in both heavily-doped p-type and semi-insulating samples. These include TF-μSR, muon level crossing resonance, and the new ZeroX technique used to study low-spin systems.

Using μLCR, the local structure of Mu^+ in p-type GaAs:Zn at 50 K was determined. The position and symmetry of observed level crossing resonances indicate that the muon is sitting at the bond center site between nearest neighbor Ga and As atoms. The separation between the muon and the Ga and As is found to be $r_{Ga} = 1.83 \pm 0.10$ Å and $r_{As} = 1.76 \pm 0.10$ Å, resulting in a bond relaxation of approximately 50% over the undistorted length. Comparison with theoretical calculations for H^+ in GaAs showed reasonable agreement, particularly with the Ga. The experimental value for r_{As} is significantly larger than the theoretical values predict. This is possibly attributed to the larger zero point energy of the muon, and an anharmonic potential due to the stretched Ga–As bond. These measurements represent the first experimental determination of the structure of isolated Mu^+ or H^+ in any III-V semiconductor.

An electric field was applied to SI-GaAs to enhance the diamagnetic fraction at 10 K. Measurements of the transverse field relaxation σ as a function of electric field were performed to identify which diamagnetic center is forming at each field. Comparison with known experimental results shows that in a range of fields from $1 - 15$ kV/cm, the observed center is Mu^+. In addition, μLCR experiments performed at 20 kV/cm reveal a resonance due to ^{71}Ga consistent in both position and amplitude with that seen for Mu^+ in the p-type samples. Although our data do not explicitly rule out the formation of Mu^- for $E < 1$ kV/cm, at all other measured fields Mu^+ is the diamagnetic center seen. The data support a model for Mu^0 formation where the muon thermalizes as Mu^+, then forms Mu^0 via delayed capture of an electron from the radiation track. The electric field thus acts to ionize this excited state, prohibiting formation of the neutral center and enhancing the observed diamagnetic precession signal.

With the data taken in this thesis, we have made great steps in increasing our knowledge of diamagnetic muonium in GaAs. The characterization of Mu^+ in p-type GaAs completes our knowledge of the structure of the primary muonium centers (Mu^+, Mu^0, and Mu^-) in GaAs. More detailed theoretical modeling would be extremely useful to explain the results in comparison with H^+. Identification of electric field enhanced Mu^+ in SI-GaAs has provided valuable additional information on the effect of an electric field on muonium formation. Further experiments could help to shed more light on the underlying formation mechanism, which is still not completely understood.

In addition to the work done in GaAs, a new μSR technique (dubbed ZeroX) was presented. This technique was conceived to allow materials with a low abundance of non zero nuclear spins (such as Si) to be studied with greater sensitivity. As proof-of-principle, temperature dependant ZeroX data were taken on a sample of p-type GaAs:Zn. Comparison with previous data obtained using conventional TF-μSR shows excellent qualitative agreement between the two results. Data taken in p-type Si:B indicate that the muon is moving above 50 K.

Bibliography

[1] S. M. Myers, M. I. Baskes, H. K. Birnbaum, J. W. Corbett, G. G. DeLeo, S. K. Estreicher, E. E. Haller, P. Jena, N. M. Johnson, R. Kirchheim, S. J. Pearton, and M. J. Stavola, Rev. Mod. Phys **64**, 559 (1992).

[2] S. J. Pearton, J. W. Corbett, and M. Stavola, *Hydrogen in Crystalline Semiconductors* (Springer, Berlin, 1992).

[3] *Hydrogen in Semiconductors and Metals*, edited by N. H. Nickel, W. B. Jackson, R. C. Bowman, and R. G. Leisure (Materials Research Society, Pennsylvania, 1998), Vol. 513.

[4] C. G. Van de Walle in *Semiconductors and Semimetals*, (Academic Press, New York, 1991), Vol. 34, Chap. 16.

[5] C. H. Seager and D. S. Ginley, Appl. Phys. Lett. **34**, 337 (1979).

[6] A. Rohatgi, D. L. Meier, P. Rai-Choudhury, S. J. Fonash, and R. Singh, J. Appl. Phys. **59**, 4167 (1986).

[7] B. D. Patterson, Rev. Mod. Phys. **60**, 69 (1988).

[8] A. Schenck, *Muon Spin Spectroscopy: Principles and Applications in Solid State Physics* (Adam Hilger Ltd., 1985).

[9] K. H. Chow, B. Hitti, and R. F. Kiefl in *Identification of Defects in Semiconductors*, ed. by M. Stavola (Academic Press, New York, 1998), Chap. 4.

[10] R. F. Kiefl, M. Celio, T. L. Estle, G. M. Luke, S. R. Kreitzman, J. H. Brewer, D. R. Noakes, E. J. Ansaldo, and K. Nishiyama, Phys. Rev. Lett. **58**, 1780 (1987).

[11] J. W. Schneider, R. F. Kiefl, E. J. Ansaldo, J. H. Brewer, K. Chow, S. F. J. Cox, S. A. Dodds, R. C. Duvarney, T. L. Estle, E. E. Haller, R. Kadono, S. R. Kreitzman, R.

L. Lichti, Ch. Neidermayer, T. Pfiz, T. M. Riseman, and C. Schwab, Mat. Sci. Forum **83-87**, 569 (1992).

[12] K. L. Hoffman, K. H. Chow, R. F. Kiefl, B. Hitti, T. L. Estle, and R. L. Lichti, Physica B **326**, 175 (2003).

[13] L. Pavesi and P. Giannozzi, Phys. Rev. B **46**, 4621 (1992).

[14] K. H. Chow, B. Hitti, R. F. Kiefl, S. R. Dunsiger, R. L. Lichti, and T. L. Estle, Phys. Rev. Lett. **76**, 3790 (1996).

[15] K. H. Chow, B. Hitti, R. F. Kiefl, R. L. Lichti, and T. L. Estle, Phys. Rev. Lett. **87**, 216403 (2001).

[16] K. H. Chow, R. F. Kiefl, W. A. MacFarlane, and J. W. Schneider, Phys. Rev. B **51**, 14762 (1995).

[17] S. K. Estreicher, Mater. Sci. Forum **148–149**, 349 (1994).

[18] D. G. Eshchenko, V. G. Storchak, J. H. Brewer, and R. L Lichti, Phys. Rev. Lett **89**, 226601 (2002).

[19] D. G. Eshchenko, V. G. Storchak, and G. D. Morris, Phys. Lett. A **264**, 226 (1999).

[20] S. R. Kreitzman, D. J. Arseneau, B. Hitti, and J. H. Brewer, *μSR Facility Users Guide* (1999).

[21] M. Weissbluth, *Atoms and Molecules* (Academic Press Inc., 1980).

[22] C. P. Slichter, *Principles of Magnetic Resonance* (Berlin; New York: Springer, 1996).

[23] E. Roduner and H. Fischer, Chem. Phys **54**, 261 (1981).

[24] J. W. Schneider, *Avoided-Level-Crossing: A New Technique in Muon Spin Rotation to Study the Nuclear Hyperfine Structure of Muonium Centres in Semiconductors* (Thesis, Universität Zürich, 1989).

[25] T. L. Estle, *Hamiltonians, Line Shapes, and Spectra* (unpublished notes, μSR summer school) (1996).

[26] O. Hartmann, Phys. Rev. Lett. **39**, 832 (1977).

[27] K. H. Chow, *Spin Dynamics and Electronic Structure of Muonium and its Charged States in Silicon and Gallium Arsenide* (Ph.D. thesis, University of British Columbia, 1995).

[28] J. H. Van Vleck, Phys. Rev. **74**, 1168 (1948).

[29] B. E. Schultz, K. H. Chow, B. Hitti, R. F. Kiefl, R. L. Lichti, and S. F. J. Cox, Phys. Rev. Lett. (in press).

[30] *Landolt-Börnstein New Series*, edited by O. Madelung, M. Schulz, and H. Weiss (Springer-Verlag, New York, 1982), Vol. 17.

[31] S. J. Breuer, R. Jones, P. R. Briddon, and S. Öberg, Phys. Rev. B **53**, 16289 (1996).

[32] R. F. Kiefl, J. W. Schneider, H. Keller, W. Kündig, W. Odermatt, B. D. Patterson, K. W. Blazey, T. L. Estle, and S. L. Rudaz, Phys. Rev. B **32**, 530 (1985).

[33] MINUIT: Function Minimization and Error Analysis, CERN, Geneva, Switzerland.

[34] B. E. Schultz, K. H. Chow, B. Hitti, Z. Salman, S. R. Kreitzman, R. F. Kiefl, and R. L. Lichti, Phys. Rev. B **72**, 033201 (2005).

[35] D. G. Eshchenko, V. G. Storchak, J. H. Brewer, G. D. Morris, S. P. Cottrell, and S. F. J. Cox, Phys. Rev. B **66**, 035105 (2002).

[36] V. G. Storchak, D. G. Eshchenko, R. L. Lichti, and J. H. Brewer, Phys. Rev. B **67**, 121201 (2003).

[37] R. S. Hayano, Y. J. Uemura, J. Imazato, N. Nishida, T. Yamazaki, and R. Kubo, Phys. Rev. B **20**, 850 (1979).

[38] T. M. Riseman and J. H. Brewer, Hyperfine Interactions **65**, 1107 (1990).

Appendix A

Rotating Reference Frame (RRF)

In weak TF experiments, the precession frequencies are typically on the order of only a few MHz. Slowly oscillating signals naturally require fewer data points, making storage and fitting of the data efficient. As well, the signals are visually quite easy to pick out [for example, see Figure 2.3(b)]. However, in high TF experiments, muon precession frequencies can be several hundred MHz; this requires that the display and fitting software handle a much larger number of data points in order to accurately represent the oscillations. The usual practice in these instances is to perform a rotating reference frame (RRF) transformation during the fitting or displaying of the data [38].

Suppose that the signal of interest is precessing at a frequency ω_μ in the lab frame. The RRF is taken to rotate at some other frequency ω_{RRF}. The data are then displayed using the difference in these frequencies. It is common to take $\omega_{RRF} < \omega_\mu$, where the difference is only a few MHz. For example, in an applied transverse field of $B = 1$ T where $\omega_\mu = 135.54$ MHz, one would define a rotating reference frame frequency of $\omega_{RRF} \approx 134$ MHz.

Transforming the data in this way has a couple of advantages. First, data displayed with a slower oscillation are more clear. This makes it easier to visually analyse the data, including picking out complicated behavior such as beating due to multiple muon precession frequencies. This is illustrated in Figure A.1. Part (a) shows a raw TF spectrum for a sample of GaN at $T = 2$ K with $B_{TF} \approx 240$ mT. The large number of data points makes it almost impossible to try and visually analyse the data. However, after transforming to the RRF, the signal becomes much better defined; this is shown in part (b) of the figure, where $\omega_{RRF} = 31$ MHz. In addition to making the data visually clearer, it becomes more efficient to fit the data because a coarse binning usually accompanies the transformation to the RRF. If the data are repacked by a factor n, then the fitting efficiency will increase by roughly the same amount. As well, the error bars on each data point will decrease by $\sim \sqrt{n}$.

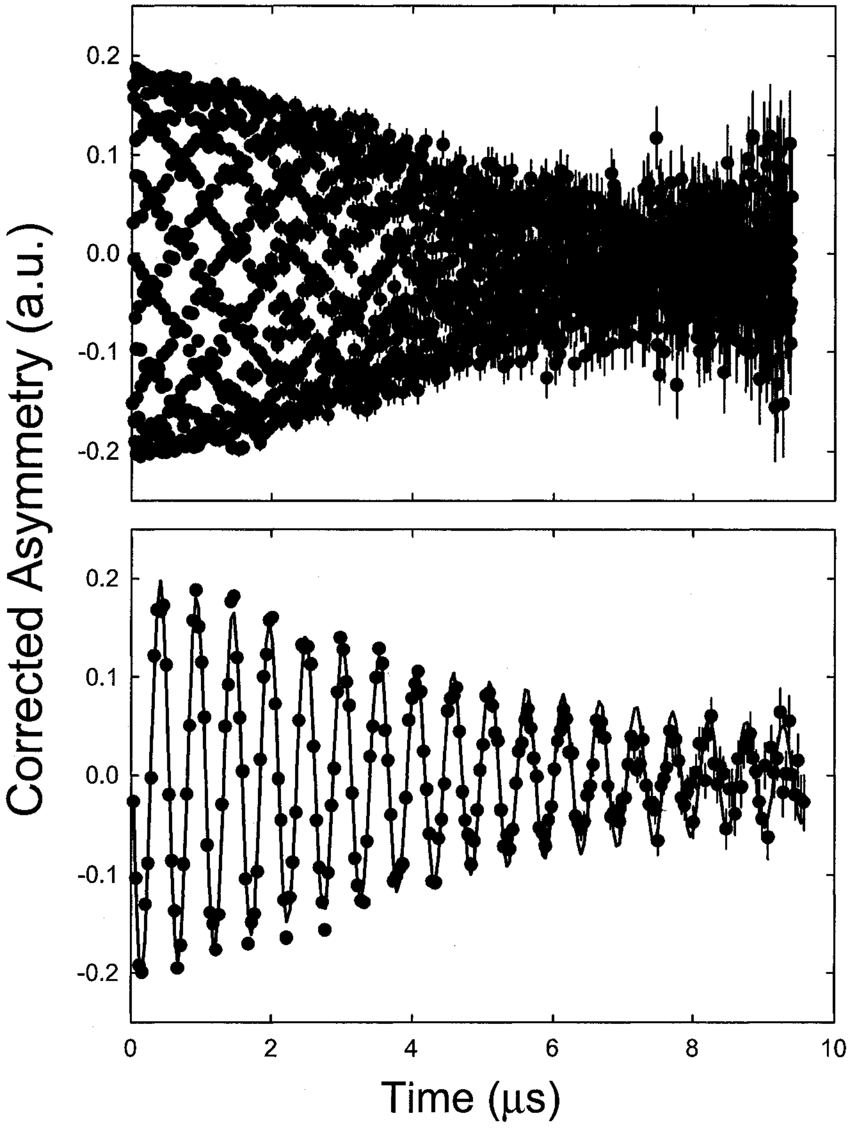

Figure A.1: Time-dependant data for GaN at $T = 2$ K and with $B_{TF} \approx 240$ mT. (a) Raw data in lab frame. (b) Data transformed to the RRF, with $\omega_{RRF} = 31$ MHz.

Appendix B

Mathematica Code

This chapter contains the code used to simulate the μLCR spectra in Chapters 3 and 4. There are a number of programming languages capable of performing the numerical matrix operations required, including Fortran, C, and C++; however, most of the simulations were performed using Mathematica. Although compiled languages such as Fortran can often perform complicated numerical calculations faster, Mathematica has a few advantages:

- It is simpler to generate the spin matrices using Mathematica's built-in matrix operations and user-defined functions (such as for the matrix direct product).
- Results of the simulations can be immediately graphed and viewed without the need for an additional graphing program. The theoretical lines can also be graphed over the raw data, making fitting easier.

The code below is based on a Fortran program originally written by K. H. Chow. The form was not changed much from the procedural Fortran code, and as a result is not necessarily the most optimal form for Mathematica to handle.

Listing B.1: Mathematica code used to simulate μLCR spectra.

```
Clear["Global‘*"];
SetDirectory["d:/"];
Off[General::spell,General::spell1];
<<Graphics‘MultipleListPlot‘;
<<Graphics‘Graphics‘;
<<LinearAlgebra‘MatrixManipulation

gammau = 135.5374;
```

```
gamma71 = 12.984;
gamma69 = 10.219;
gamma75 = 7.292;
d71 = 0.019;
d69 = (gamma69/gamma71) d71;
d75 = 0.012
dp71 = -2 d71;
dp69 = -2 d69;
dp75 = -2 d75;
q71 = 12.89;
q69 = (0.178/0.112) q71;
q75 = 44.975;
abun71 = 0.398;
abun69 = 0.602;
dec = 1/2.19703;

theta171 = (54.74/180) π;
theta271 = (0/180) π;
theta169 = (54.74/180) π;
theta269 = (0/180) π;

pop171 = 1;
pop271 = 0;
pop169 = 1;
pop269 = 0;

flip1plus71 = 21.28/10000;
flip1minus71 = 20.815/10000;
flip2plus71 = flip1plus71;
flip2minus71 = flip1minus71;
flip1plus69 = flip1plus71;
flip1minus69 = flip1minus71;
flip2plus69 = flip1plus71;
flip2minus69 = flip1minus71;

a_List?MatrixQ⊗b_List?MatrixQ := BlockMatrix[Outer[Times,a,b]];

im2 = IdentityMatrix[2];
im4 = IdentityMatrix[4];
μx = {{0,1/2},{1/2,0}};
μy = {{0,(-1/2) i},{(1/2) i,0}};
μz = {{1/2,0},{0,-1/2}};
gax = {{0,Sqrt[3]/2,0,0},{Sqrt[3]/2,0,1,0},{0,1,0,Sqrt[3]/2},
   {0,0,Sqrt[3]/2,0}};
```

```
ga_y = {{0,-i Sqrt[3]/2,0,0},{i Sqrt[3]/2,0,-i,0},{0,i,0,-i Sqrt[3]/2},
  {0,0,i Sqrt[3]/2,0}};
ga_z = {{3/2,0,0,0},{0,1/2,0,0},{0,0,-1/2,0},{0,0,0,-3/2}};
as_x = {{0,Sqrt[3]/2,0,0},{Sqrt[3]/2,0,1,0},{0,1,0,Sqrt[3]/2},
  {0,0,Sqrt[3]/2,0}};
as_y = {{0,-i Sqrt[3]/2,0,0},{i Sqrt[3]/2,0,-i,0},{0,i,0,-i Sqrt[3]/2},
  {0,0,i Sqrt[3]/2,0}};
as_z = {{3/2,0,0,0},{0,1/2,0,0},{0,0,-1/2,0},{0,0,0,-3/2}};

σ_z = 2μ_z⊗IdentityMatrix[16];
ix = (μ_x⊗im4)⊗im4;
iy = (μ_y⊗im4)⊗im4;
iz = (μ_z⊗im4)⊗im4;
jx = (im2⊗ga_x)⊗im4;
jy = (im2⊗ga_y)⊗im4;
jz = (im2⊗ga_z)⊗im4;
kx = im4⊗(im2⊗as_x);
ky = im4⊗(im2⊗as_y);
kz = im4⊗(im2⊗as_z);

ixp = Cos[theta] ix-Sin[theta] iz;
iyp = iy;
izp = Sin[theta] ix+Cos[theta] iz;
jxp = Cos[theta] jx-Sin[theta] jz;
jyp = jy;
jzp = Sin[theta] jx+Cos[theta] jz;
kxp = Cos[theta] kx-Sin[theta] kz;
kyp = ky;
kzp = Sin[theta] kx+Cos[theta] kz;
Hz71 = -gammau g iz-gamma71 g jz-gamma75 g kz;
Hz69 = -gammau g iz-gamma69 g jz-gamma75 g kz;
Hd71 = dp71 (izp.jzp)+d71 (ixp.jxp+iyp.jyp)+dp75 (izp.kzp)+d75
    (ixp.kxp+iyp.kyp);
Hd69 = dp69 (izp.jzp)+d69 (ixp.jxp+iyp.jyp)+dp75 (izp.kzp)+d75
    (ixp.kxp+iyp.kyp);
Hq71 = q71 (jzp.jzp-(5/4) IdentityMatrix[32])+q75 (kzp.kzp-(5/4)
    IdentityMatrix[32]);
Hq69 = q69 (jzp.jzp-(5/4) IdentityMatrix[32])+q75 (kzp.kzp-(5/4)
    IdentityMatrix[32]);
H71 = Hz71+Hd71+Hq71;
H69 = Hz69+Hd69+Hq69;

npts = 300;
b0 = 0.18;
```

```
bf = 0.21;
step = (bf-b0)/npts;
P = Table[e[i,j],{i,npts+1},{j,2}];
Pd = Table[e[i,j],{i,npts+1},{j,2}];
Do[
  {bn = b0+(t-1) step,
  Do[
    {Which[
      kflip == 1, bin = bn,
      kflip == 2, bin = bn+flip1plus71,
      kflip == 3, bin = bn-flip1minus71
    ],
    hn = H71/.{g→bin, theta→theta171},
    {vals, vecs} = Eigensystem[hn],
    tot = 0,
    Do[
      Do[
        {aij = vecs[[i]].σz.vecs[[j]],
        wij = (vals[[i]]-vals[[j]]) 2 π,
        tot = tot+(aij^2 wij^2)/(dec^2+wij^2)
        },
      {j, i+1,32}
      ],
    {i,1,32}
    ],
    Which[
      kflip == 1, p171 = 1-(2/32) tot,
      kflip == 2, p1plus71 = 1-(2/32) tot,
      kflip == 3, p1minus71 = 1-(2/32) tot
    ],

    Which[
      kflip == 1, bin = bn,
      kflip == 2, bin = bn+flip2plus71,
      kflip == 3, bin = bn-flip2minus71
    ],
    hn = H71/.{g→bin, theta→theta271},
    {vals, vecs} = Eigensystem[hn],
    tot = 0,
    Do[
      Do[
        {aij = vecs[[i]].σz.vecs[[j]],
        wij = (vals[[i]]-vals[[j]]) 2 π,
        tot = tot+(aij^2 wij^2)/(dec^2+wij^2)
```

```
      },
    {j,i+1,32}
    ],
  {i,1,32}
  ],
  Which[
    kflip == 1, p271 = 1-(2/32) tot,
    kflip == 2, p2plus71 = 1-(2/32) tot,
    kflip == 3, p2minus71 = 1-(2/32) tot
  ],

  Which[
    kflip == 1, bin = bn,
    kflip == 2, bin = bn+flip1plus69,
    kflip == 3, bin = bn-flip1minus69
  ],
  hn = H69/.{g→bin,theta→theta169},
  {vals,vecs} = Eigensystem[hn],
  tot = 0,
  Do[
    Do[
      {aij = vecs[[i]].σz.vecs[[j]],
      wij = (vals[[i]]-vals[[j]]) 2 π,
      tot = tot+(aij^2 wij^2)/(dec^2+wij^2)
      },
    {j,i+1,32}
    ],
  {i,1,32}
  ],
  Which[
    kflip == 1, p169 = 1-(2/32) tot,
    kflip == 2, p1plus69 = 1-(2/32) tot,
    kflip == 3, p1minus69 = 1-(2/32) tot
  ],

  Which[
    kflip == 1, bin = bn,
    kflip == 2, bin = bn+flip1plus71,
    kflip == 3, bin = bn-flip1minus71
  ],
  hn = H69/.{g→bin,theta→theta269},
  {vals,vecs} = Eigensystem[hn],
  tot = 0,
  Do[
```

```
        Do[
          {aij = vecs[[i]].σz.vecs[[j]],
          wij = (vals[[i]]-vals[[j]]) 2 π,
          tot = tot+(aij^2 wij^2)/(dec^2+wij^2)
          },
        {j,i+1,32}
        ],
      {i,1,32}
      ],
      Which[
        kflip == 1, p269 = 1-(2/32) tot,
        kflip == 2, p2plus69 = 1-(2/32) tot,
        kflip == 3, p2minus = 1-(2/32) tot
      ],
    {kflip,1,3,1}
    ],
    pangle1 = abun71 p171+abun69 p169,
    pangle2 = abun71 p271+abun69 p269,
    p1diff71 = p1plus71-p1minus71,
    p2diff71 = p2plus71-p2minus71,
    p1diff69 = p1plus69-p1minus69,
    p2diff69 = p2plus69-p2minus69,
    pdiff1 = abun71 p1diff71+abun69 p1diff69,
    pdiff2 = abun71 p2diff71+abun69 p2diff69,
    pint = pop171 pangle1+pop271 pangle2,
    pdif = pop171 pdiff1+pop271 pdiff2,
    P[[t,1]] = N[bn],
    P[[t,2]] = pint,
    Pd[[t,1]] = N[bn],
    Pd[[t,2]] = pdif,
    },
  {t,1,npts+1}
  ];

  temp1 = 1;
  temp2 = 0;
  temp3 = 0;
  temp4 = 0;
  Do[
    {k = i-1,
    If[
      Abs[P[[k,2]]]<temp1, {temp1 = P[[k,2]], temp2 = P[[k,1]]}
    ],
    If[
```

```
    Abs[Pd[[k,2]]]>temp3, {temp3 = Abs[Pd[[k,2]]], temp4 = Pd[[k,1]]}
  ]
  }
{i,2,Dimensions[P][[1]]}
];

ListPlot[P,PlotJoined→True,ImageSize→600];
ListPlot[Pd,PlotJoined→True,PlotRange→{{b0,bf},{-1.1 temp3, 1.1
    temp2}},ImageSize→600];

shift = 0;
normal = 0.183842;
fieldm = 6.143497 10^-6;
fieldb = 0.00016579;
def[a_,b_,c_,d_] := {peakl = a,peakr = b,binsizeline = c,binsizepeak = d};
def[47800,50900,160,80];
lcrdata = {#[[1]],#[[2]]/normal-shift ,#[[3]]/normal}&/@
  Import["5702.pld","Table"];
simshift = {#[[1]],#[[2]]}&/@Pd;
datamin1 = lcrdata[[1,1]];
datamax1 = peakl;
datamin2 = peakr;
datamax2 = lcrdata[[Dimensions[lcrdata][[1]],1]];
binnum1 = Ceiling[(datamax1-datamin1)/binsizeline];
binnum2 = Ceiling[(datamax2-datamin2)/binsizepeak];
binned1 = Table[e[i,j],{i,binnum1},{j,3}];
binned2 = Table[e[i,j],{i,binnum2},{j,3}];
binnedpeak = Table[e[i,j],{i,binnumpeak},{j,3}];
Do[
  {tot = 0,
  num = 0,
  err = 0,
  Do[
    {If[
      lcrdata[[j,1]]≥datamin1+(i-1) binsizeline&&lcrdata[[j,1]]<datamin1+i
          binsizeline,
      {tot = tot+lcrdata[[j,2]],
      err = err+lcrdata[[j,3]]^2,
      num = num+1
      }
    ],
    If[
      num>0,
      {binned1[[i,1]] = N[datamin1+(i-1) binsizeline],
```

```
      binned1[[i,2]] = N[tot/num],
      binned1[[i,3]] = N[Sqrt[err]/num]
      }
    ]
    },
  {j,1,Dimensions[lcrdata][[1]]}
  ]
  },
{i,1,binnum1}
];
Do[
  {tot = 0,
  num = 0,
  err = 0,
  Do[
    {If[
      lcrdata[[j,1]]≥peakl+(i-1) binsizepeak&&lcrdata[[j,1]]<peakl+i
          binsizepeak,
      {tot = tot+lcrdata[[j,2]],
      err = err+lcrdata[[j,3]]^2,
      num = num+1
      }
    ],
    If[
      num>0,
      {binnedpeak[[i,1]] = N[peakl+(i-1) binsizepeak],
      binnedpeak[[i,2]] = N[tot/num],
      binnedpeak[[i,3]] = N[Sqrt[err]/num]
      }
    ]
    },
  {j,1,Dimensions[lcrdata][[1]]}
  ]
  },
{i,1,binnumpeak}
];
Do[
  {tot = 0,
  num = 0,
  err = 0,
  Do[
    {If[
      lcrdata[[j,1]]≥datamin2+(i-1) binsizeline&&lcrdata[[j,1]]<datamin2+i
          binsizeline,
```

```
      {tot = tot+lcrdata[[j,2]],
      err = err+lcrdata[[j,3]]^2,
      num = num+1
      }
    ],
    If[
      num>0,
      {binned2[[i,1]] = N[datamin2+(i-1) binsizeline],
      binned2[[i,2]] = N[tot/num],
      binned2[[i,3]] = N[Sqrt[err]/num]
      }
    ]
    },
  {j,1,Dimensions[lcrdata][[1]]}
  ]
  },
{i,1,binnum2}
];
complete = Join[binned1,binnedpeak,binned2];
completecal = {#[[1]] fieldm+fieldb,#[[2]],#[[3]]}&/@complete;
g1 = ErrorListPlot[completecal,DisplayFunction→Identity];
g2 = ListPlot[simshift,PlotJoined→True,PlotStyle→{Thickness[0.003],
  RGBColor[0,0,1]},DisplayFunction→Identity];
Show[g1,g2,PlotRange→{{0.99 completecal[[1,1]],1.01
  completecal[[Dimensions[completecal][[1]],1]]},
  {-1.3 temp2,1.3 temp2}},DisplayFunction→$DisplayFunction,
  ImageSize→600];

Export["data.txt",completecal,"Table"];
Export["sim.txt",simshift,"Table"];
```